Frustration in soft matter: interplay between order and curvature

Cover illustration: snapshot from the animation “Yozhik v tumane” (Hedgehog in the fog) by Yuri Norstein, Soyuzmultfilm, 1975.

Bookmark: statue of the Hedgehog in Kiev, photo by Dasha Maniugina.

Frustration in soft matter: interplay between order and curvature
PhD Thesis, Radboud University Nijmegen, The Netherlands
Illustrated
With summary in English, Dutch, Russian
ISBN 9789081447713
printed by PrintPartners Ipskamp, Enschede

Frustration in soft matter:
interplay between order and curvature

een wetenschappelijke proeve op het gebied van de
Natuurwetenschappen, Wiskunde en Informatica

Proefschrift

ter verkrijging van de graad van doctor
aan de Radboud Universiteit Nijmegen,
op gezag van de rector magnificus prof. mr. S. C. J. J. Kortmann,
volgens besluit van het college van decanen
in het openbaar te verdedigen op maandag 7 september 2009
om 13.30 uur precies

door

Oksana V. Manyuhina

geboren op 11 februari 1982
te Sint-Petersburg

Promotores: Prof. dr. M. I. Katsnelson
Prof. dr. A. Fasolino

Manuscriptcommissie: Prof. dr. E. Vlieg (voorzitter)
Prof. dr. E. Kats (Institut Laue Langevin)
Prof. dr. M. A. H. Vozmediano
(Instituto de Ciencia de Materiales de Madrid)

Dedicated to my parents,
my sister Dasha,
and my husband Kostya.

Contents

List of publications:

Large portion of this thesis has appeared in the following publications:

Chapter 1: "Slow dynamics in a model of the cellulose network",
O. V. Manyuhina, A. Fasolino, and M. I. Katsnelson, *Polymer* **48**, 4849 (2007), `arXiv:0706.0997`.

Chapter 3: "Anharmonic magnetic deformation of self-assembled molecular nanocapsules",
O. V. Manyuhina, I. O. Shklyarevskiy, P. Jonkheijm, P. C. M. Christianen, A. Fasolino, M. I. Katsnelson, A. P. H. J. Schenning, E. W. Meijer, O. Henze, A. F. M. Kilbinger, W. J. Feast, and J. C. Maan, *Phys. Rev. Lett.* **98**, 146101 (2007), `arXiv:cond-mat/0703298`.

Chapter 4: "Topological instabilities of spherical vesicles",
O. V. Manyuhina, A. Fasolino, P. C. M. Christianen, and M. I. Katsnelson, *Phys. Rev. E* **80**, R010403 (2009), `arXiv:0802.2786`.

Chapter 5: "Topological defects and shape of aromatic self-assembled vesicles",
O. V. Manyuhina, A. Fasolino, and M. I. Katsnelson, *J. Phys. Chem. B* **113**, 10549 (2009), `arXiv:0907.1842`.

Other publications of the author of the thesis:

"Modeling of weak blast wave propagation in the lung",
A. I. D'yachenko, and O. V. Manyuhina, *J. Biomech.* **39**, 2113 (2006).

Introduction

We know from school that there are three states of matter: solid, liquid and gas. There is also **soft matter** which is neither crystalline nor liquid, but somewhere in between. Examples of soft matter are foams, gels, colloids, liquid crystals, membranes and a number of biological materials. Soft matter essentially differs from hard matter. In Table 1 we compare their characteristic length scales, energy scales and elastic moduli. Since the interaction energy between the components of soft matter systems is of the order of the thermal energy $k_B T$, thermal fluctuations can bring the system to an energy state very different from the initial one. Because of the small value of their elastic modulus (billion! times smaller than in hard matter) soft materials can easily adjust to external conditions by changing their shape.

In physics there are two approaches to study the behaviour of complex systems with many degrees of freedom, either by doing first principles calculations based on the detailed description of molecular interactions or by using *phenomenology*[1]. When we consider soft materials with characteristic length scales of the order of microns (thousands of molecules, millions of atoms) the atomistic approach, which is widely used in solid state physics, becomes inappropriate or at least cumbersome for calculations. The phenomenology, on the other hand, turns out to be an adequate tool to describe the collective behaviour of the system on *mesoscopic* (between microscopic and macroscopic) length scales. The phenomenology in statistical physics dates back to L. D. Landau who established the theory of second order phase transitions. Landau conjectured that a phase transition between two uniform phases can be described by what is called the *order parameter*, a quantity that is different from zero in one phase (ordered phase) and vanishes in the other (disordered phase). A typical example is the magnetization of ferromagnets below and above the Curie temperature. Further, he assumed that in the vicinity of a phase transition, the order parameter ϕ is small and spatially uniform, and the free energy (analog of energy) density can be expanded in a power series in ϕ as

$$f(T,\phi) = f_0 + a\phi + b\phi^2 + c\phi^3 + d\phi^4 + \dots,$$

where the coefficients $a, b, c, \dots$ depend on the temperature T. It was P. G. DeGennes ('founding father of soft matter') who realized that the concept of order parameter could be applied to soft matter, in particular to polymers and liquid crystals, and he received the Nobel prize for this discovery.

---

[1] Most theories may be thought of as phenomenological since they are based on assumptions.

Table 1: Hard matter versus soft matter, where L is a typical length scale, E is a typical energy scale and $G \propto E/L^3$ is a typical elastic modulus. In SI units: 1 Å $= 10^{-10}$ m, $1\ \mu\mathrm{m} = 10^{-6}$ m, $1\ \mathrm{eV} \simeq 1.6 \cdot 10^{-19}$ J, $k_B T = 1/40\ \mathrm{eV} \simeq 4 \cdot 10^{-21}$ J.

	Hard	**Soft**
L	1 Å	$1\ \mu$m
E	1 eV	$k_B T$
G	1 GPa	1 Pa

In this thesis we study the equilibrium properties of different soft systems, corresponding to the minimum of their free energy. However in many situations the free energy contains competing terms, which favour incompatible ground states, resulting in **frustration**. The concept of frustration was introduced by G. Toulouse in 1977 in the context of spin glasses, where one cannot minimize the free energy of the system by minimizing all local interactions [1]. Then this concept was generalized to many physical systems, including biological ones, and in view of the title of this thesis, we mention several definitions and examples:

(1) *Frustration* is the competition between different influences on a physical system that favour incompatible ground states [2].

(2) *Frustration* describes incompatibility between locally preferred order and global constraints, for instance it is impossible to fill 2D space with pentagons or 3D space with tetrahedra (always exists angular deficit) [3].

(3) *Frustration* is the impossibility to let all atoms occupy simultaneously the positions corresponding to the minimum of the pair potential, e.g. antiferromagnet on a triangular lattice [4].

(4) *Frustration* arises between the requirements of constant distance and the appearance of a new symmetry [3].

(5) *'Frustration'*, deviation from 'perfection', leads to the formation of defects.

This list of the definitions can be further extended, but it is not within the scope of this thesis to illustrate all examples of frustration that could happen in nature.

Outline

Motivated and inspired by experimental observations in the High Field Magnet Laboratory (HFML) and in the Department of Experimental Botany at our university, we will consider here several examples of frustrated soft matter systems.

In chapter 1 we present a coarse-grained model of the cellulose network, which consists of stiff rods connected by stretchable crosslinks. The competing interactions between

Table 2: A rough overview of the chapters of the thesis. The order parameter of the studied systems is written in the columns, and the rows distinguish the phenomenological approach.

Coarse-grained	*Ch. 1* orientation of microfibrils		*Ch. 6* 1D density modulation
Geometric	*Ch. 3,4* normal to the surface	*Ch. 5* tangent vector	

microfibrils orientation and the stretchable network of crosslinks results in a slow glassy dynamics. Our findings are compatible with the experimental observations of logarithmic creep in plant cell walls. We discuss the potential advantages of soft materials to be in frustrated glassy states.

The next chapter serves as an introduction to differential geometry and to the phenomenological models of fluid membranes (two dimensional layers of molecules). These models are based on the Landau–Ginsburg free energy with an order parameter related to curvature. The basic concepts, used throughout the rest of the thesis, are introduced here.

Chapter 3 connects the experimental observations of magnetically deformed spherical nanocapsules (vesicles) with theory. To quantify the effect of magnetic fields on self-assembled structures, we compare two theoretical approaches, discussed in chapter 2, and extract the values of elastic constants from experimental data.

In chapter 4 we propose a new candidate to the equilibrium shapes of spherical vesicles. We study the possibility of topological transformations between spherical vesicles and present a phase diagram. Interestingly, not only temperature, but also magnetic fields can induce topological transformations.

In chapter 5 we demonstrate that the stacking of flat aromatic molecules on a curved surface leads to topological defects. The competition between topological defects and elastic energy results in elongated equilibrium shapes. This simple geometric approach allows to take into account the details of microscopic interactions between aromatic molecules in phenomenological (mesoscopic) models.

In the last chapter we consider the effect of frustration in liquid crystals, that leads to a doubly-periodic pattern, observed experimentally, but not explained yet theoretically. We use the geometric approach based on minimal surfaces to describe the organization of smectic layers in presence of competing boundary conditions.

Table 2 presents a schematic overview of the thesis, distinguishing the used phenomenological approaches and differentiating the order parameter used for the studied systems (chapters).

1

Slow dynamics in a model of cellulose network

Contents

We present numerical simulations of a model that captures the main structural features of cellulose. Within a broad range of temperatures the competing interactions between the microfibrils orientation and the stretchable network of xyloglucan molecules result in a slow glassy dynamics. In particular, the relaxation of microfibril orientation is described by logarithmic time dependence and translational motion is characterized by strongly subdiffusive dynamics. Weakening of interactions between cellulose microfibrils and xyloglucan molecules results in a more marked reorientation, suggesting a possible mechanism to influence the growth of the plant cell wall.

1.1 The plant cell wall

Cellulose accounts for more than half of all living matter and it is the basic structural component of plant cell walls. Every year plants produce $1.8 \cdot 10^{11}$ tons of cellulose, which is much more than production of steel, concrete oil and gas together. Since cellulose is the most abundant organic compound in nature it is cheap and widely used in industry for the manufacture of paper, cellophane, rayon, etc. Also it may be a potential source for biofuel. Cellulose with the formula $(C_6H_{12}O_6)_n$ is a polysaccharide consisting of 2000 and more (1-4)β D-glucose units covalently linked into chains (see Fig. 1.1). The resulting cellulose microfibril is 5–15 nm wide and 1–5 μm long with strength similar to that of steel, which is important for the rigidity of the plant cell wall. The inner part of the fibril is crystalline, the outer region is more amorphous. The degree of crystallinity, the length and the orientation of cellulose microfibrils influence the structural and mechanical properties of the cell wall. The ideal organisation of the cellulose network must provide strength while remaining flexible to allow the growing of the plant cell walls. In [5] the authors suggest that among known cell wall architectures that are axial, transverse, crossed, helical and helicoidal, the latter combines in the best way strength and flexibility. In Fig. 1.1 we show an image of elongating carrot cell wall, where long cellulose microfibrils are oriented perpendicular to the axis of cell elongation.

The cell wall of higher plants is composed of crystalline cellulose microfibrils (30%), embedded in a matrix of hemicellulose, usually xyloglucans (30%), pectin polysaccharides (35%) and proteins (5%) [7] as illustrated in Fig. 1.2. The xyloglucans, that are much longer ($\approx 50 - 500$ nm) than the spacing between cellulose (20–40 nm), can bind tightly to the amorphous surface of cellulose fibrils and link them together as one can see in Figs. 1.1,1.2. In this assembly the crystalline cellulose microfibrils play the role of stiff element, whereas the hemicellulose matrix imparts the elastic properties, which allow the growth of the cell. In order to get insight into the structure, formation and growth of plant

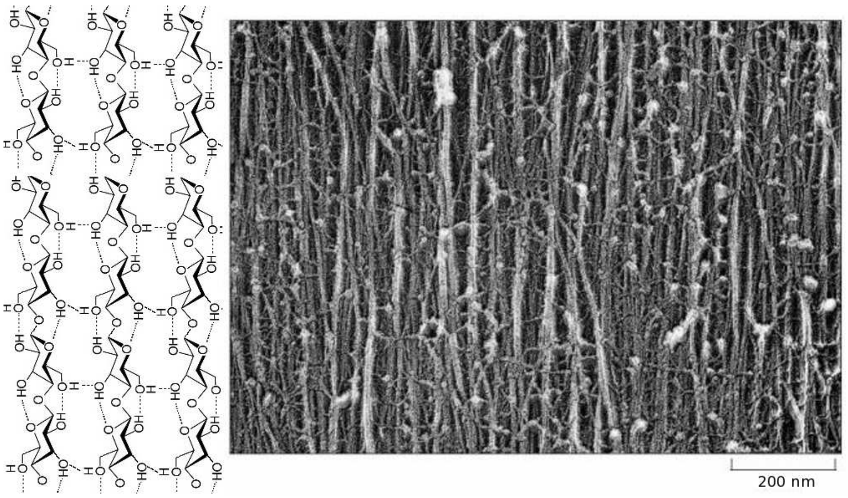

Figure 1.1: On the left: the chemical structure of cellulose microfibril composed of D-glucose units, covalently bonded to one another within a chain and stabilized by hydrogen bonds (dotted lines) between the chains. On the right: the electronic microscopy image of elongating carrot cell [6]. The cellulose microfibrils are oriented perpendicular to the direction of growth.

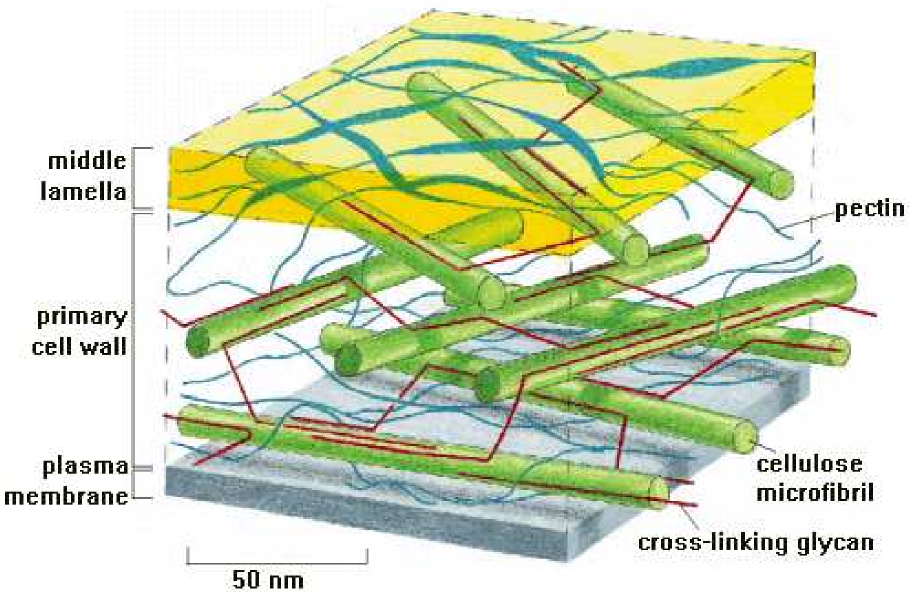

Figure 1.2: Organization of the plant cell wall: layers of cellulose microfibrils (green) embedded in a network of crosslinking xyloglucans (red) and matrix of pectins (blue) [6].

cells in nature, a bacterial cellulose is used as a model system in experiments. A bacterial cellulose composite produced by *Acetobacter xylinum* is a pure cellulose–xyloglucan network with degree of crystallinity around 75% [8, 9].

1.2 Creep in cellulose

Our interest in bacterial cellulose arises from experimental observations described in the references [10, 11]. Creep experiments performed in our university have shown that, under a unidirectional force of 0.1 N, the elongation of the plant cell wall is logarithmic in time $L = L_0 + N_{\text{creep}} \log t$ with the constant creep rate $N_{\text{creep}} = 0.101 \pm 0.013$ mm for *Acetobacter xylinum* [10]. The authors have also found that the presence of the cell wall loosening lipid transfer proteins (LTP) increases the creep rate but the elongation remains logarithmic. Interestingly, logarithmic creep was also found in polyethylene, rocks and metals, that are materials with completely different microscopic structure. In the other experiment [11], the dielectric properties of bacterial cellulose were studied in the frequency range 100 Hz–1 MHz and at temperatures between 100 and 440 K. A broad peak of dielectric absorption was found for $200\text{ K} < T < 280\text{ K}$, indicating a wide distribution of the relaxation times. These slowing down of relaxation and logarithmic time evolution are dynamical features typical of glassy systems (see Annotation 1.1 on p. 12). Therefore a possible explanation of the described phenomena could be attributed to the slow relaxation of structural elements within the cellulose–xyloglucan polymer network. In order to test this hypothesis and to understand whether bacterial cellulose can be in the glassy state or not, we need to formulate a model.

1.3 Coarse-grained modelling

We propose the coarse grained atomistic model of cellulose microfibrils and xyloglucan molecules illustrated in Fig. 1.3, to simulate bacterial cellulose, a prototype of cellulose in higher plants [7]. The long stiff rods, each composed of seven beads, represent cellulose microfibrils, that are connected by a network of stretchable crosslinks, standing for xyloglucans. The ratio between the number of rod beads and xyloglucan particles is 7:3. In our coarse-grained model, there are four types of interactions between: 1) beads within a rod (b-b), 2) beads in different rods (r-r), 3) xyloglucan particles and rod beads (x-r) and 4) xyloglucan particles (x-x). We have chosen these interactions with the following criteria:

i) the x-r bonding sets the scale of energy to that typical of a hydrogen bond,

ii) the rods have to be stiff, impenetrable, very long compared to typical bonding lengths, and the interactions between them are dominated by the interactions via xyloglucan particles,

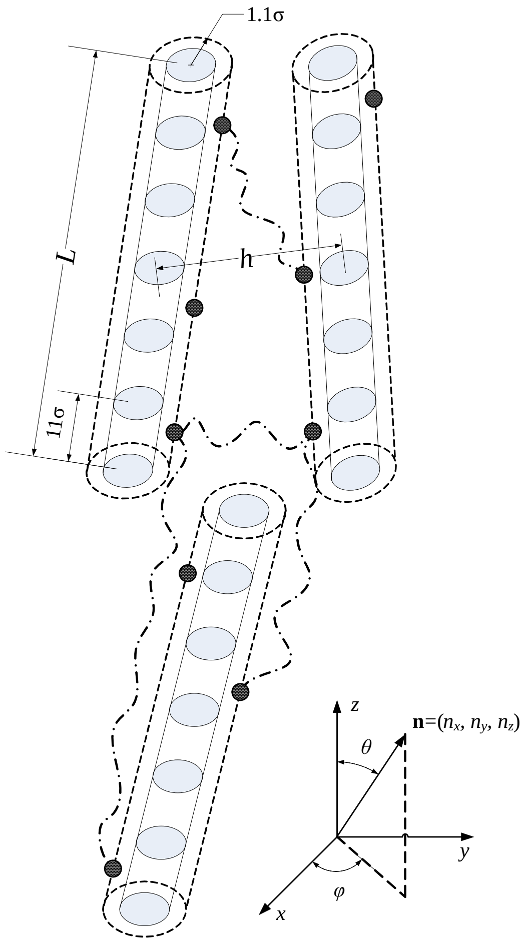

Figure 1.3: Schematic representation of our model for cellulose–xyloglucan network. Long stiff rods, formed by seven beads (grey spheres) represent cellulose microfibrils. Each x-particle (black sphere) interacts with the rod beads and with other two x-particles (see text) as indicated by the dashed-dotted wavy lines. The rods are closely packed, i.e. the equilibrium length of rod $L = 67.3\sigma$ is significantly larger than the equilibrium space between them $h = 4.5\sigma$. The rod director $\mathbf{n}$ is also indicated in cartesian and polar coordinates.

Table 1.1: Parameters of interaction potentials

Bond	Potential	Energy	Length	Cut-off radius $R_{c,s}$
b-b	U_{B}, $U_{\mathrm{LJ,b\text{-}b}}$	$A = 2500$, $\varepsilon_{\mathrm{b\text{-}b}} = 10$	$\sigma_{\mathrm{b\text{-}b}} = 10$	$R_{c,\mathrm{b\text{-}b}} = 15$
r-r	$U_{\mathrm{LJ,r\text{-}r}}$	$\varepsilon_{\mathrm{r\text{-}r}} = 0.001$	$\sigma_{\mathrm{r\text{-}r}} = 4$	$R_{c,\mathrm{r\text{-}r}} = 9$
x-r	$U_{\mathrm{LJ,x\text{-}r}}$	$\varepsilon_{\mathrm{x\text{-}r}} = 1 \equiv \varepsilon$	$\sigma_{\mathrm{x\text{-}r}} = 1 \equiv \sigma$	$R_{c,\mathrm{x\text{-}r}} = 2.3$
x-x triplets	U_{M}	$D = 0.05$	$r_{\mathrm{eq}} \in [20; 60]$	$b = 0.25\ \sigma^{-1}$ Eq. (1.4)
x-x all	$U_{\mathrm{LJ,x\text{-}x}}$	$\varepsilon_{\mathrm{x\text{-}x}} = 0.1$	$\sigma_{\mathrm{x\text{-}x}} = 1$	$R_{c,\mathrm{x\text{-}x}} = 1.12$

iii) the xyloglucan has to form a disordered network connecting different rods with the possibility of bond stretching, breaking and formation.

The last point is less straightforward than the previous steps and will be described in some details later on.

We describe most interactions by a Lennard-Jones potential of the form:

$$U_{\mathrm{LJ},s}(r) = 4\varepsilon_s\left[\left(\frac{\sigma_s}{r}\right)^{12} - \left(\frac{\sigma_s}{r}\right)^{6}\right] + C_s, \tag{1.1}$$

where ε_s and σ_s are specific Lennard–Jones parameters, characterising the energy and the length scales of intermolecular interactions, and the subscript $s = \{\text{b-b, x-r, r-r, x-x}\}$ labels the different interactions. The minimum of the potential, $-\varepsilon_s$, occurs at $r_{\mathrm{eq},s} = 2^{1/6}\sigma_s$. The constant C_s is chosen in such a way that the potential vanishes at $r = R_{c,s}$, where $R_{c,s}$ is a cut-off radius and $U_{\mathrm{LJ},s} = 0$ for $r > R_{c,s}$. The parameters are given in Table 1.1 in units of the characteristic energy and length scales of x-r interactions, $\varepsilon \equiv \varepsilon_{\mathrm{x\text{-}r}}$ and $\sigma \equiv \sigma_{\mathrm{x\text{-}r}}$. For bacterial cellulose, we choose $\varepsilon \approx 20$ kcal/mol $\approx 10^4$ K that describes a strong hydrogen x-r bonding [12], and $\sigma \approx 15$ nm that gives the typical radius of the microfibrils. Then, the equilibrium length of the rod is $L = 1\ \mu$m, which agrees with the typical length of cellulose microfibrils, and the equilibrium distance between them is $h = 67$ nm (Fig. 1.3). Moreover, the cut-off radius of $U_{\mathrm{LJ,x\text{-}r}}$ is chosen in such a way that each xyloglucan particle interacts with no more than one rod $R_{c,\mathrm{x\text{-}r}} = \frac{1}{2} r_{\mathrm{eq,r\text{-}r}}$ (Table 1.1).

In order to keep the rods rigid, we add to $U_{\mathrm{LJ,b\text{-}b}}$ a simple bending potential between the nearest beads within a rod given as

$$U_{\mathrm{B}} = A(1 + \cos\alpha), \quad \cos\alpha_i = \frac{(\mathbf{r}_{i-1} - \mathbf{r}_i, \mathbf{r}_{i+1} - \mathbf{r}_i)}{|\mathbf{r}_{i-1} - \mathbf{r}_i| \cdot |\mathbf{r}_{i+1} - \mathbf{r}_i|}, \tag{1.2}$$

where $A \gg 1$ (Table 1.1), $\mathbf{r}_i$ is the position of the bead i, with $i = 2$–6. This strong potential allows to decrease the cut-off radius $R_{c,\mathrm{b\text{-}b}}$ of $U_{\mathrm{LJ,b\text{-}b}}$ and lower the computational time.

We come now to the interactions between xyloglucan particles, which play the role of crosslinks between rods. To obtain a connected network of rods with effective long-range interactions, we require each xyloglucan particle to interact with two others. These

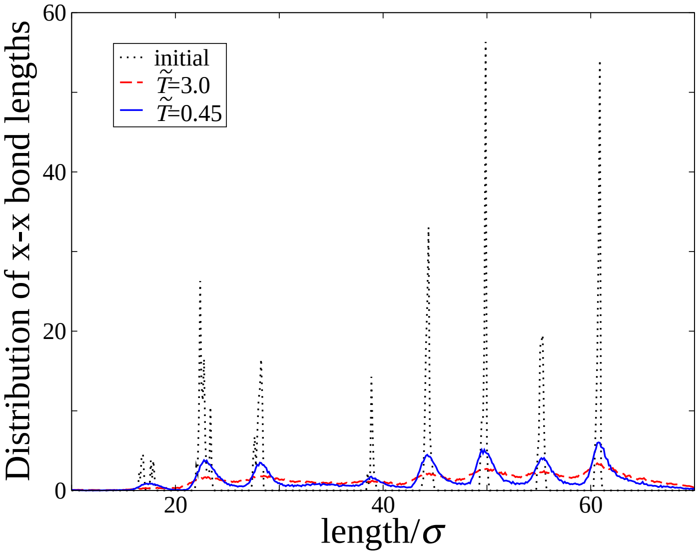

Figure 1.4: Bond length distribution of connected x-x triplets. Dotted line: initial sample providing the r_{eq}-distribution (see text); dashed and solid lines: equilibrated system around room temperature ($\widetilde{T} = 3.0$) and at low temperature ($\widetilde{T} = 0.45$), respectively.

triplets of connected particles are chosen once and for all at the beginning of the simulation as described in the following.

We place three x-particles per rod at the equilibrium distance of $U_{\mathrm{LJ,x\text{-}r}}$ from the second, fourth and sixth bead of each rod. For each x-particle we choose a first partner as the farthest x-particle within a radius L that is not yet assigned as partner of another particle. We repeat this procedure to assign the second partner. Once all triplets have been assigned, the distances between them in the initial structure are defined as equilibrium distance r_{eq} for the additional interaction between particles within a triplet described by a Morse potential

$$U_{\mathrm{M}} = D\big(1 - e^{-b(r-r_{\mathrm{eq}})}\big)^2, \tag{1.3}$$

with parameters D, b specified in Table 1.1. This means that every pair interacts through a potential with minimum at a different value of r_{eq}. As shown in Fig. 1.4, the initial r_{eq}-distribution contains eight sharp peaks. We further assume that a bond between x-x pairs can be broken if $U_{\mathrm{M}} \geqslant 0.9D$, which introduces a cut-off radius R_c^{M} for x-x interactions

$$R_c^{\mathrm{M}} = r_{\mathrm{eq}} - \frac{\ln(1-\sqrt{0.9})}{b} \simeq r_{\mathrm{eq}} + \frac{2.97}{b}. \tag{1.4}$$

1.4 What we may expect: frustration → glass formation

Our system is like a liquid crystal with the unit vector of rod orientation $\mathbf{n}$ (Fig. 1.3), playing the role of order parameter. In the absence of xyloglucan particles the system would energetically prefer to form a hexagonal crystal of parallel rods. We may expect that the presence of the long-range interactions between xyloglucan particles would introduce *frustration* i.e. incompatibility between locally preferred order and global constraints in the organisation of the rods. In other words, the energy of the system cannot be minimized by optimizing all local atomic interactions, since the atoms cannot simultaneously sit in the minima of all pairwise potentials [1, 4]. Some theoreticians believe [1, 4] that the frustration based approach can provide a physical mechanism for the formation of the *glassy* state, which is poorly defined concept. The phenomenology of the glass transition and general signatures of glassiness are described in Annotation 1.1. Such a glassy state is prone to minor changes of environment since even small external actions can transfer the system as a whole into a different metastable state, while never reaching thermodynamic equilibrium. Although there is a large arbitrariness in our construction of the interactions, we assume that frustration due to competing interactions is quite a general feature of non crystalline multicomponent systems like most of the living matter. The simple model of cellulose of section 1.3 is a good starting point to investigate these connections theoretically.

> Annotation 1.1 Glass
>
> There is no unique definition of a glass. In general : i) *Glasses* are disordered systems that lack the periodicity of crystals but behave mechanically like solids [13]; ii) *Glass* is a solid obtained by supercooling a liquid and that it is X-ray amorphous. Additionally a *glass*, when heated, should also exhibit a thermal characteristic known as the ‘glass transition’ [14]. The glass transition can be defined as the transition from liquid-like behaviour to the behaviour characteristic of amorphous solids. Conventionally, it corresponds to the temperature, where the viscosity $\eta = 10^{13.6}$ poise $[\mathrm{g \cdot cm^{-1} \cdot s^{-1}}]$ (water has a viscosity 0.0089 poise, olive oil has $\eta = 0.81$ poise and glycerol has $\eta = 15$ poise at 25 °C). The glass transition is often referred to as not thermodynamic nor even a dynamic transition, it is a point of dynamic arrest [4]. But there are unambiguous characteristics of glasses, where all theories and experiments agree, like the slowing down of relaxation and the cooperative behaviour on the mesoscopic scale. The slowing of relaxation processes implies that the system is not in a quasi-equilibrium local state but it travels restlessly among a huge variety of similar, energetically almost degenerate states actually without reaching the ground state, which is a crystal. Here we refer to a glassy state as a state with infinitely many local metastable configurations.

1.5 Simulation technique

Simulations of slow dynamics have to be conducted possibly over several decades in time. However this fact, together with the complexity of the interatomic potentials, limits the size of the system. In our simulation we use $N_{\mathrm{rod}} = 288$ rods, located in parallelepiped with 6 unit cells in the x and y directions and 14 in the z direction. In each unit cell, defined by vectors

$$\mathbf{i} = (6\sigma, 0, 0), \quad \mathbf{j} = (0, 6\sigma, 0), \quad \mathbf{k} = (0, 0, 11\sigma), \tag{1.5}$$

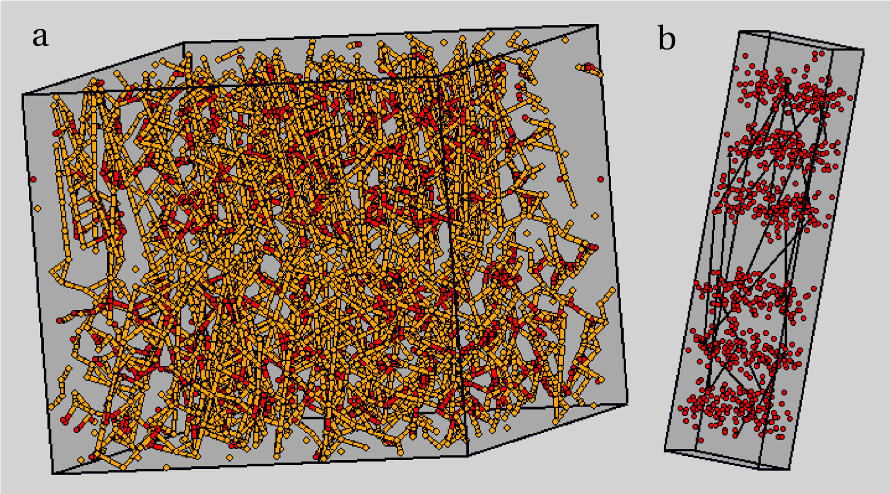

Figure 1.5: Snapshot of the system at $\widetilde{T} = 0.45$ in two representations. (a) Yellow balls and sticks: rods; red balls: xyloglucan particles. One can distinguish two layers of rods roughly oriented along the z direction. For illustration purposes the x and y sides of the box are multiplied by five. (b) The simulation box is shown with real relative dimensions. Only the x-particles (red balls) and a few of the bonds (black lines) within triplets are shown.

we put four beads at $(0.25, 0.25, 0.25)$, $(0.75, 0.75, 0.25)$, $(0.25, 0.75, 0.75)$, $(0.75, 0.25, 0.75)$. We form the rods by letting the beads interact with each other in groups of seven along the z direction, which implies two layers of densely packed rods along the z direction. In Fig. 1.5a we show a typical snapshot of the equilibrated system where the two layers of rods and the x-r bonds are visible, whereas in Figure 1.5b we show only the bonds between a few xyloglucan triplets.

First, the constructed configuration, composed of $N = 2880$ particles, was equilibrated at high temperature $T = 0.16\varepsilon/k_B$ in the microcanonical NVE ensemble. Using the velocity Verlet algorithm we integrate the equations of motion, where the mass of the rod bead is chosen as $m = 10^{-22}$ kg, being twice the mass of xyloglucan particle. The time step for integration is $\Delta t = 0.032\tau$, where $\tau = \sqrt{m\sigma^2/\varepsilon} \approx 0.5$ ns, which is the shortest period of vibrations between x-r particles. Then, the system was quenched with rate $3 \cdot 10^9$ K/s and studied in the NVT ensemble at $T = (3.0, 1.9, 0.9, 0.45, 0.23, 0.11) \cdot 10^{-2}\varepsilon/k_B$, using the Nose–Hoover chain thermostat (see e.g. [15], or classical papers [16, 17, 18, 19]). The masses of the thermostat chains were defined by $Q_1 = NT/\omega^2$ and $Q_2 = T/\omega^2$ with $\omega = 6.7$, the characteristic frequency of x-r vibrations. For convenience, in the following, we give the values of temperature in reduced units as $\widetilde{T} = 10^2 k_B T/\varepsilon$, where $\widetilde{T} = 3.0$ corresponds to room temperature.

The computer modelling allows us to study not only temperature effects, but also to vary the intermolecular interactions that are an intrinsic property of the system, and in experiment are given *a priori*. We use this advantage to compare the systems with weak x-r bonds ($\tilde{\varepsilon}_{\text{x-r}} = 0.1\varepsilon$) and broken x-x bonds ($D = 0$) to the original one (Table 1.1). By doing so, we separate the effect of xyloglucan network from the network of rods.

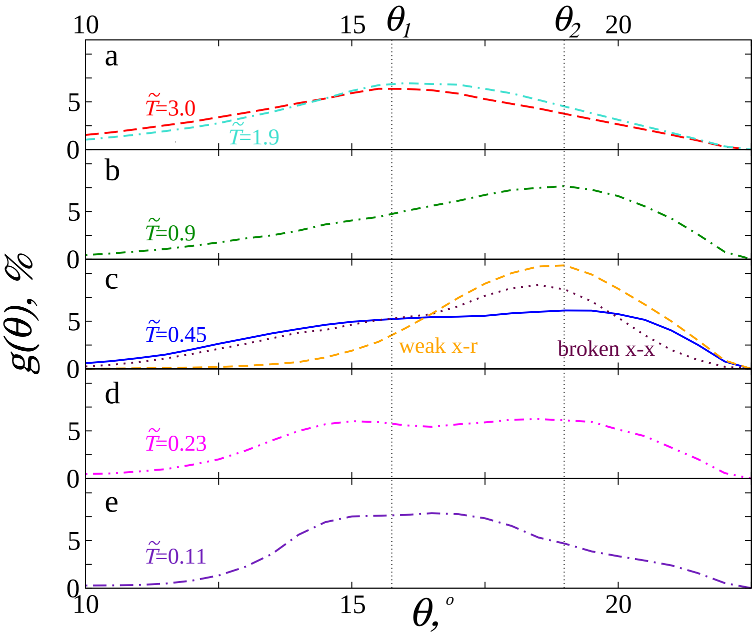

Figure 1.6: Polar angle distribution $g(\theta)$ of rod orientation for the indicated reduced temperatures. The dotted vertical lines at $\theta_1 \approx 16°$ and $\theta_2 \approx 19°$ indicate the two preferable orientations of the rods. In panel c ($\tilde{T} = 0.45$) the result for the system with weak x-r bonds (dashed line) and broken x-x bonds (dotted line) are shown as well.

1.6 Static fingerprints of the glassy state

In the polar system of coordinates the distribution functions $g(\theta)$ and $g(\varphi)$ for the polar θ and azimuthal φ angles (see Fig. 1.3), describe the static structure of the rods. These functions are defined as

$$g(x) = \frac{1}{MN_{\text{rod}}} \sum_{j=1}^{M} \sum_{i=1}^{N\text{rod}} \delta\left(x_i(t_j) - x\right), \qquad (1.6)$$

where $\delta(x_i - x)$ is the delta function, M and N_{rod} are the total number of time origins and rods, respectively.

The temperature dependence of the orientation distribution function $g(\theta)$ is shown in Fig. 1.6. At high temperatures ($\tilde{T} = 1.9, 3.0$) a broad angular distribution of rods orientation peaked at $\theta_1 \approx 16°$ results from the sampling by the system of a large part of the available microstates. As temperature decreases, a second preferable orientation of the rods at $\theta_2 \approx 19°$ appears, indicating some structural rearrangement below $\tilde{T} = 1.9$, clearly seen at $\tilde{T} = 0.9$. At lower $\tilde{T}$ both peaks become more pronounced, until at $\tilde{T} = 0.11$ they merge into a "plateau" around θ_1 and a peak at larger θ appears. A crossover between high and low temperature structures seems to occur between 1.9 and 0.9. This crossover is confirmed by looking at the azimuthal angle distribution $g(\varphi)$, shown in Fig. 1.7. We see that while three peaks are present at all temperatures, the relatively sharp peak at $\varphi = 225°$ for $\tilde{T} \leqslant 0.9$ determines a preferred orientation of the rods in the xy-plane. Consequently, both distribution functions suggest the appearance of additional order at low temperatures below $\tilde{T} = 1.9$ as observed at $T \leqslant 0.9$.

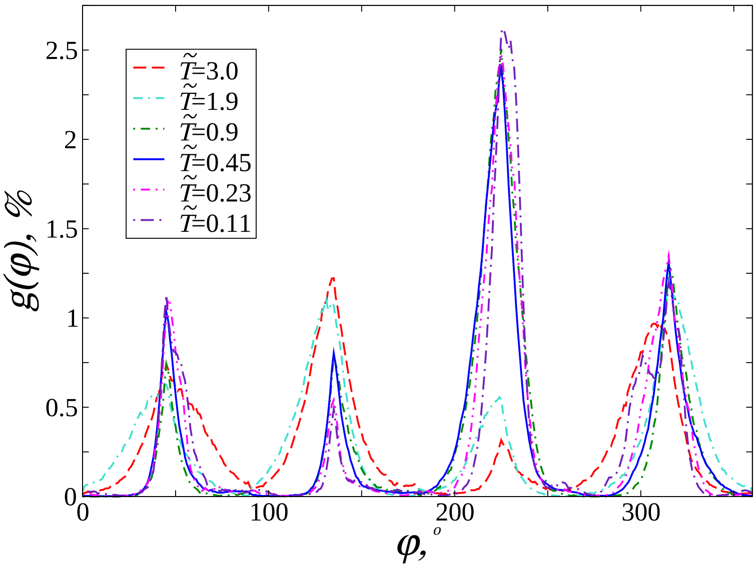

Figure 1.7: Azimuthal angle distribution $g(\varphi)$ of rod orientation for the indicated reduced temperatures. Notice the increase of the peak at $\varphi = 225°$ for $\widetilde{T} \leqslant 0.9$.

In order to single out the role of the xyloglucan network, we study two systems with broken x-x and with weak x-r bonds. The resulting distribution $g(\theta)$ for the system with broken x-x bonds is rather similar to the original one (Fig. 1.6c). However, for the system with weak x-r bonds, $g(\theta)$ has only one pronounced preferred orientation θ_2 (instead of being double-peaked), which suggests an easier reorientation of rods as for higher temperatures. Note that, the structure of the network of xyloglucan particles follows the structure of the rods, which is identified by Fig. 1.4, where the eight peaks in the distribution of x-particles are preserved for all studied temperatures (for example, we show $\widetilde{T} = 3.0; 0.45$). For low temperatures the distribution is sharper, suggesting that the network of xyloglucans is less flexible. The analysis of structural properties shows the strong influence of the xyloglucan network on the orientation of the rods, resulting in a broad or double peaked angular distribution, which is typical for glasses.

1.7 Slow relaxation

Mean-square displacement

The glassy behaviour, if it exists in our system, will be unmasked by studying the dynamic response or time dependent correlation functions. First, we consider the motion of the rods by calculating the mean-square displacement (MSD). In Fig. 1.8 we show the time dependence of the MSD = $\langle|\mathbf{r}(t) - \mathbf{r}(0)|^2\rangle$ of rod beads in log-log scale. Two regimes, the short-time behaviour and the long-time relaxation, are distinguished for all studied cases and each regime can be described by a power law, written as

$$\langle|\mathbf{r}(t) - \mathbf{r}(0)|^2\rangle = a \cdot t^b. \tag{1.7}$$

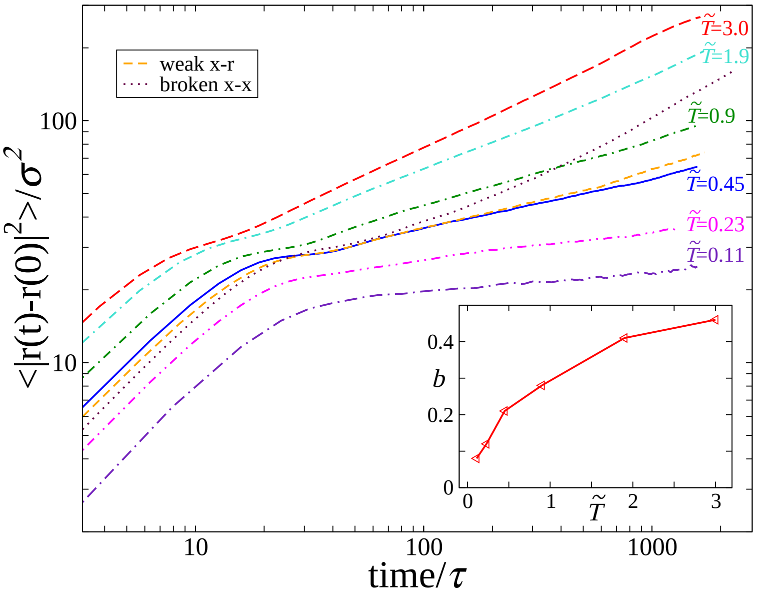

Figure 1.8: MSD of rods in log-log scale. The initial part, fast regime, is described by a power law with exponent $b \approx 0.8$ $\forall \widetilde{T}$, whereas the long-time behaviour is temperature dependent with exponent $b(\widetilde{T})$ given in the inset. Notice, that for all temperatures the dynamics is strongly subdiffusive ($b < 1$). The two time regimes are separated by a "plateau" at $\widetilde{T} = 0.9; 0.45$. The MSD for a system with broken x-x bonds is not well described by a power law for $t > 30\tau$, while weakening of x-r bonds changes only slightly the MSD at $\widetilde{T} = 0.45$.

The exponent b, like critical exponent, characterizes the motion of the particles, e.g. at short times it is common to find a ballistic motion with $b = 2$, while at long times the behaviour usually becomes diffusive with $b = 1$. The fit of the curves in Fig. 1.8 gives the temperature independent exponent $b \approx 0.8$ for the initial part $t < 20\tau$, which is much smaller than expected ballistic regime. In the inset we show the temperature dependence of $b(\widetilde{T})$ for the slow long-time behaviour of the rods, fitted for $t > 30\tau$. The diffusive regime, typical of liquids is never achieved in our simulations since, even at the highest temperature, the value of b is less than 0.5, signaling a slow glassy dynamics of the rods. Moreover, the appearance of a "plateau" between the two regimes for $\widetilde{T} = 0.9$ corresponds to the emergence of another structurally arrested state, where the rods are trapped by their neighbours. This confirms that $\widetilde{T} = 0.9$ is below the crossover temperature between two glassy phases. By fitting $b(\widetilde{T})$ (inset of Fig. 1.8) to a power-law we find $b(\widetilde{T}) \propto \sqrt{\widetilde{T}}$. By using this approximation, one can estimate the temperature typical of diffusive dynamics or 'warm liquid' for cellulose, which is $\widetilde{T} \approx 12$. We did not simulate such high temperatures, where most rods and xyloglucan bonds could be broken and such regime is not interesting for us. In everyday life boiled cellulose does not become liquid as well, but decomposes at high temperature, however this statement is too strong to relate it directly to our simple model. In this sense, we think that our system resembles more a solid rather than an overcooled liquid. We found the following influence of xyloglucan network on the MSD at $\widetilde{T} = 0.45$: weakening of x-r bonds changes only slightly the MSD, while broken x-x interactions change qualitatively the MSD behaviour and seem to suppress the subdiffusive dynamics.

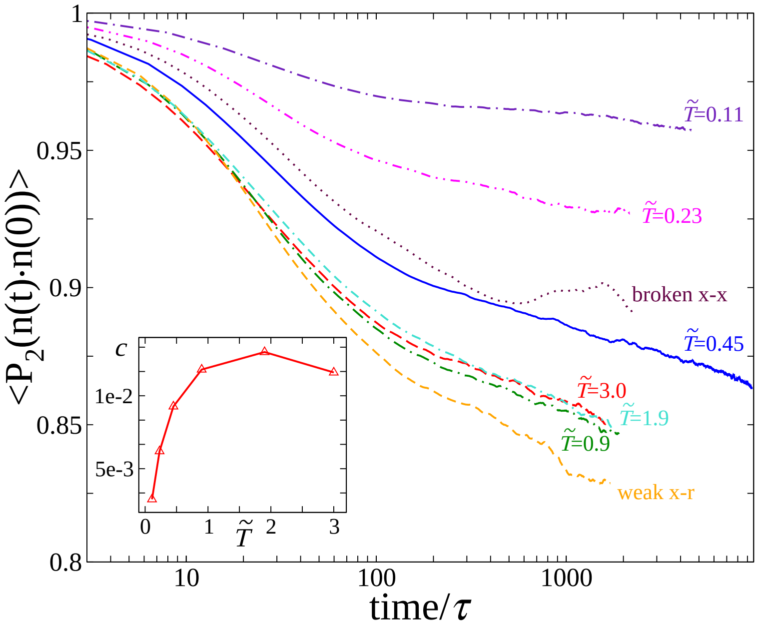

Figure 1.9: Orientational time correlation function of the rod director $\mathbf{n}$ (Eq. (1.8)). The initial decay is exponential, whereas the long-time decay shows slow logarithmic relaxation. The breaking of x-x bonds (dotted line) at $\widetilde{T} = 0.45$ eliminates the slow dynamics, while the weakening of x-r interactions (short-dashed line) leads to a higher value of $c \approx 0.017$ (Eq. (1.9)) and thus more explicit reorientation. Inset: the rate of change in rods orientation $c(\widetilde{T})$.

Orientational time correlation function

It is the change in orientation of cellulose microfibrils rather than the MSD, which is probed in creep and dielectric relaxation experiments [10, 11]. Let us now analyze the orientational time correlation function of the rods, given by

$$\left\langle P_2(\mathbf{n}(t)\cdot\mathbf{n}(0))\right\rangle = \frac{3}{2MN_{\text{rod}}}\sum_{j=1}^{M}\sum_{i=1}^{N_{\text{rod}}}\left(\mathbf{n}_i(t_j)\cdot\mathbf{n}_i(t_j+t)\right)^2-\frac{1}{2}, \tag{1.8}$$

where $P_2(x) = (3x^2-1)/2$ stands for the Legendre polynomial of the second kind. The function defined in Eq. (1.8) describes the self correlation of the director $\mathbf{n}_i$ between time 0 and t for a given rod i, then averaged over the number of rods N_{rod} and available time origins M. The correlation function of the rods orientation calculated within our model is shown in Fig. 1.9. Similar to MSD, it shows two distinct time regimes: an initial fast exponential and a slow logarithmic long-time relaxation. The logarithmic reorientation of rods, found over two time decays, is a characteristic feature of glassy dynamics. Similar logarithmic decay of correlators has been observed in Monte Carlo simulations for spin-glasses [20], colloids and micellar particles [21, 22], and overcooled liquids [23]. This slow dynamics is often explained in terms of mode-coupling theory [24, 25]. By fitting the calculated curves with the following expression

$$\left\langle P_2(\mathbf{n}(t)\cdot\mathbf{n}(0))\right\rangle = A - c\cdot\log t + p\cdot\exp(-t/\tau) \tag{1.9}$$

over the whole time interval (as an example see Fig. 1.10), we extract the value of the parameter c responsible for the slow dynamics. The temperature dependence of the fit-

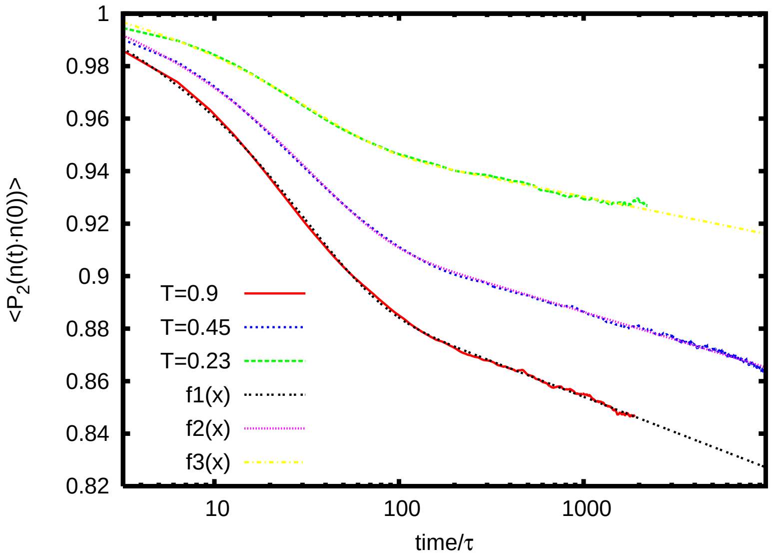

Figure 1.10: The fit of the orientational time correlation function $\langle P_2(\mathbf{n}(t)\cdot\mathbf{n}(0))\rangle$ with the expression Eq. (1.9) for $\widetilde{T} = 0.9; 0.45; 0.23$, chosen as an example.

ting parameter $c(\widetilde{T})$ is shown in the inset of Fig. 1.9. The curve $c(\widetilde{T})$ saturates for $\widetilde{T} > 0.9$, which is another sign of a structural rearrangement. What happens is that the ratio of the broken x-x bonds increases from 2% up to 6% at $\widetilde{T} = 3.0$. The increased number of broken bonds at higher temperature makes the system less frustrated preventing further increase of c with temperature. Nevertheless, the slow logarithmic reorientation dynamics persists also above the crossover temperature. Together with the data on strongly subdiffusive translational dynamics at all temperatures, this suggest a crossover between two types of structurally arrested glassy states like the one observed experimentally in a copolymer micellar system [26] and in a model system of hard spheres [27] and explained theoretically in [28, 29].

Our findings also suggest that the strength of x-r bonding has a profound effect on the reorientation of rods. Tenfold weakening of x-r interactions at $\widetilde{T} = 0.45$ results in a more pronounced change of $\langle P_2(\mathbf{n}(t)\cdot\mathbf{n}(0))\rangle$ than that due to an increase of temperature to $\widetilde{T} = 3.0$ (Fig. 1.9), but slow logarithmic dynamics is preserved. Conversely, breaking of x-x bonds ($D = 0$) leads to a non decaying behaviour of the orientation of rods and eliminates the slow dynamics completely.

1.8 Discussion

We have studied by means of Molecular Dynamics simulations a model that captures the main structural features of cellulose. We have shown that, in a wide range of temperatures, a slow dynamics results from the competition between the microfibrils interactions and the stretchable network of xyloglucan molecules. The slow dynamics is characterized by logarithmic time dependence of orientational correlators and by strongly subdiffusive dynamics of translational motion. These two features are robust and were observed for all temperatures investigated, around and below room temperature. Moreover, we have shown that weakening of the microfibril–xyloglucan interactions preserves the slow dynamics but influences the time scale of diffusion and reorientation. These findings are compatible with the observation of logarithmic creep motion in plant cell walls, also when in presence of LTP that weakens the hydrogen bonds in the network [10]. The loosening effect of LTP, rather than temperature, is thought to be one of the mechanisms that makes the extension of plant cell walls possible [10]. Indeed also in our model, variations of temperature around room temperature do not affect noticeably the slow dynamics in the way a weakening of x-r interaction does.

The complexity of our model produces an additional structural transition at low temperature. We find that a crossover between two glassy states, characterized by different angular distributions and parameters of slow dynamics. A similar glass–glass transition was found in copolymer micellar system [26]. We do not pursue further the study of the nature of this transition, that in our model occurs at low temperatures, not relevant for biological processes. However, the possibility of more than one structurally arrested state can be relevant for other related biopolymer networks.

Interestingly, the transition to a glassy state found in saccharides at low temperature [30] has been suggested to be the key factor in the protection of biological tissue against freezing. For these reasons, it is plausible to assume that living organisms should make use of substances with a broad variety of similar structures depending on external conditions, as offered by glassy materials. Evidence of slow glassy dynamics of the cytoskeleton of living cells was recently observed experimentally [31, 32, 33]. The simplest and, at the same time, one of the most important organic materials, cellulose, is a good starting point to investigate this possible connection theoretically.

Outlook

Let us put into perspective the main issues, which we did not address in our work, but that might be important for future research.

- We have mentioned the possible occurrence of a glass–glass transition in our system, however we did not explore entirely this point.Theoretically, for a model system composed of hard-spheres the transition between repulsive and attractive glasses happens at the volume fraction $\phi \approx 0.53$ when the relative width of the attractive well is smaller than 9 % [28, 29]. With a glass–glass transition, a small change in the external parameters could produce a remarkable change in the elastic properties of the material without any significant structural change [29]. In our model the glass-glass transition might be reproduced because of the complexity of interactions. The natural question to ask is how ubiquitous are these transitions in nature, where most of the systems are frustrated (with competing interactions). This point should be investigated both experimentally and theoretically.
- Our simulations describe a model system of cellulose without external forces. However, especially during growth, the cell wall is subjected to changes of turgor pres-

sure. The experimental observations, which consider the response of cellulose network to applied external forces, like strain in [10] or magnetic alignment in [34] are certainly worth to model. These modelling could give some insight into the mechanisms of the growth of plants that is still not understood completely.

- In numerous plant cell walls, the cellulose microfibrils self-assemble in a helicoidal pattern which resembles cholesteric liquid crystal order [35]. Analogous twisted arrangements are found in chitin and collagen networks [36], and the origin of such cholesteric order could be explained by the intrinsic chirality of the molecules. Therefore, it would be interesting to make a model of chiral cellulose, by adding a term responsible for the twist like in the theory of liquid crystals. However this would require systems with size much larger than the pitch of the twist.

Acknowledgements

We are grateful to C. Mariani for helpful discussions. This work was sponsored by the Stichting Nationale Computerfaciliteiten (National Computing Facilities Foundation, NCF) for the use of supercomputer facilities, with financial support from the Netherlandse Organisatie voor Wetenschappelijk Onderzoek (Netherlands Organization for Scientific Research, NWO).

2

Models of fluid membranes

Contents

The physics of membranes, two-dimensional layers of molecules, is very rich. The nature of interactions between molecules defines the order of the membrane, that can be in a fluid, hexatic or crystalline phase. In this thesis we consider only fluid membranes with zero shear modulus, meaning that the molecules can easily flow within a layer and adapt to changes of shape. The shape fluctuates, because the membranes have anomalously small surface tension or rather, because the energy of interactions between the constituents is of the order of $k_B T$. *The language of differential geometry turns out to be appropriate to describe the shape transformations of fluid membranes.*

2.1 Self-assembled membrane

Animal cells, unlike plants, do not have cell walls. Instead, they are surrounded by plasma membranes or biological membranes, which separate the interior of the cell from the exterior. To a first approximation, a biological membrane can be described as a bilayer of phospholipids like the one shown in Fig. 2.1. The phospholipid molecules are composed of one hydrophilic ('water loving') group and two hydrophobic ('water fearing') chains. Molecules, with one part being attracted and another part being repelled by water are called *amphiphilic* (see Fig. 2.2). Soaps and detergents are typical amphiphilic molecules, which consist of one hydrophilic group attached to a hydrocarbon chain. The molecules that contain two hydrophilic groups on both ends of hydrophobic skeleton are called bolaamphiphilic. They are synthesized to reproduce the monolayered membranes found in archaebacteria [37].

Above certain concentrations amphiphilic molecules self-assemble into a variety of struc-

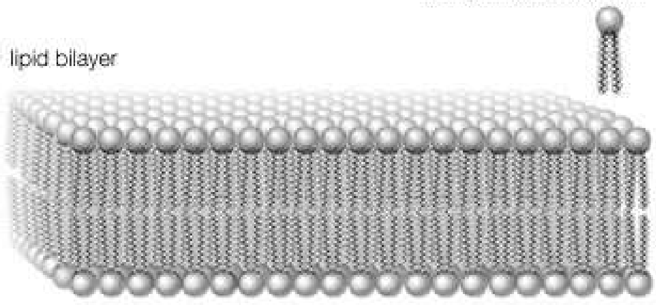

© 2007 Encyclopædia Britannica, Inc.

Figure 2.1: Lipid bilayer formed by phospholipid molecules in water [38]. Each molecule is composed of a hydrophilic group and two hydrophobic chains.

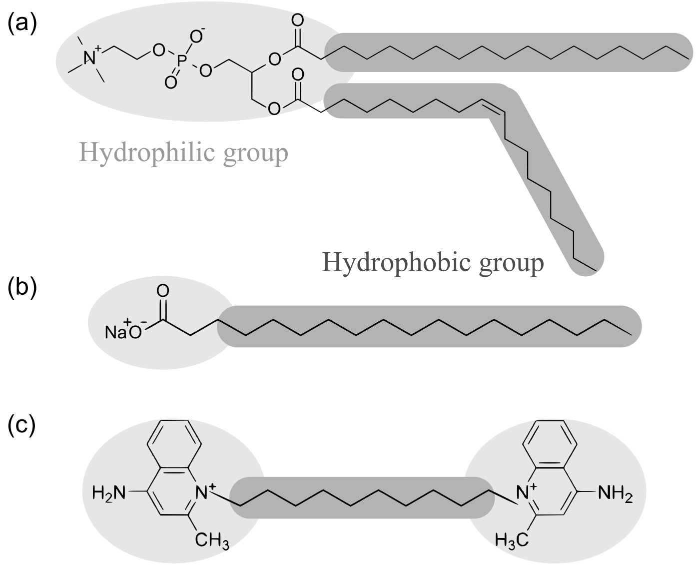

Figure 2.2: Examples of amphiphilic molecules. (a) Phosphatidylcholine, found in biological membranes; (b) Sodium stearate, the major component of soap; (c) Bolaamphiphilic molecule constituted by two symmetric hydrophilic end-groups. The name comes from the Argentinian bolas, two balls connected by a rope used to catch cattle.

tures [39] as for example shown in Fig. 2.3. The driving force for self-assembly is the necessity to minimize the free energy of the system water–amphiphilic molecules. This can be done by simultaneously maximizing the number of hydrogen bonds formed by the hydrophilic part with water and minimizing the contact of water with the hydrophobic part. The resulting equilibrium structures [40, 41, 42] basically depend on the concentration of molecules, the ratio of hydrophobic-to-hydrophilic part (packing parameter) and the temperature. Packing frustration arises from the competition between the packing areas of hydrophilic heads and hydrophobic tails, as well as from competing interactions between head groups and tails with the solvent. From a geometric point of view, if we denote by a the optimum area of the head group, by v the volume occupied by the hydrophobic chains and by l the chain length, then according to Israelachvili [43], the value of the packing parameter defined as $v/(al)$ gives an insight into the geometry of the structure. In order to form spherical micelles the packing parameter should be $v/(al) \lesssim 1/3$, for cylinders $1/3 < v/(al) \lesssim 1/2$ and for bilayers $v/(al) > 1/2$. The corresponding shapes of molecules, which satisfy these inequalities are shown in Fig. 2.3 next to the self-assembled structures. As we can see, the anisotropy in molecular shape gives rise to the curvature of the self-assembled structure and in general the following relation holds [44]

$$\frac{v}{al} = 1 + Hl + \frac{Kl^2}{3}, \tag{2.1}$$

where H is the mean curvature and K is the Gaussian curvature of the self-assembly, defined in the next section. Sometimes, an increase in temperature could be enough to induce the transition from flat lamellar phases to micellar phases, resulting from the change of molecular shape from cylindrical towards conical, because of the thermal fluctuations of hydrocarbon chain. As mentioned in the introduction, temperature plays an

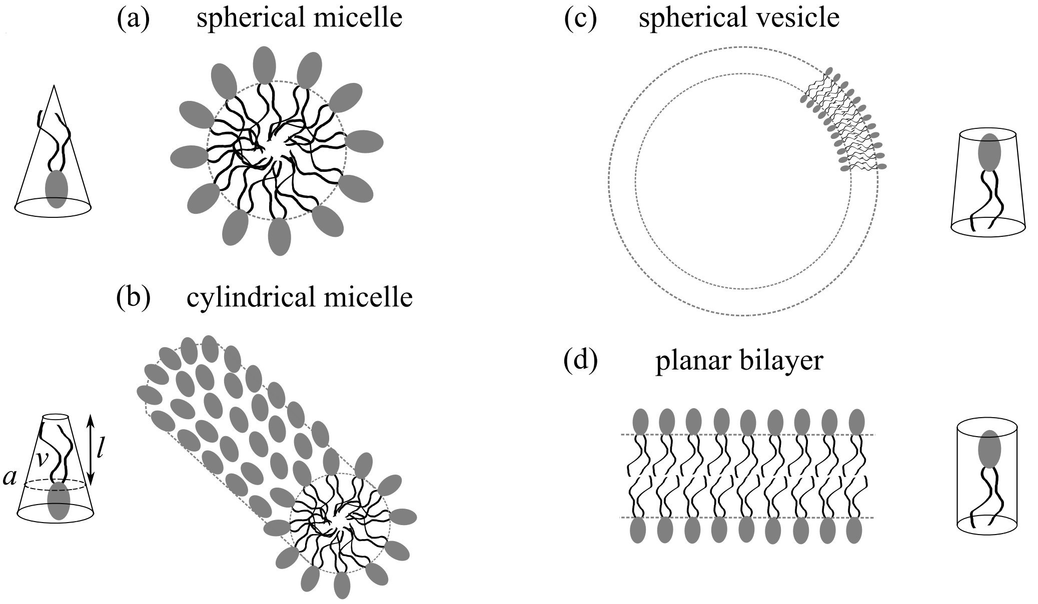

Figure 2.3: Structures self-assembled from amphiphilic molecules: (a) spherical micelles; (b) cylindrical micelles; (c) closed vesicle, which is spherical in the simplest case; (d) flat bilayer. We also show the approximate shapes of the packed amphiphilic molecules, such as cone ($v/(al) \lesssim 1/3$), truncated cones ($1/3 < v/(al) \lesssim 1/2$), and cylinder ($v/(al) > 1/2$).

important role for soft materials, because the typical energy of interactions between the constituents (e.g. self-assembled molecules) is of the order of $k_B T$. This means, that curved and fluctuating geometries become energetically accessible, and moreover that thermal fluctuations may lead to the disassembly of the molecules.

In solution, membranes may exist with open boundary, but it is more likely that they close and form *vesicles* (small bubbles) as shown in Fig. 2.3c. The typical thickness of the membrane is of the order of nanometers, that is much smaller than the characteristic size of the vesicle of the order of μm. Therefore we can neglect the thickness of the membrane and describe it as a truly two-dimensional surface embedded in the three-dimensional Euclidean space. Note, that such mathematical description is not valid for micelles, where the typical sizes are the same in all three dimensions. In this thesis, we will focus *only* on self-assemblies that can be described mathematically as smooth two-dimensional surfaces.

2.2 Differential geometry of surfaces

In this section, we introduce the necessary background of the differential geometry of surfaces, which is useful to fix the notations for the rest of the thesis. In particular, we define the metric and the curvature tensors of a surface and formulate the Gauss–Bonnet theorem connecting geometry and topology. Those who are familiar with the field, may omit the reading of this part and proceed to page 33. The interested readers are referred to the classical book *"Differential geometry of curves and surfaces"* by M. Do Carmo [45],

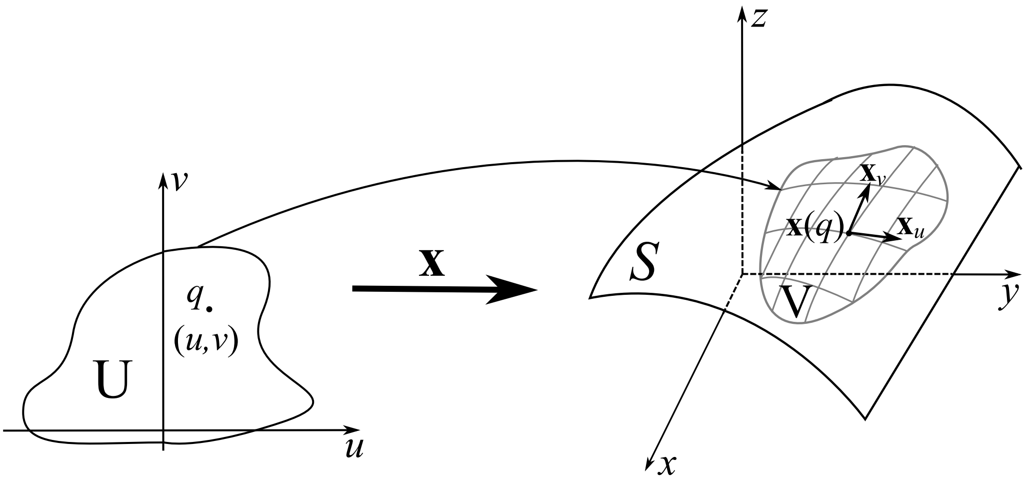

Figure 2.4: The map $\mathbf{x} : \mathrm{U} \to \mathrm{V} \cap S$ of an open set U into V is called a parametrization or a system of local coordinates in a neighbourhood of $\mathbf{x}(q)$.

which is also the main reference for this section. For the extensive introduction on differential geometry with examples from soft matter see R. D. Kamien [46] and lecture notes of F. David [47].

2.2.1 Regular surface

A surface or *two-dimensional manifolds* is a mathematical object. The word two-dimensional refers to the fact that we need two independent directions to define all the points around a given one. The space where we embed our surface is three-dimensional, which means that we need three numbers or *coordinates* to specify each point. A *parametrized* surface in $\mathbb{R}^3$ is characterized by a mapping $\mathbf{x} : \mathrm{U} \subset \mathbb{R}^2 \to \mathrm{V} \subset \mathbb{R}^3$ from an open set $\mathrm{U} \to \mathbb{R}^2$ into $\mathbb{R}^3$ as shown in Fig. 2.4. A map $\mathbf{x}$, which is a generalization of a function, assigns to every point in U with coordinates (u, v) exactly one point in V with coordinates

$$\mathbf{x}(u, v) = \big(x(u, v), y(u, v), z(u, v)\big). \tag{2.2}$$

In differential geometry we require that the functions x, y, z have continuous partial derivatives of all orders in U, so that set U is smooth and we can extend the notations of calculus to it. Let $\mathbf{x}_u = (\partial x/\partial u, \partial y/\partial u, \partial z/\partial u)$ indicates the tangent vector at $\mathbf{x}(q)$ (see Fig. 2.4) then the point $q \in \mathrm{U}$ is a *regular point* if and only if

$$(\mathbf{x}_u \times \mathbf{x}_v)(q) \neq 0, \tag{2.3}$$

where × denotes the vector product. To show that some surface S is regular, we need to i) guarantee the existence of a tangent plane at all points of S and ii) prevent self-intersection. It means that i) $\partial\mathbf{x}/\partial u \times \partial\mathbf{x}/\partial v \neq 0$ in every point of U, and ii) $\mathbf{x}$ has an inverse, which is continuous.

The surface may be *bounded* or unbounded. For example an infinite plane does not have a boundary, but a disc in the plane has the circle as a boundary. In general, for a

d-dimensional surface the dimension of the boundary is $d-1$, which is one for 2d surfaces. A sphere has no boundary, but it forms the boundary of a ball in three dimensions.

We say that the surface is *compact* or finite if it can be covered by a finite number of maps. Both sphere and torus are finite manifolds.

2.2.2 The first fundamental form (metric tensor)

Let us consider the distance on a regular surface $\mathbf{x}(u,v)$ between two points with coordinates (u,v) and $(u+du, v+dv)$, which we can write in the form

$$ds^2 = \left[\mathbf{x}(u+du, v+dv) - \mathbf{x}(u,v)\right]^2 = \langle \mathbf{x}_u, \mathbf{x}_u \rangle du^2 + 2\langle \mathbf{x}_u, \mathbf{x}_v \rangle du dv + \langle \mathbf{x}_v, \mathbf{x}_v \rangle dv^2 = \\ = E du^2 + 2F du dv + G dv^2. \quad (2.4)$$

This defines the first fundamental form (I f.f.) with the coefficients

$$E = \langle \mathbf{x}_u, \mathbf{x}_u \rangle = \left(\frac{\partial x}{\partial u}\right)^2 + \left(\frac{\partial y}{\partial u}\right)^2 + \left(\frac{\partial z}{\partial u}\right)^2, \quad (2.5a)$$

$$F = \langle \mathbf{x}_u, \mathbf{x}_v \rangle = \frac{\partial x}{\partial u}\frac{\partial x}{\partial v} + \frac{\partial y}{\partial u}\frac{\partial y}{\partial v} + \frac{\partial z}{\partial u}\frac{\partial z}{\partial v}, \quad (2.5b)$$

$$G = \langle \mathbf{x}_v, \mathbf{x}_v \rangle = \left(\frac{\partial x}{\partial v}\right)^2 + \left(\frac{\partial y}{\partial v}\right)^2 + \left(\frac{\partial z}{\partial v}\right)^2, \quad (2.5c)$$

where $\langle\ ,\ \rangle$ stands for the inner product, often also indicated by a dot (we will use both notations). Equation (2.4) can be rewritten in tensorial form as $ds^2 = g_{ij} du^i du^j$, $i, j = 1, 2$, with *metric tensor* g_{ij} defined by

$$g_{ij} = \frac{\partial \mathbf{x}}{\partial u^i} \cdot \frac{\partial \mathbf{x}}{\partial u^j}, \qquad (g_{ij}) = \begin{pmatrix} g_{11} & g_{12} \\ g_{21} & g_{22} \end{pmatrix} = \begin{pmatrix} E & F \\ F & G \end{pmatrix}. \quad (2.6)$$

For example, for the Euclidean plane $E = G = 1$, $F = 0$ and the metric is $ds^2 = dx^2 + dy^2$, for the sphere $E = r^2 \sin^2\theta$, $F = 0$ and $G = r^2$ and thus the metric is $ds^2 = r^2(d\theta^2 + \sin^2\theta d\phi^2)$.

Another important quantity that can be defined with the help of the I f.f. is the area of a bounded surface, which is

$$S = \iint_{(S)} dS, \qquad dS = |\mathbf{x}_u \times \mathbf{x}_v| du dv = \sqrt{EG - F^2} du dv. \quad (2.7)$$

Two surfaces are called *isometric* if their metric tensors or the coefficients of the I f.f. are equal. Cylinders and planes are isometric, so locally they are equivalent from the metric point of view (length, angle and area). It is not surprising, since by cutting a cylinder it may be unrolled into a plane.

It is always possible to parametrize the neighbourhood of any point of the regular surface in such a way that the coefficients of the I f.f. are

$$E = G = \lambda(u,v) > 0, \qquad F = 0. \quad (2.8)$$

Such coordinate system is called *isothermal or conformal*. Then the metric may be locally written as $g_{ij} = \lambda \delta_{ij}$, which means that any surface S is locally conformal to a plane and thus to any other regular surface.

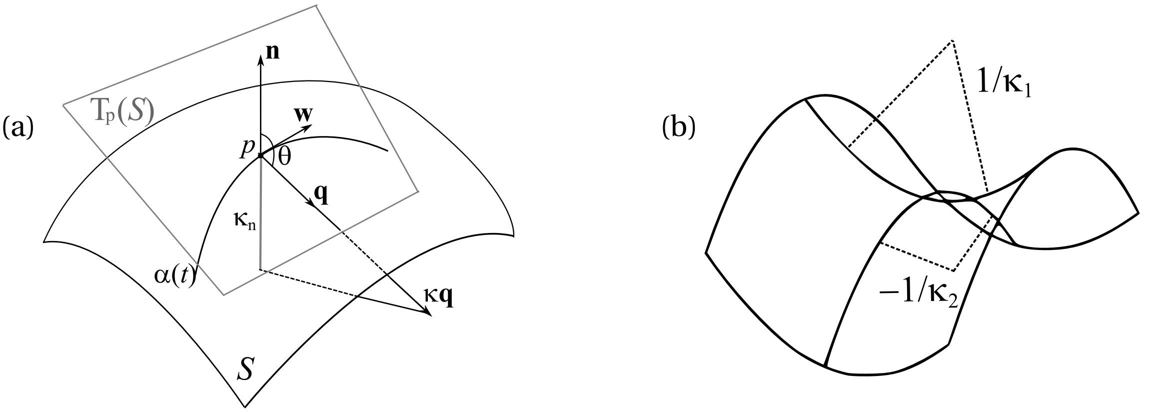

Figure 2.5: (a) $\alpha(t)$ is the regular curve in S passing through $p = \alpha(0) \in S$, $\mathbf{w} = \alpha'(0)$ is the tangent vector to S at the point p, $\kappa = |\alpha''(0)|$ is the curvature of α at p, and $\cos\theta = \langle \mathbf{q}, \mathbf{n} \rangle$, where $\mathbf{q} = \alpha''(0)/|\alpha''(0)|$ is the normal vector to α and $\mathbf{n}$ is the normal vector to S at p. The number $\kappa_n = \kappa \cos\theta$ is then called the normal curvature of $\alpha \subset S$ at p; (b) two principal directions with corresponding principal curvatures κ_1 and κ_2.

2.2.3 The second fundamental form (curvature tensor)

The I f.f. defines the intrinsic geometry of a surface like length, angle, area, while the second fundamental form (II f.f.) allows to examine its extrinsic properties, like its curvature in $\mathbb{R}^3$. Two surfaces may have the same metric tensors (isometric surfaces), but may be differently curved, like a plane and cylinder.

The geometry of the Gauss map

Given a parametrization $\mathbf{x} : \mathrm{U} \subset \mathbb{R}^2 \to S$ we can define the unit normal vector at each point $p \in \mathbf{x}(\mathrm{U})$ of the surface as

$$\mathbf{n}(p) = \frac{\mathbf{x}_u \times \mathbf{x}_v}{|\mathbf{x}_u \times \mathbf{x}_v|}(p). \tag{2.9}$$

Thus we obtain a map $\mathbf{n} : \mathbf{x}(\mathrm{U}) \to \mathbb{R}^3$ called *Gauss map*, which associates with each $p \in \mathbf{x}(\mathrm{U})$ the unit normal vector $\mathbf{n}(p)$. The surface is called *orientable* if the Gauss map can be extended differentially to the whole surface.

The plane normal to $\mathbf{n}$ at the point p is tangent to the surface S at p and is called the *tangent plane* $T_p(S)$. The quadratic form defined on the tangent plane $T_p(S)$ given by

$$\mathrm{II}_p(\mathbf{w}) = -\langle d\mathbf{n}(\mathbf{w}), \mathbf{w} \rangle, \qquad \mathbf{w} \in T_p(S) \tag{2.10}$$

is called the II f.f. of S at the point p. To give a geometric interpretation of the II f.f., consider a regular curve[1] $\alpha \subset S$, parametrized by $\alpha(t)$, with $\alpha(0) = p$. Then, since the tangent vector to S at the point p is $\mathbf{w} = \alpha'(0)$, we can rewrite Eq. (2.10) as

$$\mathrm{II}_p(\alpha'(0)) = -\langle d\mathbf{n}(\alpha'(0)), \alpha'(0) \rangle = -\langle \mathbf{n}'(0), \alpha'(0) \rangle \overset{\langle \mathbf{n}, \mathbf{w} \rangle = 0}{=} \langle \mathbf{n}, \alpha''(0) \rangle = \langle \mathbf{n}, \kappa \mathbf{q} \rangle = \kappa_n, \tag{2.11}$$

---

[1] A parametrized differentiable curve, defined as differentiable map $\alpha : \mathrm{I} \to \mathbb{R}^3$ of an open interval $\mathrm{I} = (a, b)$ into $\mathbb{R}^3$, is said to be regular if $\alpha'(t) \neq 0$ for all $t \in \mathrm{I}$.

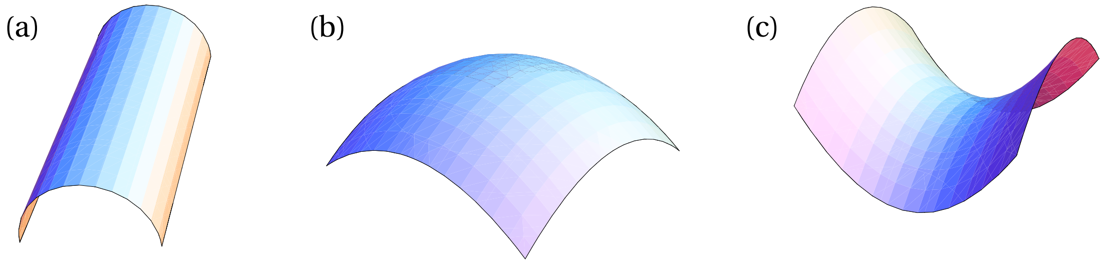

Figure 2.6: Cylinder $H > 0, K = 0$ (a), cap $H > 0, K > 0$ (b), and saddle $H = 0, K < 0$ (c), with parabolic, elliptic and hyperbolic points, respectively.

where κ is the curvature of α at p and κ_n is the projection of the vector $\kappa\mathbf{q}$ to the normal $\mathbf{n}$ at p, which is called the normal curvature (see Fig. 2.5a). The Meusner theorem states that all curves lying on a surface S and having at a given point $p \in S$ the same tangent line have at this point the same normal curvature κ_n.

The maximum normal curvature κ_1 and the minimum normal curvature κ_2 are called the *principal curvatures* at p; the corresponding directions, given by the eigenvectors $\mathbf{e_1}$, $\mathbf{e_2}$ of $d\mathbf{n}$ are called principal directions at p, so $d\mathbf{n}_p = \kappa_1\mathbf{e_1}$ and $d\mathbf{n}_p = \kappa_2\mathbf{e_2}$ (see Fig. 2.5b). The knowledge of principal curvatures allows us to compute the normal curvature along any direction $\mathbf{v} \in T_p(S)$. Since the vectors $\{\mathbf{e_1}, \mathbf{e_2}\}$ form an orthonormal basis of $T_p(S)$, we have $\mathbf{v} = \cos\theta\,\mathbf{e_1} + \sin\theta\,\mathbf{e_2}$ and the II f.f. in this basis is given by

$$\kappa_n = \mathrm{II}_p(\mathbf{v}) = \kappa_1\cos^2\theta + \kappa_2\sin^2\theta, \tag{2.12}$$

which is known as the *Euler formula*.

The determinant of $d\mathbf{n}_p$ is called *Gaussian curvature* K of S at p and the negative of half of the trace of $d\mathbf{n}_p$ is called *mean curvature* H of S at p. Thus, we can write

$$K = \det(d\mathbf{n}_p) = \kappa_1\kappa_2, \qquad H = \frac{1}{2}\mathrm{Tr}(d\mathbf{n}_p) = \frac{\kappa_1 + \kappa_2}{2}. \tag{2.13}$$

Points with positive Gaussian curvature are called elliptic points, with negative K are called hyperbolic, and those with zero K are called parabolic (see Fig. 2.6).

We can also define the mean curvature H and the Gaussian curvature K in a compact tensorial form, starting from the the curvature tensor $\kappa_{ij} = -\mathbf{n}\cdot\partial_i\partial_j\mathbf{x}$, which is actually the II f.f. Then

$$2H = \mathrm{Tr}\left(\kappa_i^j\right) = g^{ij}\kappa_{ij}, \tag{2.14a}$$

$$2K = 2\det\left(\kappa_i^j\right) = \left(\kappa_i^i\kappa_j^j - \kappa_i^j\kappa_j^i\right) = 4H^2 - K^{ij}\kappa_{ij}, \tag{2.14b}$$

where $g^{ij} = (g_{kl}^{-1})_{ij}$ and $\kappa_i^j = \kappa_{il}g^{lj}$. For completeness, we write also the expressions of H and K in terms of the unit normal vector $\mathbf{n}$, which are

$$2H = -\,\mathrm{div}\,\mathbf{n} = -\nabla_i n_i, \tag{2.15a}$$

$$2K = \mathrm{div}(\mathbf{n}\,\mathrm{div}\,\mathbf{n} + \mathbf{n}\times\mathrm{rot}\,\mathbf{n}) = (\nabla_i n_i)^2 - \nabla_i n_j \nabla_j n_i. \tag{2.15b}$$

The choice of one or another expression of H and K depends on the situation. We make use of Eqs. (2.14) in Appendix B to find the variation of free energy around the sphere. On the other hand, by using Eqs. (2.15) in the last chapter of this thesis, we rewrite the free energy of liquid crystals as a functional of a curvature.

The Gauss map in a local system of coordinates

We introduced the II f.f. and the principal curvatures in general form, without referring to a particular parametrization. However, for computational as well as for theoretical purposes, it is important to express all concepts in the local system of coordinates. Then the expression of the II f.f. in the basis $\{\mathbf{x}_u, \mathbf{x}_v\}$ is given by

$$\mathrm{II}_p = -\langle \mathbf{n}_u du + \mathbf{n}_v dv, \mathbf{x}_u du + \mathbf{x}_v dv \rangle = e\,du^2 + 2f\,du dv + g\,dv^2 \tag{2.16}$$

where, since $\langle \mathbf{n}, \mathbf{x}_u \rangle = 0$ and $\langle \mathbf{n}, \mathbf{x}_v \rangle = 0$, the coefficients can be recast in the form

$$e = -\langle \mathbf{n}_u, \mathbf{x}_u \rangle = \langle \mathbf{n}, \mathbf{x}_{uu} \rangle = \frac{(\mathbf{x}_u, \mathbf{x}_v, \mathbf{x}_{uu})}{\sqrt{EG-F^2}}, \tag{2.17a}$$

$$f = -\langle \mathbf{n}_u, \mathbf{x}_v \rangle = \langle \mathbf{n}, \mathbf{x}_{vu} \rangle = \langle \mathbf{n}, \mathbf{x}_{uv} \rangle = -\langle \mathbf{n}_v, \mathbf{x}_u \rangle = \frac{(\mathbf{x}_u, \mathbf{x}_v, \mathbf{x}_{uv})}{\sqrt{EG-F^2}}, \tag{2.17b}$$

$$g = -\langle \mathbf{n}_v, \mathbf{x}_v \rangle = \langle \mathbf{n}, \mathbf{x}_{vv} \rangle = \frac{(\mathbf{x}_u, \mathbf{x}_v, \mathbf{x}_{vv})}{\sqrt{EG-F^2}}, \tag{2.17c}$$

The derivatives of the normal $\mathbf{n}_u$ and $\mathbf{n}_v$ belong to the tangent plane, therefore in the basis $\{\mathbf{x}_u, \mathbf{x}_v\}$ we can write

$$\mathbf{n}_u = a_{11}\mathbf{x}_u + a_{12}\mathbf{x}_v, \tag{2.18 a}$$

$$\mathbf{n}_v = a_{21}\mathbf{x}_u + a_{22}\mathbf{x}_v, \tag{2.18 b}$$

which are also known as equations of *Weingarten*. The matrix (a_{ij}) is not necessarily symmetric unless $\{\mathbf{x}_u, \mathbf{x}_v\}$ is an orthonormal basis. Combining Eqs. (2.5),(2.17) and (2.18) we can write in matrix form the following relation

$$-\begin{pmatrix} e & f \\ f & g \end{pmatrix} = \begin{pmatrix} a_{11} & a_{12} \\ a_{21} & a_{22} \end{pmatrix} \begin{pmatrix} E & F \\ F & G \end{pmatrix}, \tag{2.19}$$

whence the coefficients of the matrix (a_{ij}) of $d\mathbf{n}$ in the basis $\{\mathbf{x}_u, \mathbf{x}_v\}$ are given by

$$a_{11} = \frac{fF - eG}{EG-F^2}, \qquad a_{12} = \frac{gF - fG}{EG-F^2}, \tag{2.20a}$$

$$a_{21} = \frac{eF - fE}{EG-F^2}, \qquad a_{22} = \frac{fF - gE}{EG-F^2}. \tag{2.20b}$$

The principal curvatures κ_1 and κ_2 are the eigenvalues of the matrix (a_{ij}), thus

$$K = \det(a_{ij}) = \frac{eg - f^2}{EG-F^2}, \tag{2.21a}$$

$$H = \frac{1}{2}\mathrm{Tr}(a_{ij}) = -\frac{1}{2}\frac{eG - 2fF + gE}{EG-F^2}. \tag{2.21b}$$

The application of these formulas is considered in Annotations 2.1 and 2.2, where we compute the mean and the Gaussian curvatures for two general examples.

Annotation 2.1 Surface of revolution

Consider a surface of revolution parametrized by

$$\mathbf{x}(u,v) = \big(f(v)\cos u,\, f(v)\sin u,\, g(v)\big), \qquad a \leqslant v \leqslant b, \quad 0 \leqslant u \leqslant 2\pi. \tag{2.22}$$

We find the normal vector by using Eq. (2.9) straightforwardly

$$\mathbf{n} = \frac{1}{f\sqrt{(f')^2+(g')^2}} \begin{pmatrix} \mathbf{i} & \mathbf{j} & \mathbf{k} \\ -f\sin u & f\cos u & 0 \\ f'\cos u & f'\sin u & g' \end{pmatrix} = \frac{(g'\cos u,\, g'\sin u,\, -f')}{\sqrt{(f')^2+(g')^2}}, \tag{2.23}$$

where $'$ denotes the derivative with respect to v. The coefficients of the I f.f. are found with the help of Eq. (2.5)

$$E = f^2, \quad F = 0, \quad G = (f')^2 + (g')^2. \tag{2.24}$$

The coefficients of the II f.f. can be expressed explicitly with the aid of Eq. (2.17)

$$e = \frac{-fg'}{\sqrt{(f')^2+(g')^2}}, \tag{2.25a}$$

$$f = 0, \tag{2.25b}$$

$$g = \frac{f''g' - f'g''}{\sqrt{(f')^2+(g')^2}}. \tag{2.25c}$$

If a parametrization of a regular surface is such that $F = f = 0$, then the principal curvatures are given by $\kappa_1 = e/E$, $\kappa_2 = g/G$. For the surface of revolution the mean and the Gaussian curvatures are given as

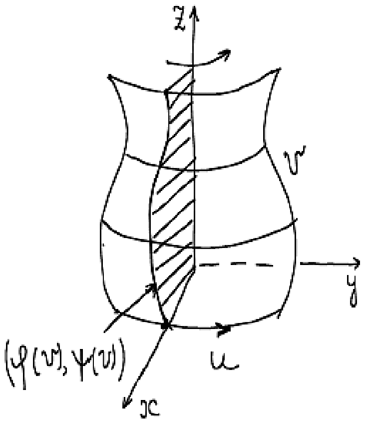

Figure 2.7: Surface of revolution is obtained by rotating a regular curve C, parametrized as $(f(v), g(v))$ in the xz plane, about z axis. Meridians $u = \text{const}$ and parallels $v = \text{const}$.

$$K = \frac{eg}{EG} = \frac{-g'(f''g' - f'g'')}{f[(f')^2+(g')^2]^2}, \tag{2.26a}$$

$$H = \frac{1}{2}\left(\frac{e}{E} + \frac{g}{G}\right) = \frac{1}{2}\left(\frac{-g'}{f\sqrt{(f')^2+(g')^2}} + \frac{f''g' - f'g''}{[(f')^2+(g')^2]^{3/2}}\right). \tag{2.26b}$$

Annotation 2.2 Monge parametrization

Consider the surface given in the Monge form

$$\mathbf{x}(u,v) = \big(u,\ v,\ h(u,v)\big), \quad (u,v) \in \mathrm{U} \subset \mathbb{R}^2, \tag{2.27}$$

where $h(u,v)$ is a differentiable function. A simple calculation using Eq. (2.9) shows that

$$\mathbf{n} = \frac{(-h_u, -h_v, 1)}{\sqrt{1+h_u^2+h_v^2}}. \tag{2.28}$$

The coefficients of the I f.f. (Eq. 2.5) can be found explicitly as

$$E = 1+h_u^2, \quad F = h_u h_v, \quad G = 1+h_v^2, \tag{2.29}$$

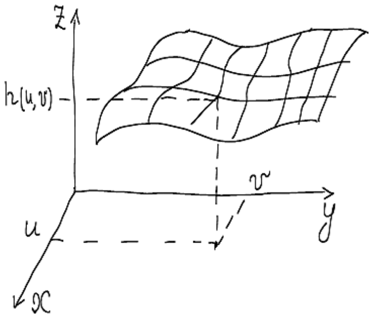

Figure 2.8: The function $h(u,v)$ specifies the height of the surface above the base plane (u,v).

and the coefficients of the II f.f. (Eq. 2.17) are given by

$$e = \frac{h_{uu}}{\sqrt{1+h_u^2+h_v^2}}, \qquad f = \frac{h_{uv}}{\sqrt{1+h_u^2+h_v^2}}, \qquad g = \frac{h_{vv}}{\sqrt{1+h_u^2+h_v^2}}. \tag{2.30}$$

Combining the above expressions with Eq. (2.21) we obtain the mean and the Gaussian curvatures

$$K = \frac{h_{uu}h_{vv} - h_{uv}^2}{(1+h_u^2+h_v^2)^2}, \tag{2.31a}$$

$$H = \frac{(1+h_u^2)h_{vv} - 2h_u h_v h_{uv} + (1+h_v^2)h_{uu}}{(1+h_u^2+h_v^2)^{3/2}}. \tag{2.31b}$$

2.2.4 Geometry and topology

The knowledge of the first and the second fundamental forms defines the local properties or geometry of the surface, like distance, angle, and curvature. The properties that do not change under stretching or small deformations of the surface belong to the topology. For example, a pear, an apple and a round sphere are topologically equivalent, because they can be transformed into one another by bending and stretching (twisting can also be added) without ripping. But a pear, an apple and a round sphere are not the same from a geometric point of view, because their metrics are different.

We have seen that H and K depend on the normal vector $\mathbf{n}$ of the surface. However, it turns out, that the Gaussian curvature can be determined by measuring only the lengths and the angles without the knowledge of $\mathbf{n}$, and thus it is an intrinsic property of the surface. As we will see in the following, the Gauss–Bonnet theorem establishes the relation between the total Gaussian curvature and the topology of the surface.

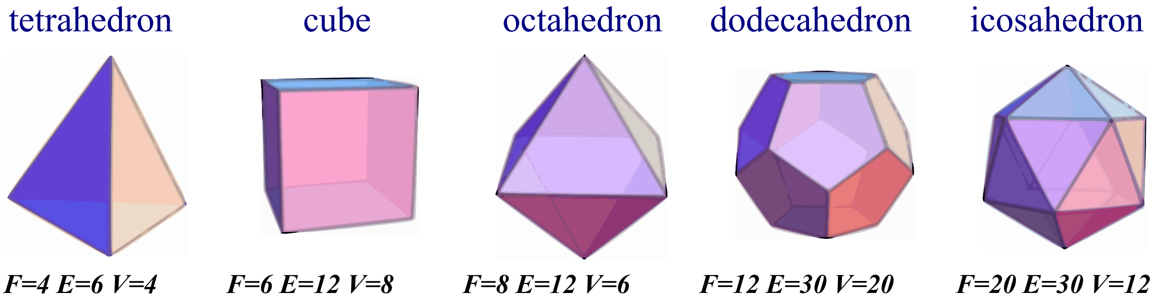

Figure 2.9: Polyhedra of the highest symmetry, with different number of faces F, edges E and vertices V, but the value of Euler characteristic $\chi = F - E + V = 2$ is the same.

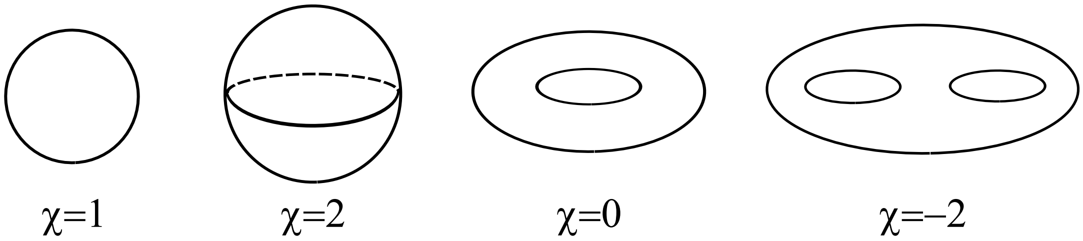

Figure 2.10: From left to right: disc, sphere, torus (sphere with one handle) and double torus (sphere with two handles).

The invariant that describes the topology of the surface is called the *Euler–Poincare characteristic* χ, which is a generalisation of the Euler characteristic for polyhedrons (see Fig. 2.9) defined as

$$\chi = F - E + V, \tag{2.32}$$

where F denotes the number of faces, E denotes the number of sides edges and V denotes the number of vertices of polyhedron. We can extend the concept of χ to any compact surface S, by dividing the surface into a finite family of triangles. The Euler characteristic χ does not depend on the triangulation of the surface, but only on the topology of the surface. For a disc $\chi = 1$, for a sphere $\chi = 2$, for a torus $\chi = 0$, for double torus $\chi = -2$ (see Fig. 2.10). Two surfaces are called *homeomorphic* or topologically isometric if they have the same χ. For example, all convex polyhedra are homeomorphic to a sphere. In general, every compact connected surface S is homeomorphic to a sphere with a certain number g of handles. The number

$$g = \frac{2-\chi}{2}, \qquad \chi = 2(1-g). \tag{2.33}$$

is called the *genus* of S. So we can calculate the Euler characteristic $\chi(S)$ from the genus g of S.

The *Gauss–Bonnet theorem* establishes the connection between the local geometry and the topology of the surface. It states that for orientable compact surface surface S, the integral of the Gaussian curvature is topological invariant

$$\iint_S K\, dS = 2\pi\chi(S), \tag{2.34}$$

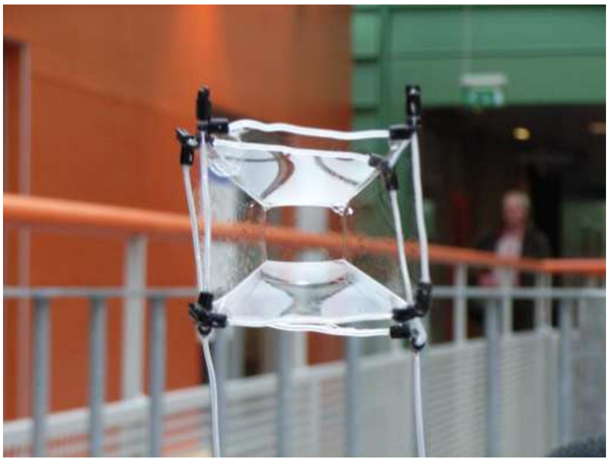

Figure 2.11: A soap film is the physical realization of minimal surfaces, which have the least area for a given boundary, like the cube at the photo. Soap films always meet in threes at 120° and four edges meet at the vertex at $\arccos(-1/3) = 109^\circ\ 28'$ angle.

namely if one deforms or bends the surface the integral in Eq. (2.34) does not change, while the curvature K at some points does.

2.3 Soap films and soap bubbles

We begin by considering soap films as the simplest example to apply the notions of differential geometry. The soap film is in essence a surface or interface composed of two soap monolayers with water in between. The typical thickness of soap films is of the order of a micron. The soap molecules, like the one shown in Fig. 2.2b, are pointing towards the air with their hydrophobic tails, whereas hydrophilic parts are surrounded by water. Because of the dynamic processes referred as thinning and draining (expelling of water), some parts of the film could become extremely thin ~ 10 nm, reducing to two soap monolayers sandwiching a few molecules of water [48, 49]. Here we consider thick films ($\sim 1\ \mu$m), when macroscopic quantities, such as surface tension is the dominant contribution.

In order to create the surface one needs to supply an energy or free energy to the system, which is proportional to the area of interface

$$\mathscr{F}_S = \sigma \iint_{(S)} dS, \tag{2.35}$$

where σ is called *surface tension*. The surface tension σ is a direct measure of the energy required to increase the area by one unit, $\sigma = \left(\partial\mathscr{F}/\partial S\right)_{T,V}$. It can be estimated as $\sigma \simeq U/(2D^2)$, where U is the cohesive energy per molecule and D is the size of the molecule, which gives the following values: for water $\sigma = 73$ mJ/m^2 at 20°C, for mercury $\sigma \approx 500$ mJ/m^2, for most oils with $U \simeq k_B T$, $\sigma \approx 20$ mJ/m^2 [49].

In the middle of the 19th century the Belgian physicist Joseph Plateau did experiments with soap films trying to understand the molecular forces in liquids [50]. By dipping a

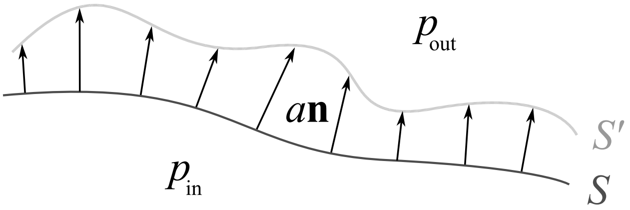

Figure 2.12: By translating every point of the reference surface S along the normal $\mathbf{n}$ by a (not necessarily constant), results in the target surface S'. Notice, that the translation in the plane of the surface along tangent vector, would not result in the change of shape.

bent wire into a soap solution and then pulling it back he manufactured beautiful structures, like the one shown in Fig. 2.11. Since the surface tension is the only force (except gravity), soap film acquires a minimum area, in order to minimize the free energy Eq. (2.35). One may ask the question what is the equilibrium shape of soap films. In equilibrium, the free energy is stationary, and thus the first variation of free energy should be zero

$$\delta\mathscr{F}_S = \sigma\delta\iint dS = 0. \tag{2.36}$$

Let us consider the parallel transport of the surface S with parametrization $\mathbf{x}(u,v)$ along the normal $\mathbf{n}(u,v)$, which corresponds to the real change of the shape. The resulting surface S' is given by $\mathbf{x}'(u,v) = \mathbf{x}(u,v) + a(u,v)\mathbf{n}(u,v)$, where $a(u,v)$ is small (see Fig. 2.12). The area element of a perturbed surface can be expressed directly by using Eq. (2.7)

$$\begin{aligned} dS' &= \left|(\mathbf{x}_u + a\mathbf{n}_u + a_u\mathbf{n}) \times (\mathbf{x}_v + a\mathbf{n}_v + a_v\mathbf{n})\right| du\,dv \overset{\text{Eq. (2.9)}}{=} \\ &= \left|\mathbf{x}_u \times \mathbf{x}_v + a(\mathbf{n}_u \times \mathbf{x}_v + \mathbf{x}_u \times \mathbf{n}_v) + a^2\mathbf{n}_u \times \mathbf{n}_v\right| du\,dv \overset{\text{Eq. (2.18)}}{=} \\ &= |\mathbf{x}_u \times \mathbf{x}_v|\left[1 + a(a_{11} + a_{22}) + a^2(a_{11}a_{22} - a_{12}a_{21})\right] du\,dv \overset{\text{Eq. (2.21)}}{=} \\ &= dS(1 + 2aH + a^2K). \end{aligned} \tag{2.37}$$

This result allows us to express the first variation of the free energy as

$$\delta\mathscr{F}_S = \sigma\iint dS\,2aH = 0 \quad \Longrightarrow \quad H \equiv 0. \tag{2.38}$$

The surface with zero mean curvature at every point is called *minimal surface*. Soap films are physical realizations of minimal surfaces. The mathematical problem of finding a surface of minimal area with a given boundary is named after Joseph Plateau.

Now consider a soap bubble, which is soap film with no boundaries. The free energy for such closed surface is composed of two terms, namely the surface tension and the volume term

$$\mathscr{F}_{S,V} = \sigma\iint dS + \Delta p\iiint dV, \tag{2.39}$$

where $\Delta p = p_{\text{out}} - p_{\text{in}}$ is the pressure difference across the interface of the bubble. In equilibrium, the variation of the free energy

$$\delta\mathscr{F}_{S,V} = \iint dS\,a(2\sigma H + \Delta p) \tag{2.40}$$

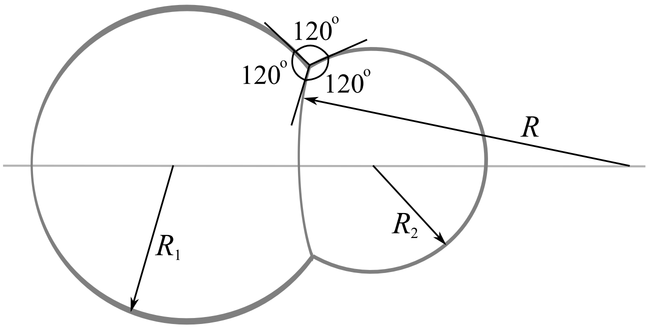

Figure 2.13: The double bubble is the unique surface of least area; it is composed of three spherical caps with the curvature of partition being the difference of the curvatures of two bubbles $1/R = 1/R_2 - 1/R_1$, which is a direct consequence of the Laplace–Young law.

vanishes and we get the following condition $\Delta p = -2\sigma H$ known as the Laplace–Young law. This condition means that in equilibrium soap bubble has $H = \text{const}$, and thus, due to Alexandroff's theorem [45], it is a *sphere*. It is not surprising, since among all surfaces, spheres have the least area to enclose and separate a given volume[2]. From the Laplace–Young law follows that the radius of soap bubbles or oil droplets in water is $R = 2\sigma/\Delta p$, which also means that the smaller the bubble the greater its inner pressure and thus by connecting two bubbles of different sizes, the smaller one empties itself into the larger one, because of this pressure excess [49].

To find the area-minimizing shape for a collection of soap bubbles (foam) is a deep mathematical problem. Recently, it has been solved for the case of two bubbles [51]. The double bubble shown in Fig. 2.13, consisting of three spherical caps meeting along a common circle at 120° angle, has the smallest area to enclose and separate two given volumes. In chapter 4 we will come back to the double bubble shape formed by bilayer membranes. The problem of identifying the surface with the least area, separating more than two volumes is not yet rigorously solved.

2.4 Phenomenological models of membranes and vesicles

Membranes (vesicles) made of two-dimensional sheets of molecules, differ from soap films (soap bubbles) by their thickness (about 10 nm $\ll$ 1 μm) and elastic properties. Vesicles display a striking variety of experimentally observed equilibrium shapes. In particular, they exhibit non-spherical, toroidal or biconcave discoidal geometries, like the ones shown in Fig. 2.14. The surface tension, which was successfully used to explain the spherical shapes of soap bubbles or liquid droplets, is irrelevant for fluid membranes. In fluid membranes the molecules can easily flow and freely adjust the total area of the membrane to the one corresponding to the best packing, which gives the condition of thermodynamic equilibrium as $\partial\mathscr{F}/\partial S = 0$. Then the surface tension $\sigma = \left(\partial\mathscr{F}/\partial S\right)_{T,V}$ is zero or at least anomalously small, yielding the possibility of long-range fluctuations of

---

[2] It took mathematicians about 2000 years, from the times of Archimedes until H. A. Schwarz 1884, to prove this long-standing conjecture.

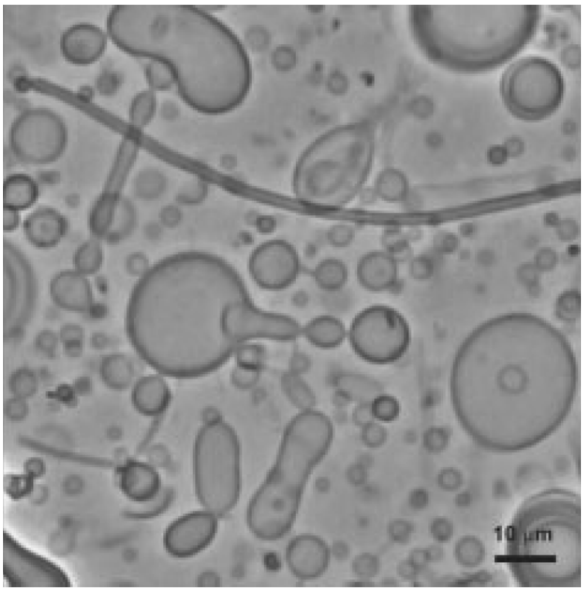

Figure 2.14: Shapes of self-assembled vesicles: spherical, biconcave, toroidal, pear-shaped et cetera [52], reproduced by courtesy of M. Antonietti.

the membrane's shape. To describe the shapes of vesicles at the mesoscopic level, we need to introduce a formalism. Since the thickness of the membrane D is much smaller than the characteristic length scale L in the other two dimensions, we can describe the membrane as a two-dimensional regular surface. Moreover, we assume that the orientations of the molecules described by the unit normal vector associated with every point of the surface and playing the role of the order parameter (see Fig. 2.15).

Since fluid membranes have no internal structure, the molecules can easily diffuse in-plane with no energy cost. However, out-of-plane fluctuations corresponding to a change of shape cost energy because they introduce "frustration" (here 'deviation from perfection') in orientation of the normals (molecules). The deviation from the flat layer and associated energy cost is locally proportional to the gradient of the normals or curvature. In general, the curvature (H, K or κ_1, κ_2) is a good local variable to describe the shape of the membrane, and being small compared to the inverse molecular size $\kappa_{1,2} \ll 1/D$, it can serve as an order parameter for the Landau–Ginsburg free energy. This free energy must be a rotationally-invariant scalar, and therefore it should contain only invariant terms, which are H, H^2, K and their combinations, that do not depend on the system of coordinates. The phenomenological Landau theory assumes that, in the vicinity of a second order phase transition, the free energy can be written as an expansion in the order parameter, including only symmetry allowed terms. Let us consider the symmetric membrane shown in Fig. 2.16, where both sides are identical and thus $\mathbf{n} \leftrightarrow -\mathbf{n}$. Since the mean curvature H depends on the sign of $\mathbf{n}$ and the Gaussian curvature K does not (see Eq. (2.15)), the surface energy for symmetric membrane is, therefore, restricted to the even powers of H and we can write

$$\mathscr{F} = \mathscr{F}_0 + \iint dS\{ \underbrace{a_1 H^2 + a_2 K}_{\text{second order}} + \underbrace{a_3 H^4 + a_4 H^2 K + a_5 K^2}_{\text{fourth order}} + \ldots\}. \tag{2.41}$$

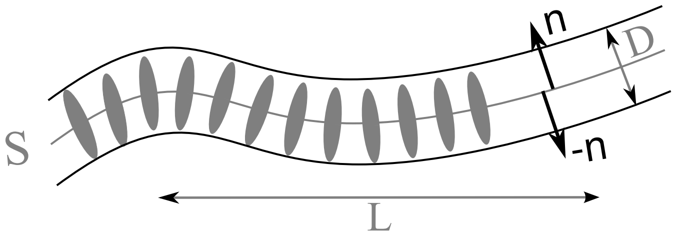

Figure 2.15: Fluctuating membrane with molecules aligned along the normal $\mathbf{n}$ of the surface S. The characteristic length scale L, and the thickness of the membrane $D \ll L$.

This expression, where the first term corresponds to the *bending* energy, gives the deviation of the energy of the curved membrane from the one of a flat layer $H = K = 0$. To guarantee the stability of the flat layer we require the quadratic form given as $f(\kappa_1, \kappa_2) = \frac{1}{4}a_1(\kappa_1 + \kappa_2)^2 + a_2\kappa_1\kappa_2$ to be positive definite, implying that $f_{\kappa_1\kappa_1} f_{\kappa_2\kappa_2} - f^2_{\kappa_1\kappa_2} > 0$ and $f_{\kappa_1\kappa_1} > 0$. These inequalities are satisfied if $-a_1 < a_2 < 0 < a_1$, otherwise higher order terms should be taken into account to stabilize the system. The elastic coefficients a_i can be derived from microscopic models, where they describe the averaged interactions between self-assembled molecules and with the solvent. Here, we discuss only the Helfrich model [53], that is a harmonic approximation of Eq. (2.41) with $a_1 > 0$, and the model of spontaneous bending [54], where a_1 is supposed to be small and negative, and thus higher order terms are necessary.

Similar to soap films, the equilibrium shape of vesicles can be found by solving the following variational problem:

$$\delta\mathscr{F} = \delta \iint dS\,\Phi(H, K) = 0, \tag{2.42}$$

where $\Phi(H, K) = a_1 H^2 + a_2 K + \ldots$ is the free energy density. By varying the surface we can find the general shape equation corresponding to $\delta\mathscr{F} = 0$ and given by [55]

$$\left(2H^2 - K + \frac{1}{2}\nabla^2\right)\Phi_H + (2HK + \bar{\nabla}^2)\Phi_K - 2H\Phi = 0, \tag{2.43}$$

where $\Phi_H = \partial\Phi/\partial H$, $\Phi_K = \partial\Phi/\partial K$, $\nabla^2 = (1/\sqrt{g})\partial_i(g^{ij}\sqrt{g}\partial_j)$, $\bar{\nabla}^2 = (1/\sqrt{g})\partial_i(KL^{ij}\sqrt{g}\partial_j)$. Here $g_{ij} = \begin{pmatrix} E & F \\ F & G \end{pmatrix}$ and $L_{ij} = \begin{pmatrix} e & f \\ f & g \end{pmatrix}$ are associated with first and second fundamental forms. The vanishing of the first variation means that the energy of a vesicle has an extreme value, which however does not guarantee that it is minimum. For the stability of vesicles we also need to require that the second variation $\delta^{(2)}\mathscr{F}$ is positive definite.

2.4.1 Helfrich model

The well known model, established by Helfrich [53] more than 30 years ago, suggests that the free energy of a fluid membrane is governed by the following terms

$$\mathscr{F}_H = \iint dS\{2k(H - H_0)^2 + \bar{k}K\}, \tag{2.44}$$

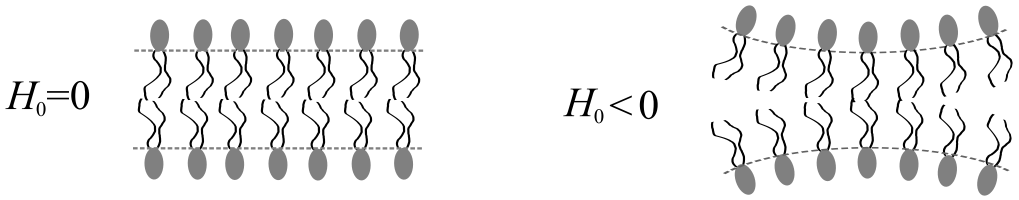

Figure 2.16: Curvature frustration for symmetric bilayer, consisting of two monolayers [41]. The difference in the cross-section between the hydrophilic heads and the hydrophobic chains results in the bending of monolayers.

where H_0 is called the *spontaneous curvature* of the membrane, k is the *bending rigidity* and $\bar{k}$ is known as the *saddle-splay modulus*. The first term describes the energy cost of the deviation from the local value of spontaneous curvature and vanishes when $H = H_0$ for all points of the surface. The second term is a topological invariant, namely it does not vary if no topological transformations are involved, and therefore is usually omitted. We are left only with the bending term, which corresponds to the harmonic approximation of the Landau expansion (Eq. (2.41)) around $H = H_0$, where $H_0 \neq 0$ accounts for the non-symmetric properties of membranes, e.g. the difference in the number of molecules in each layer (see Fig. 2.16). Although being introduced phenomenologically, the value of H_0 describes the tendency of different parts of the bilayer to bend towards either water ($H_0 < 0$ by convention) or the oil ($H_0 > 0$) [56]. The interfaces bend because of the mismatch between the head-head and tail-tail interactions. The parameters, H_0, k and $\bar{k}$, entering the Helfrich free energy can be derived via the microscopic model proposed e.g. in [56, 40] or from the Frank elastic constants of liquid crystals (see Annotation 2.3). The bending rigidity κ is found to be positive and of the order of 10^{-19} J, which is tenth of $k_B T$, whereas not much experimental data is available on the saddle-splay modulus $\bar{k}$. In [57] the value of $\bar{k}$ is found to be negative and of the order of $\bar{k} \simeq -0.83k$, which satisfies the condition of stability $-2k < \bar{k} < 0$ (see page 37), whereas in equilibrium between cylinders, spheres and discs it was measured as $\bar{k} \approx 2k_B T$ [58]. Thermal fluctuations can be taken into account via the renormalization of the bending rigidity and saddle-splay modulus at large scales given by [59]

$$k(\Lambda'^{-1}) = k(\Lambda^{-1}) - \frac{3k_B T}{4\pi} \log \frac{\Lambda}{\Lambda'}, \tag{2.45}$$

$$\bar{k}(\Lambda'^{-1}) = \bar{k}(\Lambda^{-1}) + \frac{5k_B T}{6\pi} \log \frac{\Lambda}{\Lambda'}, \tag{2.46}$$

where Λ^{-1} represents a microscopic length scale and $\Lambda' < \Lambda$. One may say that short distance fluctuations soften the bending rigidity on large scales.

The Helfrich model was successful in explaining and predicting different shapes of vesicles. Substituting the Helfrich functional $\Phi(H,K) = 2k(H - H_0)^2 + \bar{k}K$ into Eq. (2.43), we find the equation for stationary shapes as

$$4k(H - H_0)(H^2 - K + HH_0) + 2k\nabla^2 H = 0. \tag{2.47}$$

Besides cylinders and spheres, the analytic solutions of Eq. (2.47) can be the torus, the biconcave shape of red blood cells for $H_0 > 0$, and Delaunay surfaces [55].

Annotation 2.3 Frank free energy for liquid crystals

The crucial step forward in the theoretical description of fluid membranes was in realizing that they are in the liquid crystal state. Nematic liquid crystals have long-range orientational order, which can be described by the distribution of director $\mathbf{n}$ (order parameter). In equilibrium, the distribution is homogeneous, i.e. $\mathbf{n} = \text{const}$, whereas a non-homogeneous distribution of $\mathbf{n}$ describes the deformed nematic liquid crystals with *splay, twist* and *bend* distortions shown in Fig. 2.17. The elastic free energy of distorted nematic liquid crystals also known as Frank free energy (Frank, 1958) can be written as

$$\mathscr{F}_{\text{Frank}} = \frac{1}{2}\iiint d^3x\,\{K_{11}(\nabla\mathbf{n})^2 + K_{22}[\mathbf{n}\cdot(\nabla\times\mathbf{n})]^2 + K_{33}[\mathbf{n}\times(\nabla\times\mathbf{n})]^2 + \\ + 2K_{24}\nabla\cdot[(\mathbf{n}\cdot\nabla)\mathbf{n} - (\nabla\cdot\mathbf{n})\mathbf{n}]\}, \quad (2.48)$$

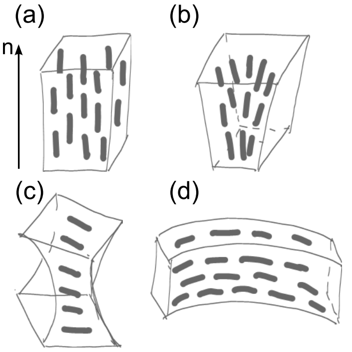

Figure 2.17: (a) Non-deformed liquid crystal with $\mathbf{n} = \text{const}$; (b) splay, (c) twist, (d) bend deformations.

where the elastic constants K_{11}, K_{22}, K_{33} describe splay, twist and bend deformations respectively. The K_{24} term can be viewed as tangential director gradient, but it is of the second order of smallness and therefore is often neglected. For a uniquely defined surface the rotation of $\mathbf{n}$ must vanish. Then, taking into account Eq. (2.15), we can rewrite Eq. (2.48) for membranes as

$$\mathscr{F} = \iint d^2x\,\{2K_{11}DH^2 - 2K_{24}DK\}, \quad (2.49)$$

which has the same form as Eq. (2.44) for $H_0 = 0$ with coefficients $k = K_{11}D$ and $\bar{k} = -2K_{24}D$ expressed via Frank's elastic constants. By multiplying the typical value of $K_{11} \sim 10^{-11}$ N by the membrane thickness $D \sim 10^{-8}$ m, we get $k \sim 10^{-19}$ J [60].

Annotation 2.4 Historical note

In mathematics, the functional $W = \iint dS\,H^2$ is called the Willmore energy. Willmore found that a sphere achieves the absolute minimum value of 4π among all compact surfaces. Willmore implicitly proposed the global problem of finding compact surfaces of a given topology minimizing W [61]. I do not know if Helfrich was aware of the works of Willmore, but certainly he knew very well the Frank's energy of liquid crystals, which is analogous to Eq. (2.44) (see Annotation 2.3 and reference [62]). But it was even before Willmore and Frank, about 1810, when Sophie Germain [61] and S. D. Poisson [55] were considering independently $\iint dS\,H^2$ as the term to describe the elastic energy of surfaces or thin shells.

However, the Helfrich model for symmetric membranes ($H_0 = 0$) does not address the question of how vesicles could be formed from flat membranes, but rather focuses on the consequences, like equilibrium shape, assuming that vesicles with curvature H_0 are already formed. In this context, the mechanism of vesicle formation is often associated with edge effects [52]. If the membrane looses a lot of energy at the edges, because of the hydrophobic interactions with the solvent, it curves to decrease the free boundary to the expense of elastic energy and finally closes and forms the vesicle. In such scenario, the free energy contains two competing terms, one being the bending energy and the other one the line tension

$$\mathscr{F} = \iint dS\{2kH^2 + \bar{k}K\} + \gamma \oint_{\partial S} dl. \tag{2.50}$$

Assuming that during the transformation from membrane to vesicle the surface area does not change (the number of molecules is constant), one can estimate the resulting equilibrium size of spherical vesicle as $R \approx (2k + \bar{k})/\gamma$.

2.4.2 Spontaneous bending model

Recently, an alternative mechanism of vesicle formation, that applies to *symmetric* membrane, was proposed [54]. It suggests that the driving force for vesicle formation is due to the spontaneous bending, resulting from the frustration between core–core and tail–solvent microscopic interactions. The entropic contribution from the tail–solvent system, could become a dominant one for long tails, resulting in a negative coefficient in front of H^2 or spontaneous bending. To stabilize the free energy higher order, symmetry allowed[3], terms are needed

$$\mathscr{F}_{\text{spb}} = \iint dS\{-|A|H^2 + A'K + c_1H^4 + c_2H^2K + c_3K^2\}. \tag{2.51}$$

The coefficients c_i can be derived from microscopic models, that take into account the interactions of molecules with the solvent, which is likely to play an important role for the process of self-assembly. In the next chapter we consider an experimental system which allows to extract the values of c_i from experimental data and moreover to compare two models Eqs. (2.50), (2.51). Note, the presence of higher order terms takes into account the dependence of the free energy on the size of self-assembled structure. Since, for symmetric membranes linear terms in H are symmetry forbidden the Helfrich free energy reduces to $\iint dS\, H^2$, that does not depend on the size of vesicles.

We believe that the new form of the free energy (Eq. (2.51)) could clarify some nontrivial equilibrium shapes, experimentally observed, but not explained within the Helfrich model. Although, solving the equilibrium shape equation (Eq. (2.43)) resulting in

$$\begin{aligned} &2AH(H^2 - K) + 4(c_2 - c_1)H^3K + 2(c_3 - c_2)HK^2 + 6c_1H^5 + \\ &\qquad + \nabla^2(AH + 2c_1H^3 + c_2HK) + \bar{\nabla}^2(c_2H^2 + 2c_3K) = 0 \end{aligned} \tag{2.52}$$

is hopeless analytically, one can use numerical approaches to minimize the free energy directly. The open source package of Ken Brakke called "Surface Evolver", being modified by Jamil Hetzel to take into account higher order terms, allows to find locally stable shapes of vesicles. The variation of the free energy Eq. (2.51) around a sphere is considered in the Appendix B.

---

[3] As we mentioned before, the terms such as HK and H^3 are not allowed for symmetric membranes.

3

Deformation of vesicles in high magnetic fields

Contents

High magnetic fields were used to deform spherical vesicles, self-assembled from bola-amphiphilic sexithiophene molecules. At low fields the deformation – measured through linear birefringence – scales quadratically with the vesicle radius and with the magnetic field strength. These data confirm a long standing theoretical prediction (W. Helfrich, Phys. Lett. **43A***, 409 (1973)), and permits the determination of the bending rigidity of the vesicles as (2.6±0.8)×*10^{-21} *J. At high fields, an enhanced rigidity is found which cannot be explained within the Helfrich model. We propose a complete form of the free energy functional that accounts for this behaviour, and allows discussion of the formation and stability of vesicles in solution.*

3.1 Why do we need high magnetic fields?

There are several advantages of using magnetic fields instead of electric fields to study the complex behaviour of materials:

1. magnetic fields change the system state, by exerting the torque on molecules;
2. magnetic fields are applied in contact-free manner;
3. magnetic forces are well controlled, since they are homogeneous in the whole volume.

The studied materials can be of *ferromagnetic, paramagnetic,* or *diamagnetic* nature. Most organic, inorganic, and polymeric compounds, such as water, wood, living organisms, are diamagnetic or "non-magnetic" materials. Since the diamagnetic response is very weak compared to the ferromagnetic one, it can be studied only with the help of high magnetic fields (>10 Tesla, where 1 Tesla = 10^4 Gauss).

The origin of diamagnetism is in the induced motion of electrons under the applied magnetic field **B**, causing the magnetic moments to align in a direction opposite to that of the applied magnetic field. The induced magnetization **M**, defined as magnetic moment per unit volume, is proportional to the magnetic field

$$\mathbf{M} = \chi\mathbf{B}, \tag{3.1}$$

where χ is the magnetic susceptibility, which is dimensionless and *negative* for diamagnets. Superconductors are perfect diamagnets with $\chi = -1$, expelling all the magnetic field from the material and thus cancelling the flux (Meissner effect). Although superconductors exhibit a strong effect, diamagnetism in general is quite a weak effect with typical value of χ of the order of -10^{-6}.

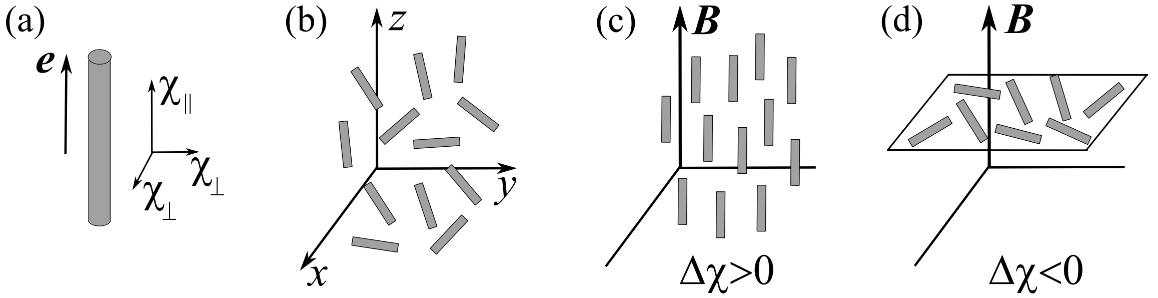

Figure 3.1: (a) Anisotropic molecule with anisotropic magnetic susceptibility $\chi_{\parallel} \neq \chi_{\perp}$; (b) isotropic random state. Alignment in magnetic field of molecules: (c) with $\Delta\chi > 0$ along the field; (d) with $\Delta\chi < 0$ in plane perpendicular to the field.

In case of anisotropic material, the susceptibility χ is a tensor, such as $M_\alpha = \chi_{\alpha\beta}B_\beta$. For uniaxial materials, such as nematic liquid crystal, $\chi_{\alpha\beta} = \begin{pmatrix} \chi_\perp & 0 & 0 \\ 0 & \chi_\perp & 0 \\ 0 & 0 & \chi_\parallel \end{pmatrix}$ and thus

$$\mathbf{M} = \chi_\perp \mathbf{B} + (\chi_\parallel - \chi_\perp)(\mathbf{B}\cdot\mathbf{e})\cdot\mathbf{e}, \tag{3.2}$$

where **e** is the unit vector along the axis of the material. The interaction of **M** with a magnetic field results in magnetic energy

$$E_{\mathrm{mag}} = -\frac{1}{2}\chi_\perp V B^2 - \frac{1}{2}\Delta\chi V(\mathbf{e}\cdot\mathbf{B})^2, \qquad \Delta\chi = \chi_\parallel - \chi_\perp, \tag{3.3}$$

where the first term does not depend on molecular orientation and may be omitted. The second term depends on the orientation **e** and is the source of magnetic alignment. If $\Delta\chi > 0$, then this term is minimized when the alignment axis **e** of the molecule is parallel to the magnetic field **B**. For example, the C–C bond in organic molecules has $\chi_\parallel < \chi_\perp < 0$ and thus $\Delta\chi < 0$, resulting in the alignment of the bond in the direction perpendicular to the field. In Fig. 3.1 we show schematically the alignment of anisotropic molecules in presence of **B** [34]. Magnetic alignment occurs when the second term in E_{mag} exceeds thermal energy, yielding the condition $\Delta\chi V B^2 > k_B T$. In case of a single molecule with $\Delta\chi \sim 10^{-7}$ and $V \sim (10\ \mathrm{nm})^3$ we get $B > 10^5$ T, that is not achievable in practice[1]. Therefore single molecules cannot be aligned by magnetic fields, because of thermal motion. However self-assemblies of N molecules with $N > 10^5$ behaving as a whole can be potentially aligned with magnetic fields since now we have $N\Delta\chi V B^2 > k_B T$ [63].

Three decades ago Helfrich suggested that magnetic forces could be used to deform spherical vesicles self-assembled from diamagnetic molecules [62]. But only recently, such magnetic deformations were observed experimentally at the High Field Magnet Laboratory of our university [64]. In the following we present experimental data and two theoretical approaches, which allow to extract information about the elastic properties of vesicles (see Appendix A and paper [65] for details).

---

[1] The highest permanent magnetic field generated in High Fields Magnet Laboratories is 45 T, exceeding million times the magnetic field of the Earth. The available pulsed magnetic fields reach the value of about 100 T.

3.2 Experimental observations of 6T vesicles

Experimentally we investigate sexithiophene (6T) (Fig. 3.2a) which is a π-conjugated oligomer with a rigid apolar sexithiophene block substituted at both ends by polar ethylene oxide chains. 6T forms hollow spherical self-assemblies in a 2-propanol solution (Fig. 3.2b, details can be found in [64]). Dynamic light scattering (DLS) reveals a narrow distribution of vesicle sizes, with an average radius $R(T)$ (±10%) that increases with temperature T from 56 nm at 20 °C to 126 nm at 60 °C (Table 3.1). At 70 °C the spherical shape is lost, while at 80°C the scattering intensity is zero because the 6T molecules are molecularly dissolved [64].

6T molecules have a strongly anisotropic diamagnetic susceptibility $\Delta\chi = 8.1 \cdot 10^{-6}$ [66], which means that the sexithiophene core tends to orient along the field [67]. Consequently, vesicles are deformed from a sphere to an oblate ellipsoid, where more molecules are parallel (top and bottom of the vesicle) than perpendicular to the field (around the equator, Fig. 3.2c), reducing the magnetic energy at the expense of elastic energy. This magnetic deformation is probed by measuring the field induced optical birefringence Δn in a resistive 20 T magnet at different T. Birefringence is defined as the difference of refractive indices parallel and perpendicular to the magnetic field, namely $\Delta n = n_\parallel - n_\perp$. For symmetric spheres $\Delta n = 0$, whereas for asymmetric discs, when all molecules are aligned along the field, birefringence reaches its maximum value.

Annotation 3.1 Cylindrical 6T assemblies in butanol

Recently, new experiments in HFML demonstrated that 6T molecules form a cylindrically shaped structures in butanol [68]. The authors claim that the morphology of 6T aggregates, ranging from spherical structure, needles, and rodlike helical assemblies, can be tuned by using different solvents, which offers a promising approach for constructing nanostructures with desired functionalities [68].

3.3 Deformation versus birefringence

For small deformations (low fields) the normalized birefringence $\Delta n/\Delta n_{\max}$ ($\Delta n_{\max} = -6.5 \cdot 10^{-5}$ [69] calculated from anisotropic polarizability) scales linearly with deformation [62, 70], but a more accurate relation is needed for high deformations (high fields). For small vesicle concentrations ρ_c the refractive index n is related to the polarizability of individual vesicles α by $n^2 = n_0^2 + 4\pi\rho_c\alpha$, where n_0 is the refractive index of the solvent. The dipole moment of the 6T molecules $\mathbf{p}$ is connected with the effective electric field $\mathbf{E}'$ in the molecular layer by $\mathbf{p} = \alpha_\perp\left(\mathbf{E}' - \mathbf{e}\left(\mathbf{e}\mathbf{E}'\right)\right) + \alpha_\parallel \mathbf{e}\left(\mathbf{e}\mathbf{E}'\right)$, where $\alpha_\perp$ and $\alpha_\parallel$ are the polarizabilities of 6T molecules with respect to $\mathbf{e}$, the unit vector normal to the vesicle at a given point of its surface. Applying standard boundary conditions on the Maxwell equations we find the birefringence of a uniaxially deformed vesicle:

$$\Delta n = \pi\rho_c\rho_m\left(\alpha_\parallel\frac{\epsilon_0}{\epsilon_n} - \alpha_\perp\right)\iint dS\left(1 - 3e_z^2\right), \tag{3.4}$$

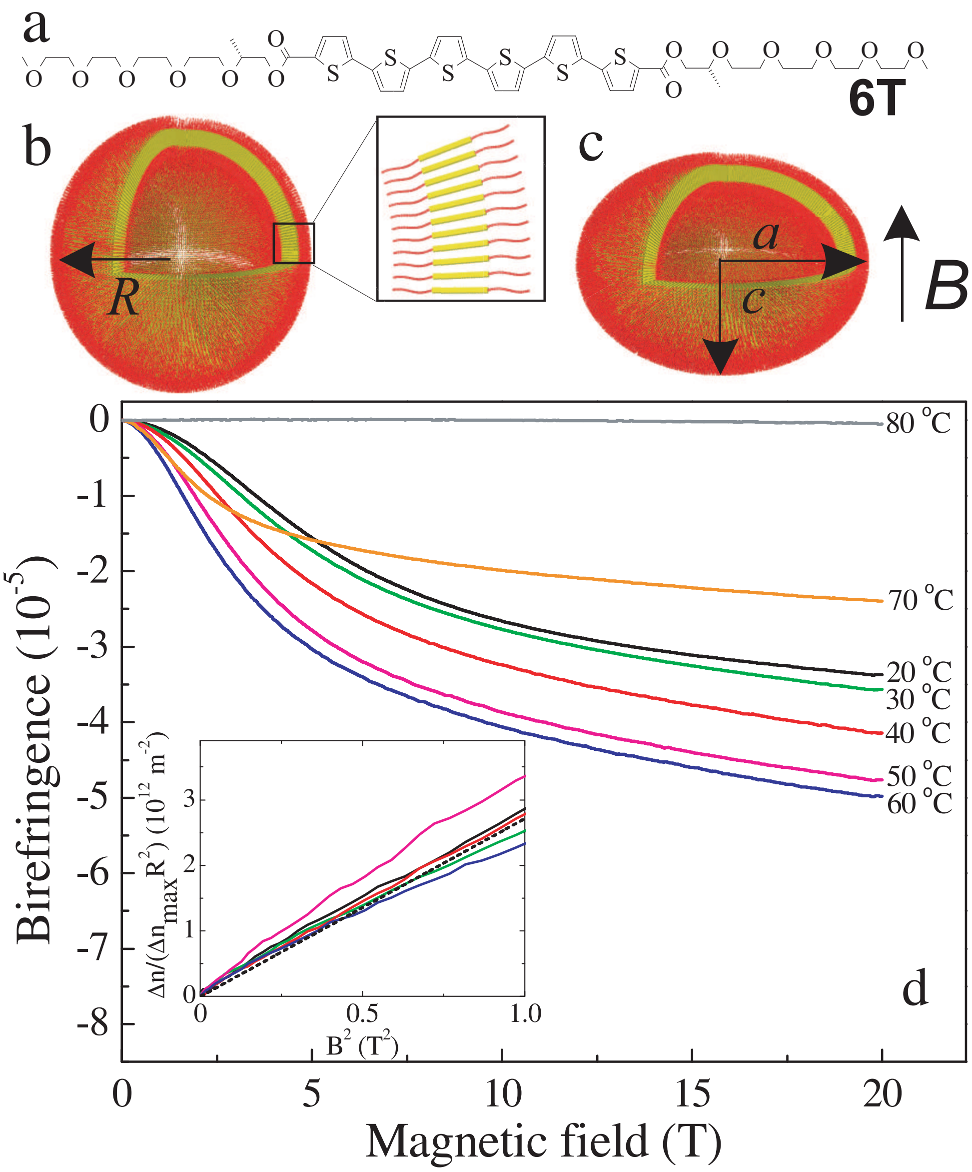

Figure 3.2: a) Chemical structure of a sexithiophene molecule (6T). Schematic representation of a spherical vesicle with radius R (b) and magnetically deformed vesicle with semi-axes a and c (c) d) Temperature dependence of the magnetic field (B) induced birefringence of a 1 g/l 6T solution in 2-propanol. Inset: normalized birefringence Eq.(3.6) divided by R^2 and plotted versus B^2. The dashed line corresponds to a fit with constant bending rigidity $k = 0.64 \cdot 10^{-21}$ J.

where ϵ_0 and ϵ_n are the dielectric constants of the solvent and of the 6T in the direction along $\mathbf{e}$, respectively, ρ_m is the surface density of molecules in the layer, the integration is over the surface S of the vesicle and z labels the direction of magnetic field $\mathbf{B}$.

To calculate Δn we assume that the shape of the deformed vesicles can be described by superspheroid[2], that is a surface of revolution with the following parametrization

$$\begin{aligned} x(u,v) &= a\cdot\sin^l v\cos u, \\ y(u,v) &= a\cdot\sin^l v\sin u, \\ z(u,v) &= c\cdot\cos^l v, \qquad (a > c), \end{aligned} \tag{3.5}$$

where a is the radius of the circular cross-section in the xy plane and c is the semi-axis in the z direction (Fig. 3.2c). Superspheroids with exponent $l < 1$ allow vesicle to flatten and obviously they represent a more general class of shapes than the spheroids ($l = 1$) that are commonly used for small deformations [62]. The birefringence now reads:

$$\frac{\Delta n}{\Delta n_{\max}} = -\frac{1}{2\pi a^2}\iint dS\,(1-3e_z^2), \tag{3.6}$$

where $\Delta n_{\max}$ is achieved in the limit of $c \to 0$ (all the molecules are completely aligned along the field). Figure 3.3 shows $\Delta n/\Delta n_{\max}$ as function of deformation $(a-c)/R$ for (super)spheroids. We keep the surface area of the vesicle constant, assuming a constant number of 6T molecules that form a permeable membrane. Remarkably, both curves are rather similar, in particular in the low deformation limit, where we recover the linear relationship between Δn and deformation

$$\frac{\Delta n}{\Delta n_{\max}} \simeq \frac{a-c}{R}, \tag{3.7}$$

by expanding Eq. (3.6) (see Appendix A). This result was known from [62, 70], however we find that it holds as long as $(a-c)/R \leqslant 0.3$ (Fig. 3.3).

3.4 Fit of experimental data

We fit experimental data within a framework of two models of vesicle formation discussed in section 2.4. For symmetric bola-amphiphiles, like 6T molecule is, the elastic free energy is restricted to the even powers of curvature, and we use this fact for phenomenological description. As already said, this approach can be used because the vesicle size is large compared to the intermolecular distances, which means that the vesicle shape is characterized by its curvatures. We assume the superspheroidal shape of vesicles for all studied temperatures and the whole range of magnetic fields. We determine the equilibrium values of a, c and l at each B by *minimizing* the total free energy $\mathscr{F}_{\text{tot}}$,

---

[1] Superllipse shapes, which are neither round nor rectangular, are widely used in architecture and design. For example, Sergels Torg in Stokholm, is in fact superellipse with $l = 0.8$ and $a/c = 6/5$, which was proposed by Danish scientist Piet Hein [71].

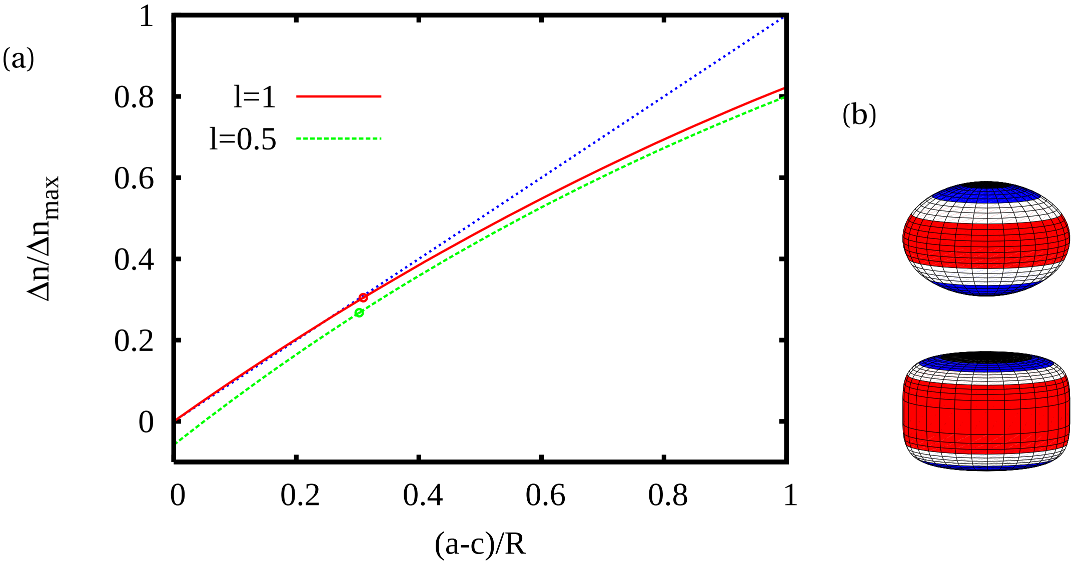

Figure 3.3: (a) Calculated relation between birefringence and deformation for spheroid (solid line) and for superspheroid with $l = 0.5$ (dashed line) keeping surface constant $S = 4\pi R^2$. The linear relation $\Delta n/\Delta n_{\max} \simeq (a-c)/R$ predicted by [62, 70] is shown by dotted line. (b) The shapes corresponding to the marked dots on the left plot with $(a-c)/R \simeq 0.3$: spheroid with $l = 1$ (top) and superspheroid with $l = 0.5$ (bottom).

which is the sum of the elastic $\mathscr{F}_{\mathrm{el}}$ and magnetic $\mathscr{F}_{\mathrm{mag}}$ free energy. Simultaneously, the parameters in $\mathscr{F}_{\mathrm{el}}$ are determined by a fit to the experimental Δn using relation (3.6). Moreover, in all our calculations we keep the surface area of the vesicle constant, assuming constant density of the molecules.

3.4.1 Helfrich model (fit up to 3 T)

We first consider the well known form of the elastic free energy proposed by Helfrich [53], leading to

$$\mathscr{F}_{\mathrm{tot}} = \mathscr{F}_{\mathrm{el}} + \mathscr{F}_{\mathrm{mag}} = 2k \iint dS\, H^2 - \frac{\Delta\chi D B^2}{2\mu_0} \iint dS\, e_z^2, \tag{3.8}$$

where H is the mean curvature and $D = 6.4$ nm (length of long axis of 6T) is the thickness of the membrane. Note that for symmetric 6T vesicles $\mathscr{F}_{\mathrm{el}}$ is the same as Eq. (2.44) with $H_0 = 0$. The bending rigidity k is the only fit parameter to obtain the best description of the experimental birefringence. The Helfrich model describes experimental curves only at low fields (small deformations) up to 3 T as shown in Fig. 3.4.

For small deformations we can expand Eq.(3.8) and write the condition of equilibrium (for derivation see Appendix A, Eq. (A.42)) as

$$\frac{a-c}{R} = B^2 \frac{R^2 D \Delta\chi}{12 k \mu_0}. \tag{3.9}$$

By combining Eqs. (3.7) and (3.9) we find that the low field birefringence is inversely proportional to the bending rigidity k, and scales quadratically with magnetic field and

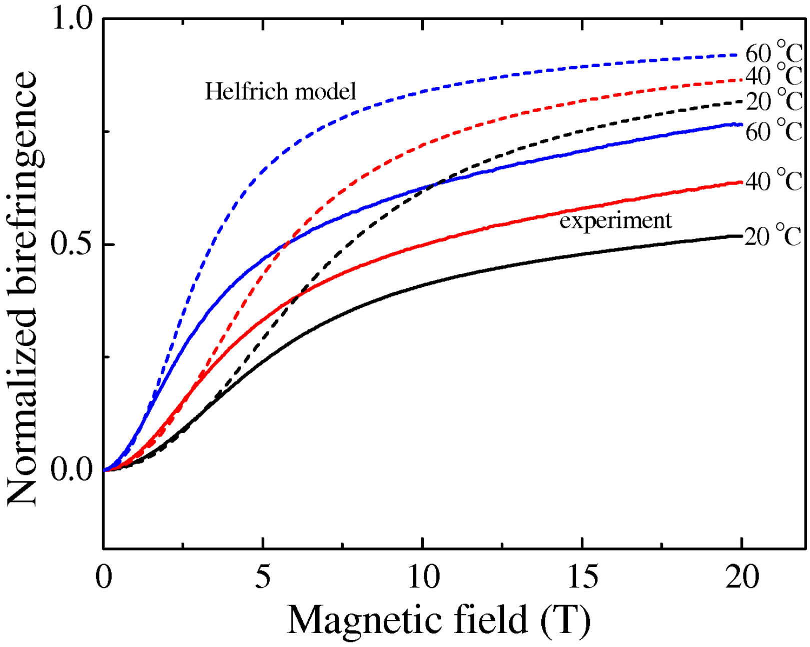

Figure 3.4: Normalized birefringence of magnetically deformed 6T vesicles. Solid lines: experimental data for different temperatures. Dashed lines: calculated birefringence in the Helfrich model, fitting the low-field behaviour using a constant k for all T.

vesicle radius (the Helfrich result). The experimental results (inset of Fig.3.2) indeed exhibit this scaling up to $B \sim 1$ T, allowing to determine k as $(0.64\pm0.2)\times10^{-21}$ J, independent of temperature. This confirms the long-standing theoretical prediction (about the scaling of k) and allows to determine experimentally the bending rigidity for this type of vesicles.

3.4.2 Spontaneous bending model (nontrivial fit)

The Helfrich free energy thus quantitatively describes the birefringence data in the low deformation regime using a constant bending rigidity. However, this model clearly overestimates the experimental birefringence at high fields (Fig. 3.4), which indicates an increased bending rigidity at higher deformations. Therefore we extend the expression of the free energy by including all symmetry allowed terms up to fourth order [54]:

$$\mathcal{F}_{\mathrm{el}} = \iint dS\{A'K + AH^2 + c_1 H^4 + c_2 H^2 K + c_3 K^2\}, \tag{3.10}$$

where K is the Gaussian curvature. According to the spontaneous bending model (section 2.4), the elastic constant A can be small and even *negative* so that fourth order terms may be dominant. Since at $B = 0$ the vesicles are spherical, with $H^2 - K = 0$, it is convenient to rewrite $\mathcal{F}_{\mathrm{el}}$ as

$$\begin{aligned}\mathcal{F}_{\mathrm{el}} = \iint dS\big[(A+A')K + A(H^2-K) + (c_1+c_2+c_3)H^4 - \\ - (c_2+2c_3)H^2(H^2-K) + c_3(H^2-K)^2\big]. \end{aligned} \tag{3.11}$$

Table 3.1: Structural properties of 6T vesicles in 2-propanol at different temperatures. Vesicle radius R, as determined by dynamic light scattering (exp.) and obtained by fitting the magnetic birefringence (fit). Equilibrium parameters a, c and l of the deformed vesicles at 20 T.

Temperature	Radius R (nm)		Superspheroid(20 T)		
T (°C)	Exp.	Fit	a/R	c/R	l
20	56	58	1.19	0.59	0.90
30	68	62	1.20	0.56	0.89
40	75	75	1.23	0.50	0.88
50	88	99	1.26	0.42	0.85
60	126	110	1.28	0.39	0.84

Therefore for spheres only the first and the third terms do not vanish. If we compare the elastic energies Eq. (3.11) for a flat layer and for a set of spheres with radius R with the same total area, and neglecting the edge energy due to the interaction of the solvent with the hydrophobic cores, we find that $A + A' < 0$ and $c_1 + c_2 + c_3 > 0$ must hold to favour the formation of spheres. In this case, the minimum of Eq. (3.11) occurs for sheres of radius:

$$R^2 = \frac{1}{H^2} = -2\frac{c_1 + c_2 + c_3}{A + A'}. \tag{3.12}$$

Since the term $\iint dSA'K$ does not depend on deformation, the magnetic deformation data cannot provide directly information about A'. In fact, according to the Gauss-Bonnet theorem, $\iint dSK = 4\pi$ for any surface topologically equivalent to the sphere (like the superspheroid considered here). However, Eq. (3.12) can be used *a posteriori* to determine A', once the other parameters are found by a best fit to the experiments. This approach is very powerful, because it experimentally determines the total free energy of vesicles, which is very difficult to obtain otherwise, and which can be used to discuss the overall stability of vesicles.

Within this description the low field bending constant k can be calculated analytically for spheroids by expanding Eq. (3.10) for small deformations (this is a long calculation, see Appendix A for details)

$$2k = A(T) + \frac{14c_1 + 11c_2 + 8c_3}{3R^2(T)}, \tag{3.13}$$

which connects our approach to that of Helfrich. Moreover, since k has to be positive to guarantee stability against deformations, this equation poses an extra constraint on the choice of parameters. In the spirit of Landau theory, we assume that only A depends on T and that the coefficients c_i are temperature independent. In fact, by using the experimental value of k we eliminate the parameter A from the fitting procedure, by which c_i and $R(T)$ are determined via fitting to the experiments at different temperatures (see Fig. 3.5). For all temperatures the overall behavior of Δn is nicely reproduced, including the weaker field dependence at higher fields, indicating anharmonic deformation characterized by a field enhanced bending rigidity. The fitted value of $R(T)$ (Table 3.1) is well within the error margins of the experimental DLS values. Table 3.1 also shows the parameters a, c and l at 20 T, which correspond to substantially deformed vesicles, as illustrated

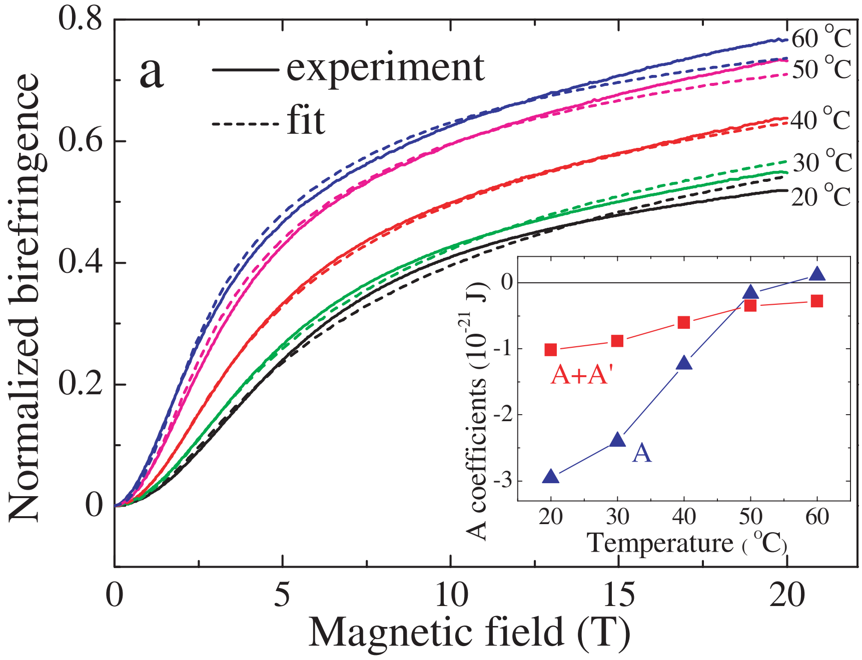

Figure 3.5: Fit (dashed lines) of the experimental birefringence (solid lines) at different temperatures, using superspheroidal vesicles with deformation energy $\mathscr{F}_{\mathrm{el}}$ given by equation (3.11). Inset: the temperature dependence of elastic constant $A(T)$ and $A'(T)$ calculated *a posteriori* by using Eqs. (3.13) and (3.12).

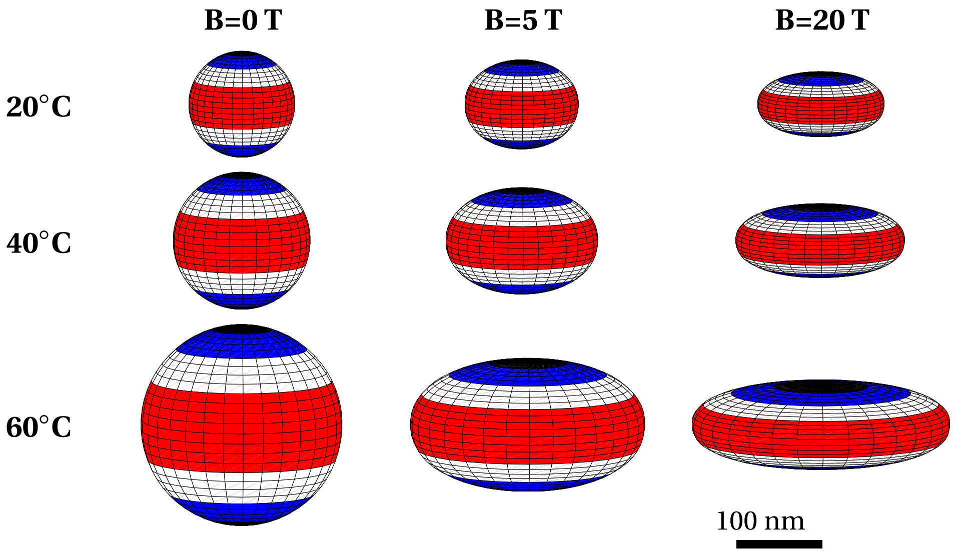

Figure 3.6: Illustration of calculated equilibrium shapes for different values of temperature and magnetic field

in Fig. 3.6. At the highest fields deformations $(a-c)/R$ as large as 0.9 are found, which agrees very well with the observed deformation of 6T vesicles that are fixed in a compatible organogel and imaged by scanning electron microscopy [64]. Not surprisingly, we find that with increasing deformation the vesicle shape becomes flatter (decreasing l, see Table 3.1), maximizing the number of molecules aligned along the field.

The best fits in Fig. 3.5 correspond to $c_1 = 1.148, c_2 = -1.336, c_3 = 0.358$ (10^{-35} Jm^2), and the T-dependence of A and $A + A'$ is shown in the inset. Indeed, these values make the vesicles stable at $B = 0$ ($A + A' < 0, c_1 + c_2 + c_3 > 0$) for $T < 60°C$. However, $A + A'$ approaches 0 when $T \rightarrow 60°C$, suggesting an instability of the vesicles at higher T, which is indeed compatible with the experiments that show that the vesicles melt above $60°C$. It is this vicinity of the system to an instability, which makes fourth order terms comparable in magnitude to second order ones and make the Helfrich model inadequate for this situation.

3.5 Conclusions

We found that a fourth order Landau–Ginzburg expression (spontaneous bending model) of the vesicle free energy describes quantitatively the measured elastic deformation up to high magnetic fields, far beyond the quadratic dependence predicted by Helfrich at low fields [62]. From the experimental data we obtain the free energy as a function of temperature that accounts for the overall stability of vesicles and predicts their dissolution at high temperature. The parameters c_1, c_2, c_3, $A(T)$ and $A'(T)$ fully describe the free energy of the vesicles. Their actual values are intricately related to the intermolecular interactions within the vesicle/solvent system, such as π-π interactions between neighboring 6T cores and interactions between 6T tails and solvent molecules [54, 72]. Determination of these parameters for a physical nanostructure therefore provides a stringent test case, on the basis of which microscopic intermolecular interaction models can be developed. Such a quantitative description of non-covalent interactions within molecular assemblies is an important step towards the detailed understanding of the rules of self-assembly.

Acknowledgements

It is my pleasure to thank Peter Christianen and Jan Kees Maan for sharing with me their knowledge and for many stimulating discussions. I am indebted to Igor Shklyarevskiy for doing experimental measurements reported here and to Jeroen Gielen for introducing me to the new experiments performed in HFML.

4

Double bubble: change of topology

Contents

We assumed in the previous chapter that the topology of vesicles does not change when they are deformed. However, in general, one cannot exclude the possibility of other topologies different from the spherical one. Here we propose a new candidate to the equilibrium shapes of vesicles, called double bubble, which has neither the topology of two spherical vesicles nor the one of a larger sphere. We study the relative stability of three shapes and present a phase diagram. We find that not only temperature, but also magnetic fields can induce topological transformations between spherical vesicles and double bubbles.

4.1 What is interesting about double bubbles?

When two soap bubbles of equal volume meet each other, they form a double bubble, a shape composed of two spherical caps separated by a flat disk (Fig. 4.1a). Surprisingly, only recently it has been proven that, among all surfaces, the double bubble has the least area to enclose and separate two given volumes [51]. The connected spherical bubbles often observed in soap are certainly a realization of this 'minimum property' of double bubbles since surface tension is the dominant driving force (see section 2.3). In this chapter we explore theoretically whether double bubbles could be an equilibrium shape of vesicles, when not only the surface tension, but also other energy terms, like elastic and magnetic energies, are relevant.

To the best of our knowledge, a double bubble was never considered as a candidate to describe the shape of vesicles. Firstly, the presence of the membrane S_2 (see Fig. 4.1a) distinguishes double bubbles from dumbbells or pear-shaped vesicles that were extensively studied [74, 75]. On the other hand, the surface S_2 consists of a *single* membrane which differs from the case of two adhering vesicles where the surface S_2 is composed of two interacting membranes forming a flat-contact doublet [76] (see Fig. 4.2a). Many theoretical studies was devoted to the fusion of membranes (two membranes merge into one) mediated by the formation of a stalk phase [77, 78, 79]. However, none of these studies considered the topology of the double bubble $\chi = 3$ (see Annotation 4.1 and Eq. (2.34)), which is neither the one of two spheres $\chi = 4$ nor the one of a single sphere $\chi = 2$ (see Fig. 4.2c). From a geometrical point of view one may therefore refer to a double bubble as an intermediate shape in the topological transformations between one and two spheres. Here we study theoretically the possibility of such topological transformation.

The basic reasoning for the formation of a *single* bilayer instead of two bilayers could be the capillary forces acting between two membranes (see Fig. 4.2b). In fact, if vesicles would favour the formation of multiple layers at the line of contact, than they would stick together forming a foam or more simple, their walls would be multilayered. Since this

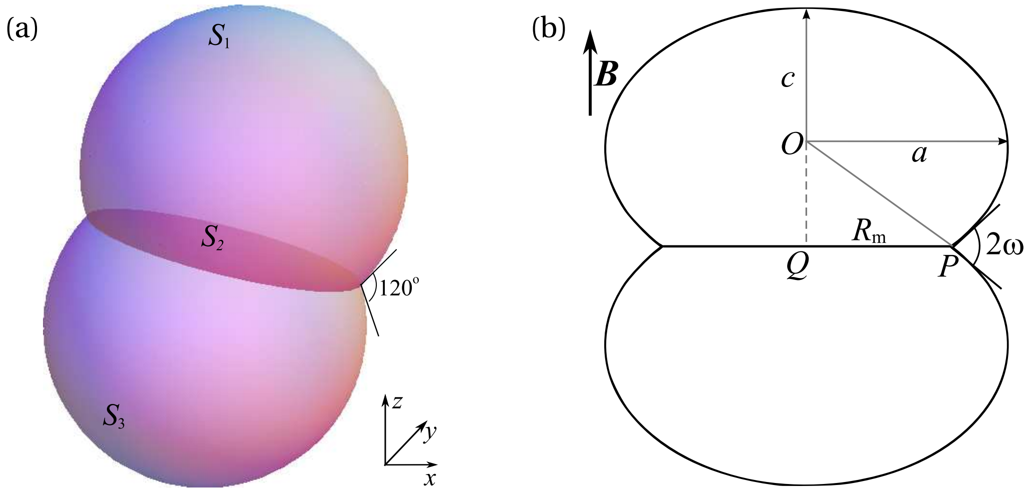

Figure 4.1: (a) The double bubble is the unique surface of least area that encloses two equal volumes; it is composed of two identical spherical caps S_1 and S_3 separated by a single membrane S_2 that is flat for equal volumes; the three pieces meet along a circle at 120° angle [73]. (b) Cross-section of a magnetically deformed double bubble with semi-axes $a > c$; 2ω is the angle between two tangent planes at the meeting circle, it is introduced as a parameter.

is not experimentally observed, we may expect the formation of a single layer at the line of contact. However, a single membrane results in the presence of an unavoidable kink, where the three surfaces meet together (as in the case of the double bubble). Such kinks in fluid membranes are not discontinuities in a strict mathematical sense, because of the finite thickness of the membrane and easy in plane diffusion of molecules (zero shear modulus and small surface tension). Therefore, the energy cost at the contact between three surfaces should be finite as we discuss below. The rigorous derivation of this energy term would require a detailed analysis of molecular interactions which is beyond the scope of this thesis. In Fig. 4.2b we show with red circles the regions in the vicinity of the kink, where understanding the molecular organisation requires further studies.

To study the instabilities of spherical vesicles towards double bubbles with a flat membrane we start from the well known model of elastic free energy proposed by Helfrich [53]. This model was successful in explaining some trivial shapes of red blood cells and in predicting some new non-trivial shapes of vesicles [40, 80, 60] (see chapter 2). However, one cannot apply without restrictions a continuum elastic theory to shapes with discontinuities, since it would yield infinite energy. The discontinuities can be taken into account by introducing a line tension with an effective angular dependence, as was proposed in [81]. Similar arguments can be applied to a double bubble, which has a circular rim with a singularity, where three smooth surfaces meet (see Fig. 4.1a). Therefore, to take into account the rim singularity in the shape of a double bubble, we propose a new phenomenological term derived from the Gauss–Bonnet theorem, and added to the Helfrich elastic free energy. Although other forms of the rim energy might be plausible, here we investigate the consequences of our ansatz. Assuming that intrinsic parameters of the system entering the phenomenological Helfrich free energy, like elastic moduli and spontaneous curvature, are temperature and pressure dependent [41], we

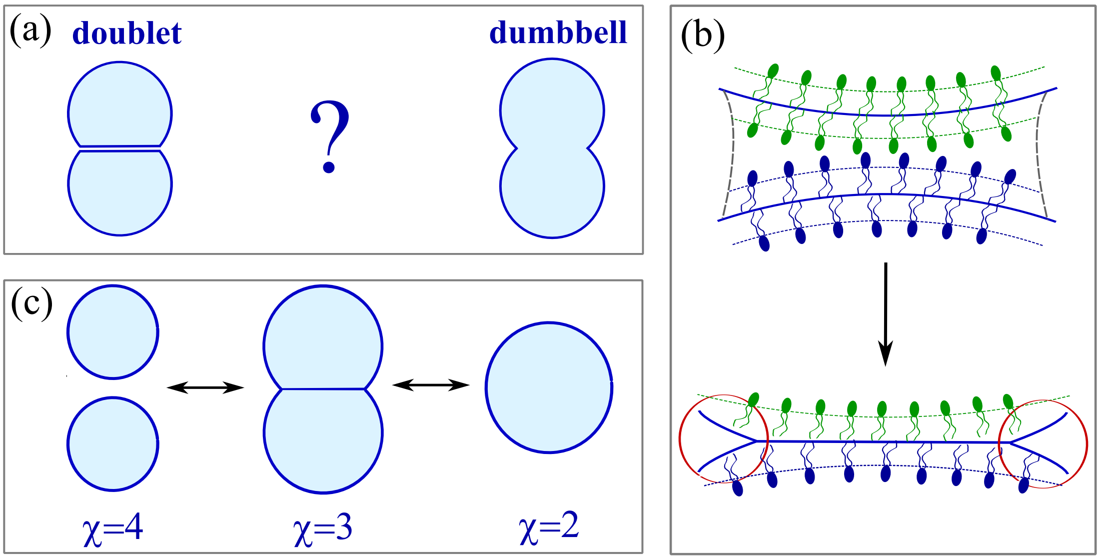

Figure 4.2: (a) The studied shapes of vesicles: two adhering vesicles, forming flat-contact doublet with $\chi = 4$ [76] and dumbbell with $\chi = 2$ [74, 75]. (b) The capillary forces (dashed lines) between two membranes could result in the formation of a single bilayer membrane, yielding a double bubble. Red circles show the regions were the molecular organization is not known. (c) Double bubble ($\chi = 3$) as an intermediate shape in topological transformations between one sphere ($\chi = 2$) and two spheres ($\chi = 4$).

propose a phase diagram for the studied shapes. It is intuitively clear that shapes similar to a double bubble may occur whenever flat membranes become favorable, for instance in presence of high magnetic fields that tend to orient diamagnetic molecules. For this case, experimental evidence of deformation of self-assembled spherical vesicles to oblate spheroid was reported in [64, 65]. Here, we find that a magnetic field can also influence the relative stability of shapes and can make two spheroidal vesicles less stable than a deformed double bubble or one larger spheroid. The latter transformation was experimentally observed for liposomes [82] in high magnetic fields.

4.2 Geometry and free energy

In Fig. 4.1a we show the double bubble as defined mathematically. The double bubble is composed of two spherical caps S_1 and S_3 separated by a disk S_2, meeting along a common circle (rim) at an angle of 120° [73]. To consider magnetic deformations, we study the modified geometry shown in Fig. 4.1b. Firstly, we assume that, during the deformation, the spherical caps S_1 and S_3 (with $S_1 = S_3$) change to oblate spheroids with semiaxes c and a parallel and perpendicular to the magnetic field B respectively (see Fig. 4.1b). Secondly, we allow the angle between the three surfaces to differ from 120° by introducing the parameter ω, related to the radius of the membrane as

$$R_{\mathrm{m}} = \frac{a^2 \sin\omega}{\sqrt{a^2 \sin^2\omega + c^2 \cos^2\omega}}, \qquad \text{(see Annotation 4.1).} \tag{4.1}$$

Here chapter we extend the concept of double bubble from the unique area minimizing surface with $c = a$ and $\omega = \pi/3$ to the set of shapes with $c \in (0, a]$, $\omega \in (0, \pi/2)$.

The equilibrium shapes of fluid membranes are usually studied in terms of the Helfrich model of bending energy (see chapter 2 and references there):

$$\mathscr{F}_{\mathrm{el}} = \int dS\{2k(H - H_0)^2 + \bar{k}K\}, \tag{4.2}$$

where H and K are the mean and Gaussian curvatures respectively, and H_0 is the spontaneous mean curvature. The first term, proportional to the bending rigidity k, describes the local deviation from equilibrium curvature H_0, while the second term with Gaussian rigidity $\bar{k}$ influences only the topology (Eq. (2.34)) and thus is often neglected. For the same reason, $\bar{k}$ is also not measurable if no topological transformations occur. Here we cannot omit this term, because we examine different topologies. It was shown theoretically and confirmed experimentally that $-1 < \bar{k}/k < 0$ for monolayer vesicles, while for bilayer vesicles $\bar{k}$ can be positive [41][1]. The values of H_0, k and $\bar{k}$ depend on pressure and temperature, and therefore may be considered as parameters and not as intrinsic properties of the system. We will consider the case with $0.7 < H_0 R_0 < 1.3$, $-1 \leqslant \bar{k}/k \leqslant 1$, where R_0 is the radius of the spherical vesicle, and $k = 4 \cdot 10^{-20} J \approx 10\ k_{\mathrm{B}}T$, the latter being a typical value for molecular vesicles. Moreover, we assume that self-assembled molecules keep a constant density, implying the condition of constant surface of the vesicles $S = 8\pi R_0^2$ as those of two spheres.

Annotation 4.1 Calculus for double bubble

The surface of spheroid is given by the following parametrization

$$\mathbf{x}(u, v) = \big(a \sin v \cos u,\ a \sin v \sin u,\ c \cos v\big), \qquad 0 \leqslant v \leqslant \pi, \quad 0 \leqslant u \leqslant 2\pi. \tag{4.3}$$

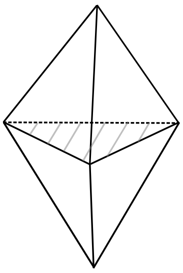

Figure 4.3:

Then from Eq. (4.3) and Fig. 4.1b follows that $OQ = |-c \cos v_P|$, $|OP|^2 = a^2 \sin^2 v_P + c^2 \cos^2 v_p$, resulting in

$$R_{\mathrm{m}} = QP = \sqrt{|OP|^2 - |OQ|^2} = a \sin v_P.$$

At point P we can express the tangent to ellipse as

$$\tan\omega = \frac{dz}{dy} = -\frac{c}{a} \tan v_P. \tag{4.4}$$

Substituting $\sin v_p = \tan v_p / \sqrt{1 + \tan^2 v_p}$ we find R_{m} (Eq. (4.1)). The Euler characteristic χ of a polyhedron is defined according to Eq. (2.32). Since the double bubble is homeomorphic to two tetrahedrons (see Fig. 4.3) with one common face, yielding $F = 7$, $E = 9$ and $V = 5$, its Euler characteristic is $\chi = F - E + V = 3$.

---

[1] In one of the few experiments, the values of $k \approx 5\ k_{\mathrm{B}}T$, $\bar{k} \approx 2\ k_{\mathrm{B}}T$, and H_0 were determined simultaneously from the size distribution of coexisting spherical vesicles, cylinders and discs [58].

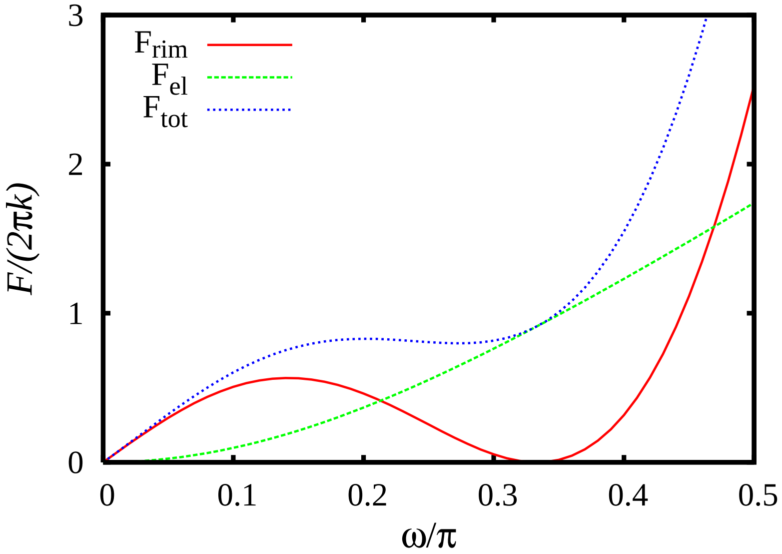

Figure 4.4: The free energy terms $\mathscr{F}_{\rm rim}$, $\mathscr{F}_{\rm el}$ and $\mathscr{F}_{\rm tot}$ of double bubble with $c=a$ plotted versus the angle ω. We choose $\bar{k}=0$ and $H_0R_0=1$ for the elastic part for illustration.

The form of the phenomenological free energy, given by Eq. (4.2), is valid only for smooth surfaces like spheroids or the individual surfaces S_1, S_2 and S_3. In order to introduce the energy of the rim phenomenologically, we make use of the Gauss–Bonnet theorem $\int dS\,K = 2\pi\chi$ (see Eq. (2.34)), where $\chi = 3$ for the double bubble (see Annotation 4.1). By integrating explicitly the Gaussian curvature K over the three smooth pieces of the double bubble, namely the spheroidal caps $\{S_1, S_3\}$ and the flat membrane S_2 ($K=0$), we find the following expression[2]

$$\sum_{i=1}^{3}\int_{S_i} dS\,K = 4\pi(1+\cos\omega), \tag{4.5}$$

which depends only on the angle ω (see Fig. 4.1b). Since $\int dS\,K = 6\pi$, the difference with respect to Eq. (4.5) represents the contribution of the curvature integral over the rim. This integral accounts for the discontinuity of the shape and yields the angle deficit of the rim as $2\pi\chi - \sum_{i=1}^{3}\int_{S_i} dS\,K = 2\pi(1-2\cos\omega)$. We then assume that the phenomenological free energy of a circular rim is proportional to the square of the angle deficit $(1-2\cos\omega)$ multiplied by the rim length $2\pi R_{\rm m}$

$$\mathscr{F}_{\rm rim} = \gamma(1-2\cos\omega)^2 2\pi R_{\rm m}, \tag{4.6}$$

where the coefficient of proportionality γ represents the line tension. The value of γ can be estimated by considering the formation of vesicles due to edge effects and compar-

---

[2] By using Eqs. (A.2), (A.6) it is easy to show that

$$\int_0^{v_P} dS\,K = 2\pi(1-\Delta)\int_{\cos v_P}^{1}\frac{dx}{\lambda^{3/2}} = \left.\frac{2\pi x}{\sqrt{\Delta x^2+(1-\Delta)}}\right|_{\cos v_P}^{1} = 2\pi\left(1-\frac{\cos v_P}{\sqrt{\cos^2 v_P+\frac{c^2}{a^2}\sin^2 v_P}}\right) \overset{\text{Eq. (4.4)}}{=} 2\pi(1+\cos\omega).$$

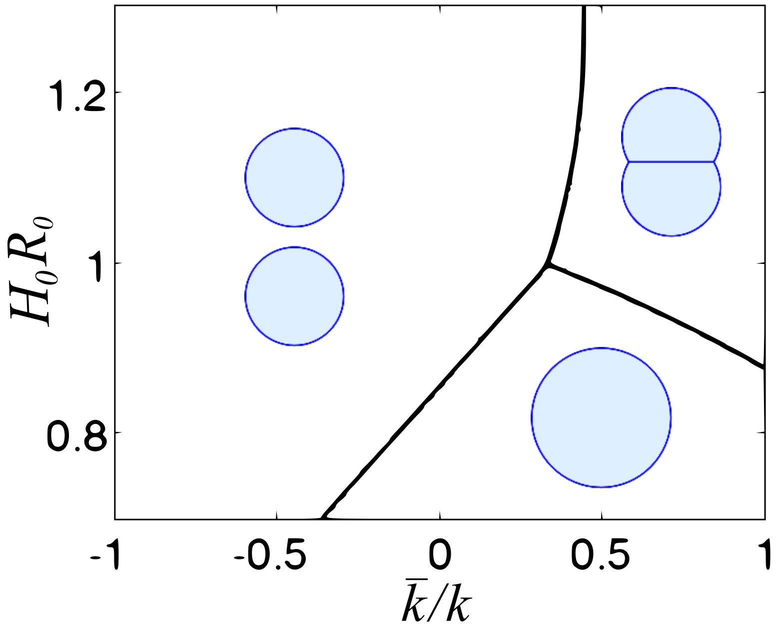

Figure 4.5: Phase diagram showing regions where two spheres with radius R_0, a standard double bubble with $c = a$ and $\omega = \pi/3$, and one single vesicle with radius $\sqrt{2}R_0$ have the lowest free energy. The parameters H_0, k and $\bar{k}$ depend on temperature and pressure [41].

ing the free energy of the two limiting cases, namely a disc with $F_{\text{disc}} = 2\pi\gamma R_{\text{d}} = 4\pi\gamma R_0$ and a sphere with $F_{\text{sphere}} = 4\pi 2k$, yielding $\gamma = 2k/R_0$ [52, 83]. Our conjecture for the form of the rim free energy $\mathscr{F}_{\text{rim}}$ is similar to the line tension with an effective angular dependence proposed in [81] to justify the occurrence of slope discontinuities between different membrane domains. Also for crystals, it has been demonstrated mathematically in [84], that the cusps that are often present at crystal surfaces can be intrinsic property of equilibrium shapes and not necessarily due to defects.

We begin by considering the symmetric case, namely a double bubble composed of two spherical caps with

$$c = a = R = R_0\sqrt{\frac{8}{4(1+\cos\omega)+\sin^2\omega}}, \tag{4.7}$$

which is easy to derive from the condition of constant surface, yielding the limiting case $R|_{\omega=0} = R_0$. The result for elastic energy is

$$\mathscr{F}_{\text{el}} = 4\pi k(1+\cos\omega)\left[(1-RH_0)^2+\frac{\bar{k}}{2k}\right]+2\pi k\sin^2\omega(RH_0)^2, \tag{4.8}$$

and for the rim energy is $\mathscr{F}_{\text{rim}} = 2\pi\gamma R\sin\omega(1-2\cos\omega)^2$. The ω-dependence of these terms is shown in Fig. 4.4. The rim energy vanishes at $\omega = 0$ when two vesicles just touch and at $\omega = \pi/3$ when the angle between three surfaces is $2\omega = 2\pi/3$ (see Fig. 4.1) that coincides with the Plateau's rule for soap films. However, contrary to soap bubbles, the elastic energy grows with ω so that the total free energy $\mathscr{F}_{\text{tot}} = \mathscr{F}_{\text{el}} + \mathscr{F}_{\text{rim}}$ does not necessarily have a minimum in the vicinity of $\omega = \pi/3$, depending on the relative contribution from $\mathscr{F}_{\text{el}}$. These results show that with this approach we can obtain the correct limiting

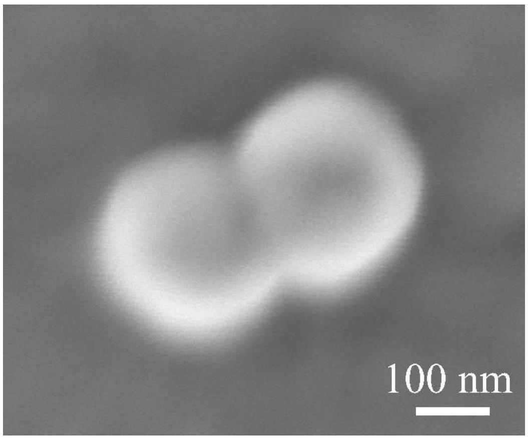

Figure 4.6: Scanning electron microscopy (SEM) image of 6T vesicles on a metallic surface found after evaporation of a solvent.

cases. Figure 4.5 presents the phase diagram for the relative stability of spherical vesicles and double bubbles in the plane of the parameters $(\bar{k}/k)$–(H_0R_0). Thermal fluctuations can be taken into account via the renormalization of the bending and Gaussian rigidity given by Eqs. (2.45). Therefore, an increase in temperature might be enough to induce shape transformations. In Fig. 4.6 we show a SEM (scanning electron microscopy) image of a structure formed by self-assembled bolaamphiphilic sexithiophene (6T) molecules that usually form hollow spherical vesicles [64]. The angle between two spherical parts in this image suggests the possibility that this structure is a double bubble and not two adhering vesicles. It would be interesting to apply other experimental techniques, such as TEM (transmission electron microscopy), to investigate this issue.

4.3 The effect of magnetic field

Now consider the effect of magnetic field, which tends to align diamagnetic molecules and usually leads to deformation of spherical vesicles towards superspheroid like the one measured and explained in [64, 65]. Here, we consider the possibility that magnetic fields could affect the topology as well. We minimize the total free energy

$$\mathscr{F}_{\text{tot}} = \mathscr{F}_{\text{el}} + \mathscr{F}_{\text{rim}} + \mathscr{F}_{\text{mag}}, \tag{4.9}$$

with respect to the deformation c/a for a given value of ω. The elastic energy $\mathscr{F}_{\text{el}}$ and the rim energy $\mathscr{F}_{\text{rim}}$ are given by Eqs. (4.2) and (4.6), respectively, and the magnetic energy, assuming that the membrane S_2 is perpendicular to the direction of the magnetic field, is

$$\mathscr{F}_{\text{mag}} = -\frac{\Delta\chi D B^2}{2\mu_0}\Big(\int dS\, n_z^2 + \pi R_{\text{m}}^2\Big), \tag{4.10}$$

where $\Delta\chi = \chi_\parallel - \chi_\perp$ is the difference of magnetic susceptibility along the long and short axes of the molecule and D is the length of the molecule and the last term is the contribution of the flat disk with radius R_{m} (Eq. (4.1)). Whenever the reduction in magnetic

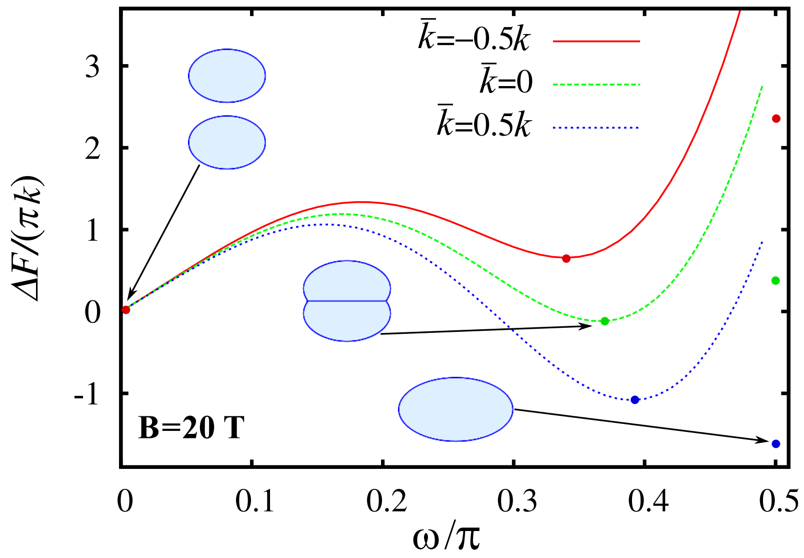

Figure 4.7: Variation of the minimum of the total free energy $\Delta\mathscr{F} = \min_{\omega=\mathrm{const}} \mathscr{F}_{\mathrm{tot}}(c/a) - \min_{\omega=0} \mathscr{F}_{\mathrm{tot}}(c/a)$ for magnetic field $B = 20$ T. The thick dots on each curve indicate the local minima separated by barriers. For some cases we show the corresponding equilibrium shapes. For this plot the parameters are $H_0R_0 = 1$, $R_0 = 100$ nm, $D = 5$ nm, $\Delta\chi = 10^{-5}$.

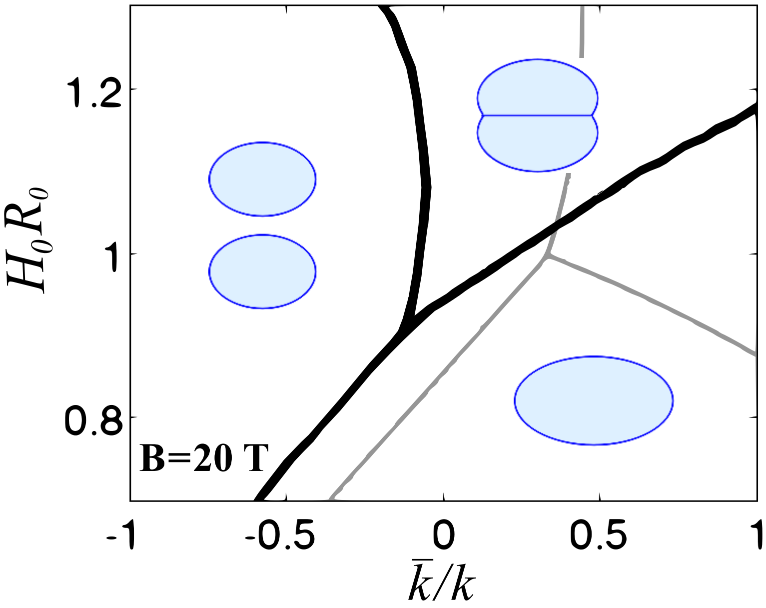

Figure 4.8: Phase diagrams enclosing three regions with topologically different shapes: thick black lines ($B = 20$ T) and grey thin lines ($B = 0$ T same as Fig. 4.5). Shapes with different topologies illustrate schematically the regions of the lowest free energy.

energy $\mathscr{F}_{\text{mag}}$ due to the presence of the membrane compensates the elastic energy $\mathscr{F}_{\text{el}}$ and the energy of the rim $\mathscr{F}_{\text{rim}}$, the formation of a double bubble is favored.

We show first the free energy, minimized over the deformation c/a, for all possible values of ω in a magnetic field chosen as $B = 20$ T (see Fig. 4.7). Magnetic fields of such intensity are typically used to study diamagnetic self-assemblies as we have discussed in the previous chapter. We distinguish three deep minima, separated by high barriers, corresponding to the three equilibrium shapes. By varying the value of the Gaussian rigidity we find as the ground state: two spheroids for $\bar{k} = -0.5k$, a deformed double bubble with $\omega \simeq 0.37\pi$ for $\bar{k} = 0$, and a single spheroid for $\bar{k} = 0.5k$ with comparable values of deformation c/a. Nevertheless, the presence of three separated minima means that the experimentally observed shapes would depend on the kinetics of the system and that under certain conditions all three shapes could exist simultaneously. In Fig. 4.8 we illustrate the phase behaviour of the studied shapes at $B = 20$ T compared to the one at $B = 0$ T in Fig. 4.5. As we expected, in presence of a magnetic field, the area in the phase diagram of stable deformed double bubbles and single spheroids increases significantly, which leads to a larger probability of finding these shapes for the fluctuating spherical vesicles. These results also show that the change in topology from sphere to double bubble can be induced not only by temperature but also by magnetic fields.

4.4 Conclusions

In conclusion, we found that the double bubble, the surface of smallest area enclosing two equal volumes, also minimizes, under certain conditions, the free energy of self-assembled elastic vesicles. We have explicitly shown that magnetic fields can be used to alter not only the shape and the size, but also the topology of two diamagnetic vesicles. Considering the possibility of other topologies is useful when analyzing experimental results and establishing whether self-assemblies are in equilibrium or not. The calculations presented in this chapter may be thought of as a first step to consider the formation of foam during self-assembly, like the one observed in [37]. We hope that our work will provide a motivation for new experiments.

Acknowledgements

It is a pleasure to acknowledge helpful discussions with Michael Mueger, Philippe Nozières and Efim Kats.

5

Topological defects in aromatic assemblies

Contents

So far the mathematical description of fluid membranes was based on the assumption that the curvature is the only order parameter accounting for the shape of the vesicles. Here we show that the regular packing of flat aromatic molecules on a curved surface results in unavoidable topological defects, which could determine the shape and the topology of vesicles. As an example we study the packing of 6T molecules, known to self-assemble into spherical vesicles (see chapter 3). The competing interactions between bending energy and the defects lead to elongated shapes.

5.1 Beyond fluid membranes

Until now we considered fluid membranes with zero shear modulus and no internal structure or no in-plane order. However, membranes may exist in different thermodynamic states with varying degrees of orientational and translational order [85]. At low temperatures the membranes may freeze to a *crystalline* phase, where the molecules form a regular lattice and can be characterized by the quasi long-ranged positional order. Bending of crystalline membranes would inevitably cause stretching or contraction of the in-plane bonds and thus would cost more energy compared to the fluid membranes. In the following we briefly mention crystalline membranes, followed by the discussion of *hexatic* membranes, which are the main concern of this chapter.

5.1.1 Crystalline membranes

The free energy of crystalline membranes is written as [86, 87]

$$\mathscr{F}_{\text{cryst}} = \frac{1}{2}k\iint d^2x\,(\nabla^2 h)^2 + \frac{1}{2}\iint d^2x\,\big(2\mu u_{ij}^2 + \lambda u_{kk}^2\big). \tag{5.1}$$

The first term is the bending energy, identical to the one of fluid membranes with h being the height of the out-of-plane fluctuations (see Annotation 2.2). The second term is the strain-elasticity of two-dimensional solids, where μ and λ are called Lamé coefficients [88]. The strain tensor u_{ij} is defined as

$$u_{ij} = \frac{1}{2}(\partial_i u_j + \partial_j u_i + \partial_i h \partial_j h). \tag{5.2}$$

Since $\mathscr{F}_{\text{cryst}}$ is quadratic in u, the last term in Eq. (5.1) can be exactly integrated to produce an effective free energy for h as

$$\mathscr{F}_{\text{cryst}} = \frac{1}{2}k\iint d^2x\,(\nabla^2 h)^2 + \frac{1}{8}K_B\iint d^2x\,\big(P_{ij}^T \partial_i h \partial_j h\big)^2, \tag{5.3}$$

where

$$P_{ij}^{T} = \delta_{ij} - (\nabla_i \nabla_j)/\nabla^2 \quad \text{and} \quad K_B = \frac{4\mu(\mu+\lambda)}{2\mu+\lambda}. \tag{5.4}$$

The nonlinear coupling of in-plane strain modes and out-of-plane height modes as in Eq. (5.2) (bending of the flat membrane causes the stretching of the bonds) leads to non-trivial properties distinct from those of fluid membranes. For example, the long-wavelength bending rigidity is stiffened rather than softened as in fluid membranes (see Eq. (2.45)) and the in-plane bulk and shear moduli (zero for fluid membranes) are softened [87].

Annotation 5.1 Graphene

Graphene is a one atom thick sheet of carbon atoms packed in the honeycomb crystal lattice with lattice constant $a = 0.246$ nm. Unlike membranes self-assembled from molecules and characterized by a finite (although small) thickness, graphene with zero thickness could serve as an excellent example of crystalline membrane and thus a nice model system. It is a truly two-dimensional crystal, regardless of the Mermin–Wagner theorem, which states that there is no long-range crystalline order for $T > 0$ in two (or less) dimensions, because of the violent thermal fluctuations. The calculated bending rigidity of graphene is $1.76 \cdot 10^{-19}$ J at room temperature [89], the bulk and shear moduli are $\simeq 198$ J/m^2 and $\simeq 159$ J/m^2 respectively [90]. Because of such strong elastic moduli graphene remains relatively flat and defectless even at high temperatures ~ 3500 K. For more information on graphene, see for instance the review written by Katsnelson [91].

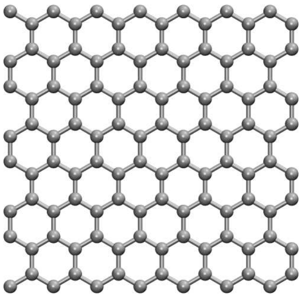

5.1.2 Hexatic membranes

Hexatic membranes, although fluid, are characterized by in-plane orientational order, with order parameter $\mathbf{m}(\mathbf{x})$ lying at the tangent plane of the membrane at point $\mathbf{x}$. The elastic free energy of a hexatic membrane, which cannot be recast into the form of the free energy for fluid membranes is [85, 47, 92]

$$\mathscr{F}_{\text{hex}} = \frac{K_A}{2} \iint dS\, D_i m^j(\mathbf{u}) D^i m_j(\mathbf{u}), \tag{5.5}$$

where $\mathbf{u} = \{u, v\}$ is a set of internal coordinates, and D_i is the covariant derivative with respect to the metric of the surface. The constant K_A is called the hexatic stiffness, which measures the coupling between the in-plane orientations of neighbouring bonds. The minimal energy configuration is given by neighbouring $\mathbf{m}(\mathbf{u})$ vectors which differ only by parallel transport. In fact, according to the Gauss' "Theorema egregium", tangent vectors parallel transported along a close loop are rotated by an amount equal to the Gaussian curvature K integrated over the enclosed area [47, 92, 45]. Therefore, a non-zero Gaussian curvature of the surface leads to a 'frustration' in orientation of tangent vectors, resulting in the presence of topological defects called *disclinations*.

Topological defects

A topological defect is a point around which the tangent vector field rotates by an integer q_i multiple of 2π. The integer, q_i, is called the *index* or *winding number*. The Poincaré–Hopf index theorem [45] says that the sum of indices q_i on a compact surface S equals to the Euler–Poincaré characteristic $\chi(S)$

$$\sum_i q_i = \chi(S) = \frac{1}{2\pi}\int dS\, K. \tag{5.6}$$

This expression nicely connects physics with topology and it may be considered as the generalization of the Gauss-Bonnet theorem (Eq. (2.34)).

Annotation 5.2 Fractional index

The index q_i is an integer number if we consider the vector field as an order parameter living on a surface. In general an order parameter $\mathbf{m}(\mathbf{x})$ can be invariant under rotation by an angle $2\pi p/l$ (p and l are integers). Thus the index of the defect can take non-integer values $\pm 1/l, \pm 2/l, \ldots$. In figure we show disclinations with $q_i = 1/2$ and $q_i = -1/2$ in nematic liquid crystals with π rotational symmetry ($\mathbf{m} \to -\mathbf{m}$, $l = 2$). For a nice fundamental review on topological defects in ordered media see reference [93].

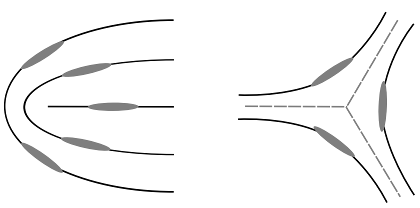

An alternative representation of Eq. (5.5) can be given in terms of the defects themselves [94, 95, 92]

$$\mathscr{F}_{\text{hex}} = -\frac{K_A}{2}\int d^2\mathbf{x}\sqrt{|g(\mathbf{x})|}\int d^2\mathbf{y}\sqrt{|g(\mathbf{y})|}\,[K(\mathbf{x}) - s(\mathbf{x})]\,\frac{1}{\Delta}\Big|_{\mathbf{x},\mathbf{y}}[K(\mathbf{y}) - s(\mathbf{y})] \tag{5.7}$$

where $|g(\mathbf{x})|$ is the determinant of the metric tensor, $K(\mathbf{x})$ is the Gaussian curvature, and $s(\mathbf{x})$ is the disclination density given by

$$s(\mathbf{x}) = 2\pi\sum_{i=1}^{N_d} q_i\,\delta(\mathbf{x} - \mathbf{x}_i)/\sqrt{|g(\mathbf{x}_i)|}, \tag{5.8}$$

with the sum over all defects N_d, located at the sites $\mathbf{x}_i$ with index q_i. Defects interact with each other and with the Gaussian curvature, like charged particles with the background charge distribution [96]. Because of the repulsive nature of defect interactions, the situation with the maximum separation between the defects is energetically favourable. However, there is a competition between this effect and the coupling of defects with the Gaussian curvature. As the Gaussian curvature is increased, the splay or bend of the director **m** decreases, resulting in the reduction of $\mathscr{F}_{\text{hex}}$. In order to quantify the energetics of defects one needs to calculate the inverse Laplace–Beltrami operator $1/\Delta$ or the corresponding Green's function for an arbitrary surface, given as

$$\Gamma(\mathbf{x},\mathbf{y}) = -\frac{1}{\Delta}\Big|_{\mathbf{x},\mathbf{y}}, \qquad \Delta \equiv \frac{1}{\sqrt{|g|}}\partial_i\big(g^{ij}\sqrt{|g|}\partial_i\big). \tag{5.9}$$

In the case of crystalline order on a surface (crystalline membranes) the topological defects are called *dislocations* and the defect interactions are given by an equation identical in form to Eq. (5.7), with K_A substituted by K_B (Young modulus, Eq. (5.4)) and $1/\Delta \to 1/\Delta^2$ [97].

5.2 Flat plaquettes versus rods

The phenomenological approach considered in the previous chapters describes qualitatively the arrangement of molecules on the surface of vesicles as if they were rods aligned along the normals **n** of the surface (see Fig. 5.1b). However, the constituents of self-assembled vesicles are often molecules with a flat aromatic core (as the one studied in chapter 3), which should be modelled as plaquettes rather than rods. Consider now the regular packing of flat plaquettes on a curved surface, e.g. on a spherical cap (see Fig. 5.1e): every plaquette can be described by a director **m** (headless vector) normal to the plane of the plaquette and thus tangent to a sphere. We will discuss later whether the director **m** is a true vector. The regular packing of flat plaquettes results in hexatic or in-plane orientational order and consequently leads to unavoidable topological defects, like the one shown in Fig. 5.1e, for a surfaces with non-zero Gaussian curvature. These *intrinsic* topological defects are caused by the symmetry of the packed molecules and not by the temperature-induced phase transition from the Sm-A phase to the Sm-C phase with tilted molecules [85, 98]. The defects should be taken into account when considering the aromatic core–core (plaquette–plaquette) interactions. This simple geometric approach is the first step to incorporate the microscopic details of the core–core interactions into a phenomenological model.

The Helfrich model (Eq. (2.44)) and the spontaneous bending model (Eq. (2.51)) predict the sphere as an equilibrium shape of vesicles. Unlike two-dimensional spherical crystals [97, 99], the defects in aromatic self-assemblies could influence the geometry and the topology of the structure as a whole. Therefore, we allow spherical vesicles to deform towards oblate or prolate spheroid in order to determine the minimum energy configuration given by the sum of elastic energy and of the energy of interacting defects. We also consider double bubble as an example of another topology (χ) and thus with different number of topological defects according to Eq. (5.6).

The number of topological defects depends on the Euler characteristic of the surface χ but also on the intrinsic symmetry of the self-assembled molecules. Consider the previous example of 6T molecule (see chapter 3 and Fig. 3.2a), known to self-assemble into spherical vesicles [64]. The aromatic 6T core is composed of six thiophene rings enclosed in a rectangle. We can write for 6T the following symmetry operations which leave one point unmoved [100]

$$m_z = \begin{pmatrix} 1 & & \\ & 1 & \\ & & -1 \end{pmatrix} \quad \text{and} \quad 2_z = m_x m_y = \begin{pmatrix} -1 & & \\ & -1 & \\ & & 1 \end{pmatrix}, \tag{5.10}$$

where m denotes the symmetry operations such as mirror-reflections across line. Their product $m_x m_y m_z = \begin{pmatrix} -1 & & \\ & -1 & \\ & & -1 \end{pmatrix}$, acting on a vector, results in the inversion symmetry, which means that there are no invariant vectors in the plane of the molecule. This defines a *unique normal* **m** to the plane of the plaquette which will be a tangent vector to a sphere. Instead, for 5T core, the point group is different[1], containing the operators

$$m_z = \begin{pmatrix} 1 & & \\ & 1 & \\ & & -1 \end{pmatrix}, \quad m_y = \begin{pmatrix} 1 & & \\ & -1 & \\ & & 1 \end{pmatrix}, \quad 2_x = m_y m_z = \begin{pmatrix} 1 & & \\ & -1 & \\ & & -1 \end{pmatrix}, \tag{5.11}$$

which leaves a vector $v = (x, 0, 0)$ invariant under symmetry transformations. This additional symmetry of the core yields a director to the plane of the molecule with $\mathbf{m} \to -\mathbf{m}$. We may generalize our results to even and odd number of thiophene and benzene rings. For the tangent vector field on a sphere ($\chi = 2$), there are two topological defects with vorticity 2π (topological charge $q_i = +1$), located at the north and south poles (Fig. 5.3), because of the repulsive nature of defect interactions. Whereas for directors there are four defects with vorticity π ($q_i = +1/2$) [85, 95], located on a sphere at the vertices of a tetrahedron. For vector field on a double bubble ($\chi = 3$) there are three topological defects located at the top of spherical caps and at the center of a flat membrane (see Fig. 5.3). The vorticity at the center of a membrane is always $q_i = +1$ irrespective of the details of molecular packing (radially or concentrically). Based on the example of 6T molecules, which can be generalized to any aromatic molecule with inversion symmetry, we consider in the following the interaction of two and three topological defects on surfaces with the topology of a sphere and double bubble respectively.

5.3 Free energy of interacting defects

According to Eq. (5.7) the quantitative understanding of defect interactions requires the calculation of the Green's function for a curved surfaces, which could be an overwhelming task. However, this non-trivial problem can be solved by projecting conformally a complex surface onto a simple one, e.g. plane or sphere, where the Green's function is known [101]. The conformal mapping preserves the angles, but not the lengths, which is crucial for the invariance of the free energy (Eq. (5.5)) given the same topology.

---

[1] The molecules with odd number of thiophene rings have $mm2$ point group, whereas for the even number the point group is $2/m$.

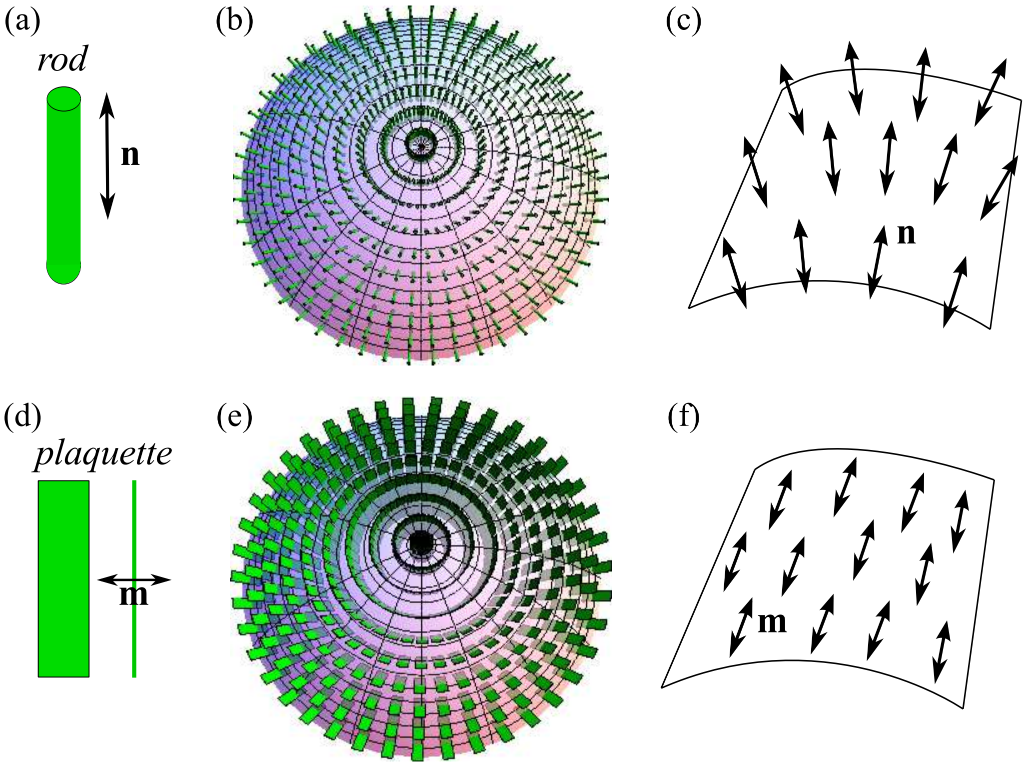

Figure 5.1: The arrangement of rod-shaped molecules (a) on a spherical cap (b), described by the director $\mathbf{n} \to -\mathbf{n}$ normal to the surface (c). Flat plaquettes (d), described by in-plane tangent field with director $\mathbf{m} \to -\mathbf{m}$ (f), cannot arrange continuously on a surface with non-zero Gaussian curvature (e).

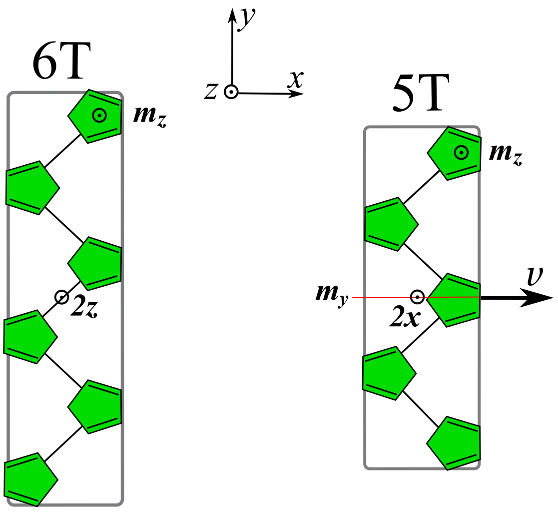

Figure 5.2: Schematic representation of aromatic molecules with six (6T) and five (5T) thiophene cores. We show the possible symmetry transformations for both molecules and the invariant vector v for 5T molecule.

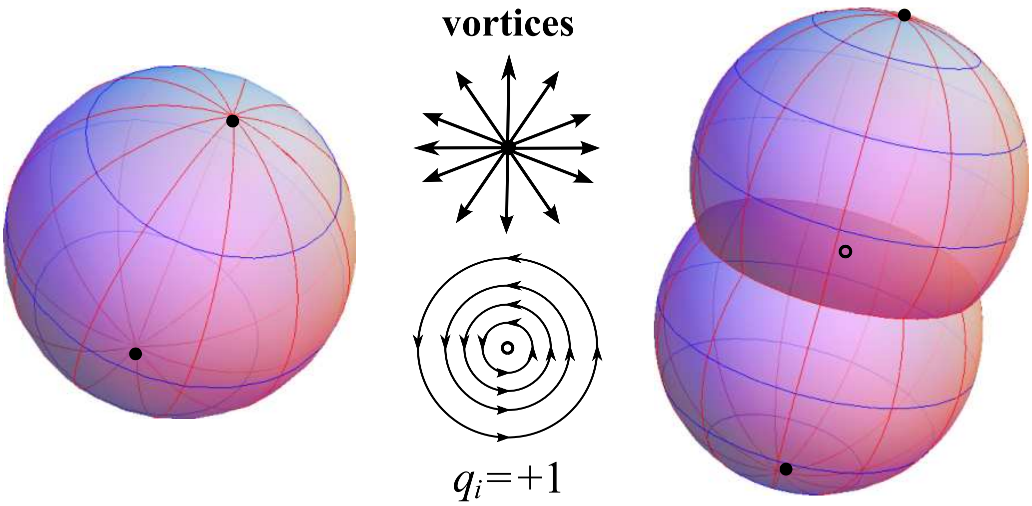

Figure 5.3: Two vortices on a sphere located at the north and the south poles (thick dots). Three vortices on a double bubble located at the top of the spherical caps and at the center of the membrane.

Let us consider a spheroid, which is a surface of revolution (see Annotation 2.1) given by the following parametrization

$$\mathbf{x}(u,v) = \big(a\sin v\cos u,\, a\sin v\sin u,\, c\cos v\big), \qquad 0 \leqslant v \leqslant \pi, \quad 0 \leqslant u \leqslant 2\pi, \tag{5.12}$$

with semiaxes c and a. Then, the metric of a spheroid is given by

$$ds_1^2 = (a^2\cos^2 v + c^2\sin^2 v)\,dv^2 + a^2\sin^2 v\,du^2. \tag{5.13}$$

The mapping of spheroids onto a sphere with metric $ds^2 = R^2(d\theta^2 + \sin^2\theta\,d\phi^2)$ is said to be conformal if

$$ds^2 = e^{2\lambda(\mathbf{u})}ds_1^2, \tag{5.14}$$

where $e^{2\lambda(\mathbf{u})}$ is called the conformal factor, which varies with position $\mathbf{u} = \{u, v\}$ on the spheroid. Because of the rotational symmetry $u = \phi$ and thus the conformal factor depends only on a single parameter v. By equating two metrics we find that

$$e^{2\lambda(v)} = \frac{R^2\sin^2\theta}{a^2\sin^2 v}, \qquad \frac{d\theta}{\sin\theta} = \pm dv\sqrt{\cot^2 v + \frac{c^2}{a^2}}. \tag{5.15}$$

The explicit analytical expression for the conformal factor can be found by integrating both sides of the second equality (see Annotation 5.3).

The pair Green's function of the deformed sphere can be defined in a similar way to the methods used in reference [101] for superfluids

$$\Gamma(\mathbf{u}_i,\mathbf{u}_j) = -\frac{1}{2\pi}\log\frac{\mathscr{D}_{ij}}{d} + \frac{1}{4\pi}\big(\lambda(\mathbf{u}_i) + \lambda(\mathbf{u}_j)\big), \tag{5.16}$$

where $\mathscr{D}_{ij}$ is the distance between two defects on the sphere (the chord between two points! see Appendix C) and d is the core size of the defect[2]. This representation of

---

[2] At this microscopic scale the continuum theory breaks, so d may be thought of as a cut-off radius.

the Green's function already includes both the interaction between defects (first term) and the position dependent self-energy of the defect (see Appendix C Eq. (C.19)). Using Eq. (5.7) we can write the contribution from the hexatic degrees of freedom, or simpler the free energy of interacting defects, given by

$$\mathscr{F}_{\text{hex}} = 4\pi^2 K_A q_i q_j \Gamma(\mathbf{u}_i, \mathbf{u}_j). \tag{5.17}$$

In the case of two topological defects on a sphere with topological charge $q_i = q_j = +1$, the minimum of $\mathscr{F}_{\text{hex}}$ corresponds to the defects located at the north ($v = 0$) and the south ($v = \pi$) poles[3]. It gives $\mathscr{D}_{ij} = 2R$, and together with Eqs. (5.16) and (5.21) we find the Green's function on spheroids as

$$\Gamma(0, \pi) = -\frac{1}{2\pi}\Big(\log\frac{2a}{d} + \lambda_0(\eta)\Big), \tag{5.18}$$

where $\boxed{\eta = c/a}$.

Annotation 5.3 Conformal factor of a spheroid

Integrating Eq. (5.15) we get

$$\begin{aligned} \log\Big(\tan\frac{\theta}{2}\Big) = g(v) \equiv \\ \equiv -\sqrt{-1+\eta^2}\arctan\left(\frac{\sqrt{-1+\eta^2}\cot v}{\sqrt{\eta^2+\cot^2 v}}\right) - \log\big(\cot v + \sqrt{\eta^2+\cot^2 v}\big). \end{aligned} \tag{5.19}$$

Substituting $\sin\theta = 2\tan(\theta/2)/(1+\tan^2\theta/2)$ into Eq. (5.15) we find the conformal factor

$$e^{2\lambda(v)} = \frac{R^2}{a^2 \sin^2 v \cosh^2 g(v)}, \tag{5.20}$$

and the limit of interest

$$\lim_{v\to 0}\lambda(v) = \log\frac{R}{a} - \lambda_0(\eta), \quad \text{where} \quad \boxed{\lambda_0(\eta) = \sqrt{-1+\eta^2}\arctan\sqrt{-1+\eta^2}}. \tag{5.21}$$

The Green's function for a double bubble cannot be derived straightforwardly through the conformal mapping on a sphere because the topology, and thus the number of defects on a double bubble (three) is different from those on a sphere (two). To get around this point we carve a double bubble into geometric pieces (see Fig. 5.4) and project them separately onto a sphere. Then the total Green's function is constructed as the sum of the pair Green's functions defined by Eq. (5.16). The conformal factors for a deformed double bubble are calculated in Annotation 5.4, resulting in the following expressions

---

[3] This statement could be easily verified by plotting $\mathscr{F}_{\text{hex}}$ (Eq. (5.17)) as a function of the parameter v using Eq. (5.20).

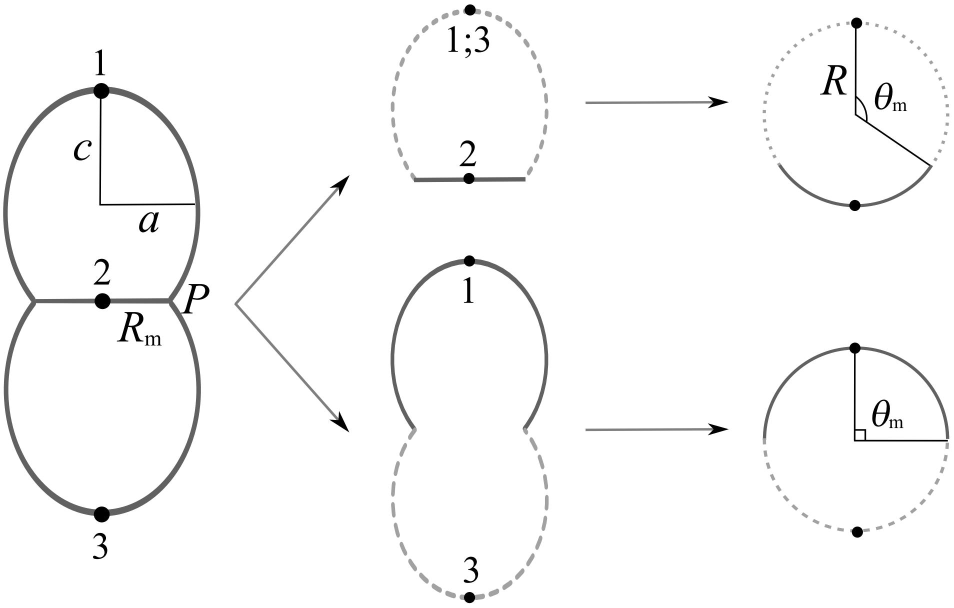

Figure 5.4: Cutting of a double bubble with three topological defects into geometric pieces with two topological defects, which consequently can be projected onto a sphere.

for Γ_{ij}

$$\Gamma_{12} = \Gamma_{23} = -\frac{1}{2\pi}\Big(\log\frac{2a}{d} + \frac{1}{2}\big[\lambda_0(\eta) + g(v_p) + \log(\sin v_p) - \log 2\big]\Big), \tag{5.22}$$

$$\Gamma_{13} = -\frac{1}{2\pi}\Big(\log\frac{2a}{d} + \lambda_0(\eta) + g(v_p)\Big). \tag{5.23}$$

We may notice, however, that the sum of the pair Green's functions for a double bubble counts twice the self energy of every defect, since it was mapped also twice. Taking into account this fact we can write the final expression for the free energy of the hexatic degrees of freedom (Eq. (5.17)) on a double bubble as

$$\mathscr{F}_{\text{hex}} = -\pi K_A\Big(6\log\frac{2a}{d} - \log\frac{2}{\sin v_P} + 2\big[\lambda_0(\eta) + g(v_p)\big]\Big). \tag{5.24}$$

This expression holds only for double bubbles with non-zero size of the membrane with ($R_{\text{m}} = a\sin v_P$, $v_P \neq \pi$). In the limiting case, for two spheroids touching at a point (vanishing membrane, $v_P = \pi$) there is a logarithmic divergence of the free energy and one should reconsider the construction of the Green's function. Since we are not interested in this particular case, we do not pursue this study further.

Annotation 5.4 The Green's function for a deformed double bubble

The stereographic projection of the flat membrane with polar coordinates (r, ϕ) onto a sphere requires the following change of variables $\phi = \phi$ and $r = R\cot(\theta/2)$ (see Fig. 5.4). Then the metric of a sphere in a polar coordinates is given by

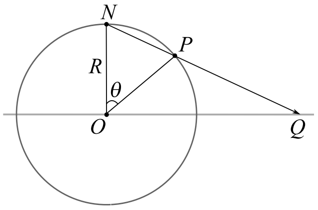

$$ds^2 = \frac{4R^4}{(R^2 + r^2)^2}(dr^2 + r^2 d\phi^2), \quad r \in [0, R_\mathrm{m}]. \tag{5.25}$$

And thus the conformal factor for $r = 0$ (the defect at the center of the membrane) equals 4. The membrane with a finite radius $R_\mathrm{m} = a \sin v_P$ (see Annotation 4.1) is mapped onto a spherical cap (not a sphere) and we can define θ_m (see Fig. 5.4) as $\theta_\mathrm{m} = 2\,\mathrm{arccot}(R_\mathrm{m}/R)$. To guarantee that the mapping of every geometric piece (see Fig. 5.4) is bijective (one-to-one) we need to require that the image of the point P coincides with θ_m, or that the following condition (see Eq. (5.19) holds

$$\log\Big(\tan\frac{\theta}{2}\Big) = g(v) + \log\Big(\tan\frac{\theta_\mathrm{m}}{2}\Big) - g(v_P). \tag{5.26}$$

Together with Eq. (5.21) it gives

$$\lim_{v\to 0}\lambda(v) = \log\frac{R}{a} - \lambda_0(\eta) + \log\Big(\tan\frac{\theta_\mathrm{m}}{2}\Big) - g(v_P). \tag{5.27}$$

5.4 Elongated shapes are desirable

In this section we study the equilibrium shapes of spherical vesicles in presence of topological defects. We calculate the total free energy as the sum of bending energy $\mathscr{F}_\mathrm{el}$ and of the energy associated with topological defects $\mathscr{F}_\mathrm{hex}$, namely

$$\mathscr{F}_\mathrm{tot} = \mathscr{F}_\mathrm{el} + \mathscr{F}_\mathrm{hex} = 2k \iint dS\, H^2 + 4\pi^2 K_A q_i q_j \Gamma(0, \pi). \tag{5.28}$$

The mean curvature H^2 at a given point depends on the change of the normal vector around this point, characterizing the local properties of the surface. The non-local (long-ranged) interactions of the defects are described by the Green function $\Gamma(\mathbf{x}_i, \mathbf{x}_j)$, which depends only on the metric of the surface. The competition between two terms in Eq. (5.28) leads to frustration, because the defects favour high Gaussian curvature [96], which inevitably leads to high mean curvature (due to $H^2 \geqslant K$), and consequently to an increase of the bending energy. The topological defects in self-assemblies account for the competition between local interactions of aromatic cores and the topological constraints, whereas the details of microscopic potentials reside in the bending rigidity k and the hexatic constant K_A. In our system, the ratio K_A/k is the only governing parameter, related to details of intermolecular interactions for a given temperature. Although

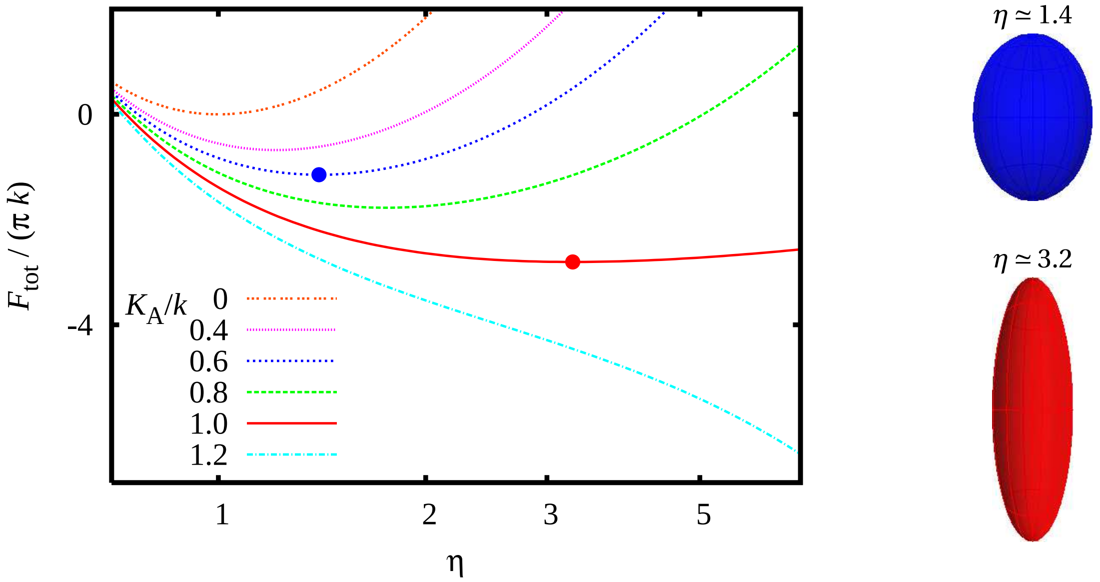

Figure 5.5: The normalized total free energy $\mathscr{F}_{\mathrm{tot}}/\pi k$ for a deformed spherical vesicle as function of $\eta = c/a$ (the semiaxes of spheroid) in logarithmic x-scale. The minimum of $\mathscr{F}_{\mathrm{tot}}$, corresponding to a sphere $\eta = 1$ for $K_A = 0$, shifts to higher values of η with hexatic constant K_A compared to bending rigidity k. For the ratio $K_A/k = 1.2$ we expect an instability towards rod-like structures. Substituting Eqs. (A.36),(5.18) into Eq. (5.28) we find analytical expression of $\mathscr{F}_{\mathrm{tot}}$. The calculations were done, assuming that the surface area is constant. On the right the equilibrium shapes corresponding to the values $K_A = 0.6k$ (top) and $K_A = k$ (bottom).

the value of the bending rigidity $k = (0.64 \pm 0.2) \cdot 10^{-21}$ J was found from experimental measurements of magnetic deformations of 6T spherical vesicles in isopropanol (see chapter 3, and the reference [65]), the value of the hexatic constant K_A is a less accessible parameter. Assuming that π-π interactions between thiophene molecules give the main contribution to the values of k and K_A we can roughly estimate the ratio K_A/k based on the results of *ab initio* molecular orbitals calculations for different geometries of thiophene dimer [102, 103], yielding K_A/k of the order of unity.

Figure 5.5 shows the total free energy for different values of K_A/k as a function of $\eta = c/a$, the ratio of the semiaxes of spheroids with defects located at $z = c$ and $z = -c$. In presence of topological defects, the equilibrium shapes, corresponding to the minimum of $\mathscr{F}_{\mathrm{tot}}$, are shown for two values of K_A/k. When the contribution $\mathscr{F}_{\mathrm{hex}}$ is not dominant ($K_A \lesssim 0.6k$) the equilibrium shapes are close to spherical, but for $K_A \simeq k$ they are elongated with $\eta \simeq 3.2$. It is not surprising that the defects favour high Gaussian curvature K, since the splay of the tangent vector field decreases with K. For small values of the bending rigidity ($K_A > k$) we expect an instability towards infinitely long tubular structures. This holds for both spheroids and double bubbles. A similar elongation of phospholipid vesicles has been predicted to occur as a function of temperature at the phase transition between Sm-A phase and Sm-C phase [98].

As was explained in the previous chapter, double bubbles have an extra term in the free energy associated with the circular rim with a singularity, where three surfaces meet (see

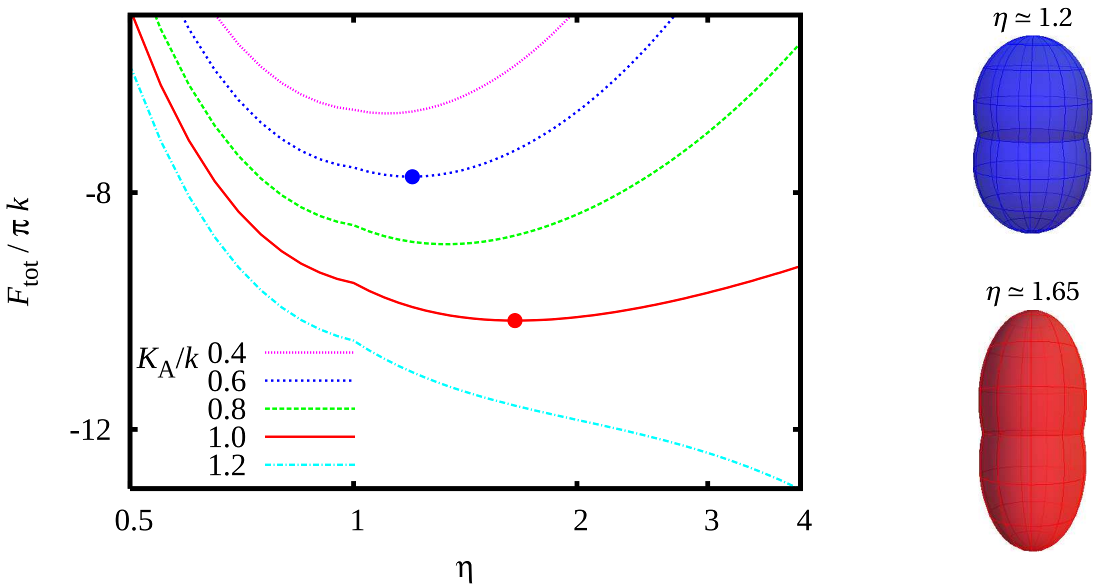

Figure 5.6: The normalized total free energy $\mathscr{F}_{\rm tot}/\pi k$ for a deformed double bubble (we choose $\omega = 0.37\pi$) as a function of $\eta = c/a$ in logarithmic scale. For $K_A = 0$ the equilibrium cap is spherical, for $K_A > k$ there is an instability, similar to the one in Fig. 5.5, towards infinitely long tubular structures. The equilibrium shapes corresponding to the values $K_A = 0.6k$ (top) and $K_A = k$ (bottom). The surface area is kept constant.

Eq. (4.6)). We take into account this term also in the present calculations. We find here that the minimum of the total free energy occurs when $\omega = 0.37\pi$ (see Fig. (4.1)b) irrespective of the contribution from the hexatic order[4]. We present in Fig. 5.6 the free energy of deformed double bubbles for a chosen value of $\omega = 0.37\pi$. The elongation of shape with increasing K_A (or decreasing k) is similar to the one found for the sphere with defects. However, the absolute value of the deformation η of the double bubble with defects is smaller than that for the sphere.

5.5 Discussion

Usually, the appearance of topological defects is related to the temperature-induced phase transition effect, when, upon a cooling, fluid membranes attains an in-plane orientational order, like in Sm-C phase with tilted molecules [85, 98]. Recently, Nelson [95] proposed an elegant way to generate topological defects by coating spherical colloidal nanoparticles with anisotropic objects like nematic liquid crystals. The high-energy core of defects can be used as sites for chemical activity and as potential spots for the assembly of three dimensional architectures. This method based on the simple laws of topology opens an attractive possibility to design functional systems in a controlled way. In this chapter we have considered an alternative mechanism of generating topological

---

[4] Unlike previous chapter, here we consider the case of symmetric 6T molecules with $H_0 = 0$ in the bending energy, which favours the presence of the flat membrane. As the result the minimum of the free energy corresponds to $\omega = 0.37\pi$ instead of $\omega = \pi/3$.

defects in self-assembled structures. Since these structures are not rigid we allow the geometry to change in the presence of topological defects, which crucially differs from the interaction of defects on *frozen* geometries.

We demonstrated that the stacking of flat aromatic molecules in self-assembled spherical vesicles leads to topological defects. The essential difference in symmetry between molecules with even and odd number of thiophene groups results in two and four topological defects on a sphere, respectively. In the case of two interacting defects the equilibrium shape of vesicles turns out to be elongated. Moreover, for small values of the bending rigidity the instability towards long tubular structures happens both for spheroids and for double bubbles. The nature of these intrinsic topological defects could shed light on the new experimental observations of multiwalled cylindrical structures formed from 6T molecules in butanol [68] (see Annotation 3.1). The theory presented here holds only for single layered structures and thus we cannot establish a direct comparison with the experimental observations. Moreover, in real situations, parameters such as k depend also on the particular solvent [54]. In general, the question of how the shape of self-assembled structures is connected with the intrinsic properties, such as the symmetry, of the constituent molecules remains open. Here we proposed a simple geometric approach based on topological defects to establish this connection for molecules with thiophene/benzene aromatic cores. The proposed theory can be used to extract the value of K_A/k from experimental observations of the shape of self-assembled aromatic molecules.

Acknowledgements

I am grateful to Aloysio Janner for his help in understanding the symmetry groups of aromatic molecules.

6 Pattern formation in smectic liquid crystals

Contents

This last chapter deals with another type of frustrated systems, smectic liquid crystals, where the interplay between translational and orientational order leads to a doubly-periodic spatial pattern. To get insight into the experimental observations we propose two approaches for constructing space filling 3D structure of smectic layers. However, the minimal surfaces considered up to now cannot reproduce the ratio of the two periodicities observed experimentally. Nevertheless, we believe that there is a big deal to learn from failures as well as from success.

6.1 Prologue

LIQUID CRYSTALS ARE BEAUTIFUL AND MYSTERIOUS.

This is the opening sentence of the fascinating book "The physics of liquid crystals" written by the Nobel Laureate P. G. de Gennes [63] 35 years ago. After a brief introduction, for more details please consult the books [63, 104], we discuss one of the mysteries posed by liquid crystals.

By cooling down an isotropic liquid, composed of elongated molecules, first we find the nematic phase, where all molecules are aligned along a preferred direction **n** (see Fig. 6.1). By further cooling we find the smectic phase, that can be viewed as a set of two dimensional fluid layers stacked on each other with a well-defined spacing, of the order of nanometers. This phase possesses both orientational order, inherited from nematics, as well as one-dimensional translational order. In this chapter we will discuss only smectics (greek "$\sigma\mu\eta\gamma\mu\alpha$" >> soap), in particular the Smectic-A phase[1], where the director **n** coincides with the normal to the layer.

Our interest in liquid crystals originates from a unique experiment, performed at the HFML [2] by G. Tordini, which can be described as follows:

1. The liquid crystal 8CB was confined in a glass cell in which the surface causes *homeotropic anchoring* (molecules are aligned perpendicular to the surface) along the z-direction as schematically shown in Fig. 6.2.
2. The sample was cooled to the smectic phase in the presence of a magnetic field $B = 7$ T applied in the direction of the x-axis.

---

[1] In nature, there are also Sm-C, Sm-B, Sm-G, Sm-F phases with additional order of molecules within the plane of a layer.

[2] High Field Magnet Laboratory, Nijmegen.

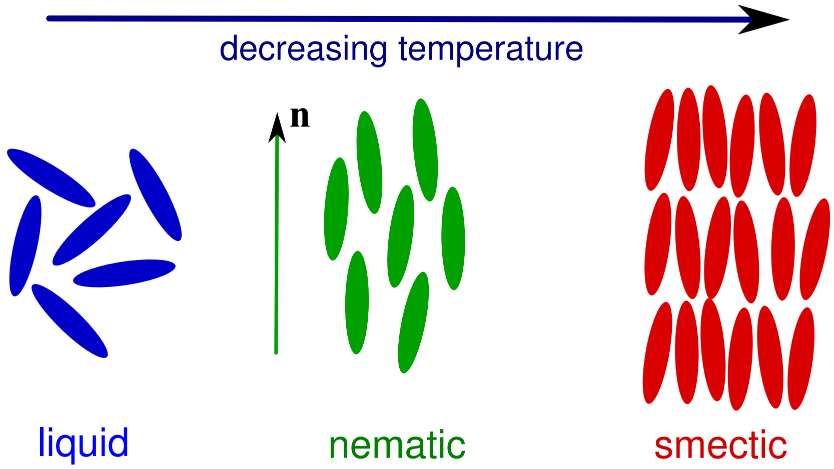

Figure 6.1: Liquid crystal phases, such as nematics and smectics. The former has long-range orientational order; the latter has orientational order and one-dimensional periodicity (here we illustrate three layers).

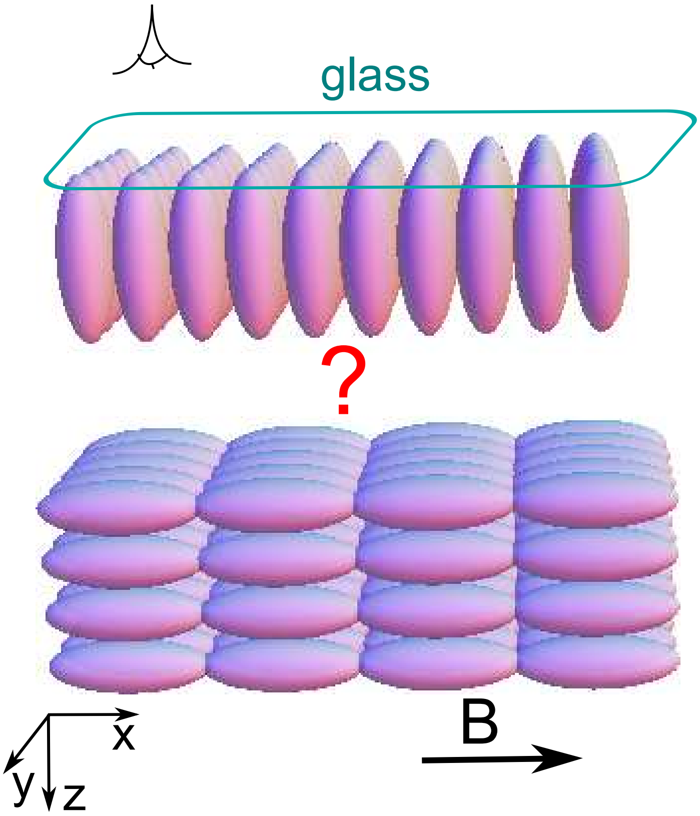

Figure 6.2: A schematic representation of a preferred alignment of 8CB molecules, with 3.2 nm length, under the experimental conditions. At the glass surface the homeotropic anchoring favours the director $\mathbf{n}$ parallel to z-axis, and at the bulk the magnetic field $B = 7$ T aligns the molecules along x-axis. The question mark is our problem: to find the organization of smectic layers between these two incompatible ground states.

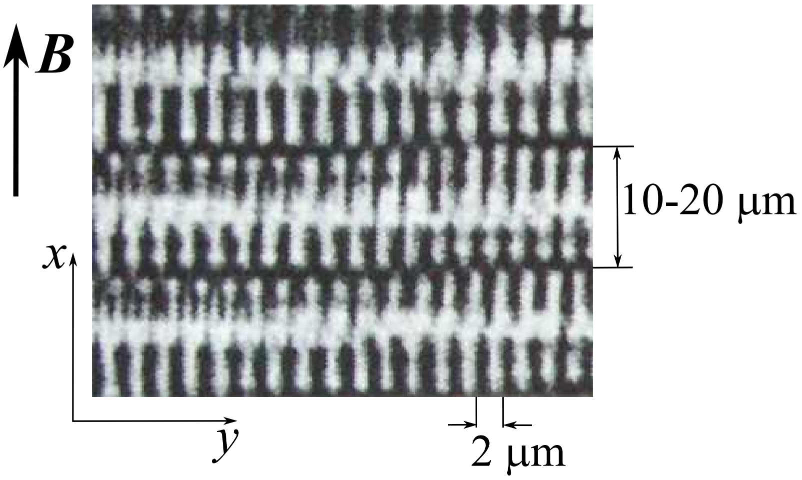

Figure 6.3: Novel doubly-periodic pattern observed at the HFML while cooling 8CB liquid crystal in presence of magnetic field $B = 7$ T, subjected to homeotropic anchoring at the glass surface $z = 0$ (see Fig. 6.2). The photograph (here is a small part of it) is taken in the xy-plane close to the glass surface. The black regions correspond to the orientation of molecules along the $x \pm \delta x$-direction, and white regions are all other possible directions.

3. In the vicinity of the nematic–smectic transition ($T \simeq 32.5$°C) the formation of stripes close to the glass surface was observed.

4. While further cooling, a doubly-periodic pattern in the xy-plane developed (see Fig. 6.3), with periodicity of the stripes of about $10-20$ μm in the direction of $\mathbf{B}$ and of about 2 μm in the perpendicular direction.

The formation of periodic structures in 8CB smectic liquid crystals subjected to antagonistic boundary conditions was found before. However, the observed patterns where either stripes, described by edge dislocations and curvature walls [105, 106, 107], or very regular, almost hexagonal periodic patterns, described by focal conic defects [108, 109, 104] and toroidal defects [110, 111]. In this respect, the formation of a doubly periodic structure with two distinct periods (one almost ten times smaller than the other) observed in HFML is intriguing, unknown and unexplained.

Our hypothesis is that this doubly periodic structure occurs because of the competing effect of the magnetic field in the bulk and of the homeotropic anchoring at the glass surface, leading to frustration in the orientation of molecules (see Fig. 6.2). This frustration could be easily released in the nematic phase, by means of elastic distortions such as bend and splay (see Annotation 2.3). Indeed, experimentally no pattern was observed in the nematic phase. But for smectic layers, it is impossible to satisfy both requirements, namely in the bulk the layers should be perpendicular to the magnetic field with director $\mathbf{n} \parallel x$ and at the glass surface they should have $\mathbf{n} \parallel z$ (see Fig. 6.2). Note that here the director $\mathbf{n}$ follows the normal to the layer, because we consider the Sm-A phase. Although the layers can significantly deform, the curvature would alter the spacing between them, yielding an enormous compression energy. The only possible ground state of smectics is to have flat and uniformly-spaced layers, which cannot satisfy the imposed boundary conditions. The formation of the doubly-periodic pattern observed experimentally as in Fig. 6.3 is the manifestation of this frustration. Presumably, black and white regions are domains with different orientations of the molecules, which favour either the direction of the magnetic field or of the anchoring. Then the boundaries between two domains are topological defects associated with spontaneous symmetry breaking. However, the experimental picture does not allow us to identify unambiguously the director in every point of the photograph plane, resulting in more than one possible interpretation.

The aim of our theoretical study is to get insight into the 3D organization of smectic layers, given that in xy-plane close to the glass surface a doubly-periodic pattern occurs. The basic idea of our geometric approach is to conceive each smectic layer as a 2D regular surface. Space filling 3D structures of smectic layers can be constructed by adding the surfaces/layers on top of each other, similar to russian ‘matryoshkas’. Since the thickness of the layer $d = 3.2$ nm is much smaller than the characteristic length scale of the observed structure, of the order of microns, we can apply a coarse-graining approach, by representing every surface as a stack of several molecular layers.

6.2 Act I: a simple 2D model

We begin our considerations with a simple coarse-grained 2D model. We assume that the smectic layers are curved in the xz-plane as superellipses in order to satisfy boundary conditions (see Fig. 6.4). Indeed, the orientation of the molecules, described by the normal to the superellipses, changes from parallel to the magnetic field in the bulk, to perpendicular to the magnetic field at the glass surface. Since the stacking of superellipses cannot tile a 2D plane, there are inevitable topological defects in the resulting space filling structure. These defects are *domain walls*, illustrated in Fig. 6.4 as vertical lines between the external superellipses, as well as *disclinations* of charge $+1/2$ (see Annotation 5.2). This structure extended in a third dimension (y direction) would give the experimentally observed stripes with periodicity $P_x \sim 10 \div 20$ μm. In this respect our geometry with superellipses is similar, but not identical, to those considered in references [106, 107]. Assuming this geometry we intend to find an optimum (minimum energy) configuration of superellipses, which is more stable than planar layers.

The optimum configuration and thus the optimum periodicity P_x is calculated as follows

1. We choose the rectangular box with dimensions $(2h_x \times 2h_z)$, where $2h_z = 1.6$ mm is the height of the experimental cell and we choose $h_x = h_z/4 = 200$ μm. Then we fill it with a set of superellipses parametrized as [3]

   $$\alpha_j(t) = (x_j(t), z_j(t)) = (a_j \cos^l t, c_j \sin^l t), \qquad t \in [0, \pi/2], \tag{6.1}$$

   where a_j and c_j are the semiaxes of the superellipse, and $l \leqslant 1$ is an exponent, which is the same for all superellipses. Index $j = 1$ labels the external superellipse

---

[3] This parametrization is identical to the 3D superspheroid considered in chapter 3 and given by Eq. (3.5).

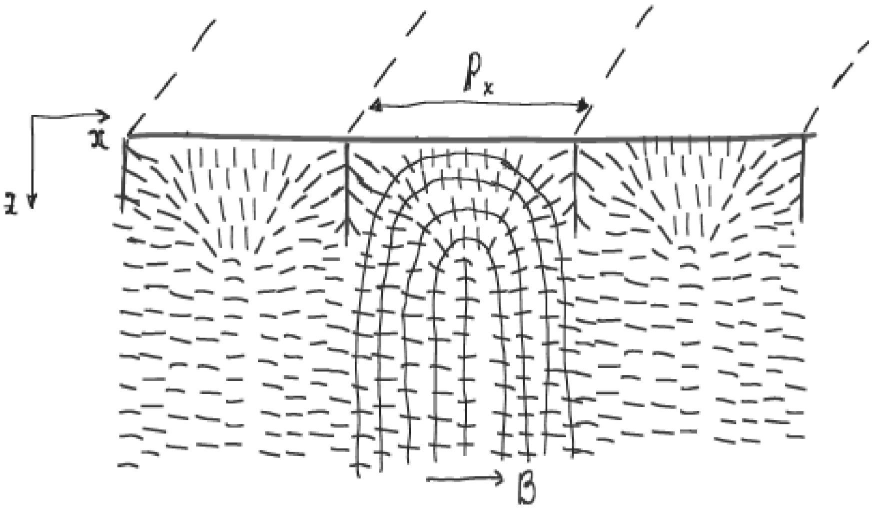

Figure 6.4: The illustration of smectic layers as a set of superellipses with molecules identified with the normal to the layer. The space filling structure fully satisfies the constraint in the bulk, where the molecules are aligned along the magnetic field B and partially at the glass surface, where the majority of the molecules are perpendicular. The structure contains $N = 3$ external superellipses and $j_{\rm max} = 4$ internal. For simplicity, we show only the upper half of the cell.

with $c_1 = h_z$, $a_1 = h_x/N$, where $N = 1,2,3,\ldots$ is a parameter. For the set of enclosed superellipses we have $c_{j+1} = c_j - d$ and $a_{j+1} = a_j - d$ with $d = 32$ nm the coarse-grained thickness and $j = 1,2,\ldots,\lfloor h_x/(Nd)\rfloor$.

2. For a given value of N we minimize the total free energy $\mathscr{F}_{\rm tot}(N,l)$ per unit length with respect to the exponent l

$$g(N;l_{\rm opt}) = \min_{N=\rm const}\left\{\mathscr{F}_{\rm tot}(l)/C(l)\right\}, \qquad \mathscr{F}_{\rm tot} = 4N(\mathscr{F}_{\rm el}+\mathscr{F}_{\rm mag}+\mathscr{F}_{\rm a}), \tag{6.2}$$

where $C(l) = 4N\sum_j \int\limits_0^{\pi/2} dt|\alpha'_j(t)|$ is the total length, and $\mathscr{F}_{\rm tot}$ is given by the sum of elastic energy $\mathscr{F}_{\rm el}$, magnetic energy $\mathscr{F}_{\rm mag}$ and the anchoring energy $\mathscr{F}_{\rm a}$. These energy contributions[4] can be easily estimated as

$$\mathscr{F}_{\rm el} = \frac{Kd}{2}\sum_j \int_0^{\pi/2} dt|\alpha'_j(t)|(2\kappa_j)^2, \qquad \kappa = \frac{x'z''-z'x''}{|\alpha'|^3}, \tag{6.3}$$

$$\mathscr{F}_{\rm mag} = -\frac{\Delta\chi B^2 d}{2\mu_0}\sum_j \int_0^{\pi/2} dt|\alpha'_j(t)|(n_{x,j})^2, \qquad n_x = -\frac{-z'}{|\alpha'|}, \tag{6.4}$$

$$\mathscr{F}_{\rm a} = \frac{W_a}{2}\sum_j \int_0^{\pi/2} dt|\alpha'_j(t)|\left[(n_{x,j})^2\big|_{z=0} + (n_{x,j})^2\big|_{z=2h_z}\right], \tag{6.5}$$

---

[4] The contribution from the curved domain walls is taken into account in the calculations, for derivation please consult the reference [107]. The energy term describing the compression of layers is omitted here, because of the vicinity to the nematic–smectic transition. This assumption is questionable.

Table 6.1: The calculated equilibrium values of periodicity P_x and exponent l define completely the geometry of the space filling structure for a given value of anchoring W_a. The small value of the exponent $l \approx 0.1$ means that the shape of superellipses is close to rectangular.

W_a, 10^{-4} J/m^2	1	5	10	30	50
P_x, μm	15	17	19	29	38
l_{opt}	0.30	0.15	0.09	0.07	0.05

where $|\alpha'_j(t)| = \sqrt{(x'_j(t))^2 + (z'_j(t))^2}$ is the length of the tangent vector of the parametrized curve $\alpha(t)$ (Eq. (6.1)) at t, and the index j is dropped from the definition of the curvature κ ($2\kappa = -\operatorname{div}\mathbf{n}$, see Eq. (2.15)) and the x-component of the normal n_x.

3. The optimal periodicity $P_x = 2h_x/N_{\text{opt}}$ (independent of the size of the box h_x) is found from $N_{\text{opt}} = \min g(N; l_{\text{opt}})$ given by Eq. (6.2). The result is presented in Table 6.1 for different values of the anchoring W_a.

The elastic splay constant (see Annotation 2.3, bend and twist are not allowed for smectic layers) for 8CB liquid crystal is $K_{11} = 1.1 \cdot 10^{-11}$ J/m [112], and a typical value of the magnetic susceptibility for liquid crystals is $\Delta\chi \simeq 10^{-7}$. However the value of the surface anchoring W_a in Eq. (6.5), which measures the energy cost required for deviations of the layer normal from the preferred z-direction, depends on the particular treatment of the surface and on the molecules. For the nematic phase $W_a \sim 10^{-7} \div 10^{-3}$ J/m^2 and for smectics it is much higher, $W_a \sim 10^{-3} \div 10^{-2}$ J/m^2, because it is more difficult to destroy the layered structure. It is intuitively clear, that there is a threshold value of W_a below which the planar configuration of the layers has lower free energy than the configuration with superellipses. Our calculations predict this critical value to be $W_a \approx 10^{-4}$ J/m^2.

To summarize briefly, the proposed 2D model, which captures the main physics of smectics, gives a reasonable estimate of the periodicity $P_x \simeq 15 \div 30$ μm along the magnetic field, similar to the one found in experiment. However, a generalization of this model to 3D would never predict the second periodicity, which is our main interest.

Elastic energy of smectics

Let us consider the elastic energy of smectics derived within a linear theory by Landau and Peierls in 1930, actually before the discovery of the smectic phase. It is given by the following form [104, 109]

$$\mathscr{F}_{\text{el}} = \frac{1}{2}\int dV \Big\{ \underbrace{C\,(\partial_z u)^2}_{\text{compression}} + \underbrace{K_{11}(\operatorname{div}\mathbf{n})^2}_{\text{bending}} \Big\}, \tag{6.6}$$

where C is the compression modulus and u is the layer displacement. The non-linear treatment of smectic elasticity is presented elsewhere, e.g. [113]. Both terms in Eq. (6.6) are important and should be taken into account while considering smectics in general and the nematic–smectic transition in particular. Nevertheless, there are two limiting cases, namely [109]

1. For the deep smectic phase $T < T_{\mathrm{N-Sm}}$ the typical value of elastic constants for 8CB is $C \approx 10^6$ J/m^3 and $K_{11} \approx 10^{-11}$ N, yielding

$$C \gg K_{11}/R^2 \quad \to \quad R \gg \lambda, \quad \lambda = \sqrt{\frac{K_{11}}{C}} \tag{6.7}$$

   where R is the characteristic length of the structure and $\lambda \approx 3$ nm is a 'penetration length'.

2. Close to the nematic–smectic transition $T \to T_{\mathrm{N-Sm}}$: the penetration length diverges $\lambda \to \infty$ and the compression modulus $C \to 0$, leading to the smallness of the compression term compared to the bending term. To guarantee the minimum of the free energy in Eq. (6.6) we require

$$2H \equiv -\operatorname{div}\mathbf{n} = 0 \quad \to \quad H \equiv 0 \quad \text{minimal surface,} \tag{6.8}$$

   whence smectic layers should be described by surfaces with vanishing mean curvature H, *minimal surfaces*, discussed in chapter 2 in the context of soap films as an area-minimizing surfaces (Eq. (2.38)).

6.3 Act II: Scherk's example of doubly periodic minimal surface

We assume that, because of the vanishing bending energy, minimal surfaces could be a good ansatz to describe the equilibrium properties of many systems, in particular the experimentally observed doubly-periodic pattern (see Fig. 6.3). To find the right minimal surface we need to satisfy the symmetries involved in experiment and the external boundary conditions. As an endeavour, we consider here the well-known example of doubly periodic minimal surface, called Scherk's first minimal surface[5]. This surface, composed of two sets of parallel planes connected by saddles (see Fig. 6.5) was used to describe the screw dislocations and twist grain boundaries in block copolymers [114] as well as in smectic-A liquid crystals [115]. It is given in Monge parametrization (see Annotation 2.2) as

$$h(x,y) \equiv z = \frac{1}{\sin\alpha}\log\frac{\cos x}{\cos(x\cos\alpha + y\sin\alpha)}, \qquad -\pi/2 < x, y < \pi/2, \tag{6.9}$$

where $\alpha \in (0, \pi/2]$ is a parameter (for $\alpha \to 0$ Eq. (6.9) reduces to helicoid). One can easily check, by substituting $h(x,y)$ into Eq. (2.31b), that the mean curvature vanishes at all the

---

[5] The first minimal surface after the catenoid and helicoid (Meusnier 1776), which was discovered by H. Scherk in 1834.

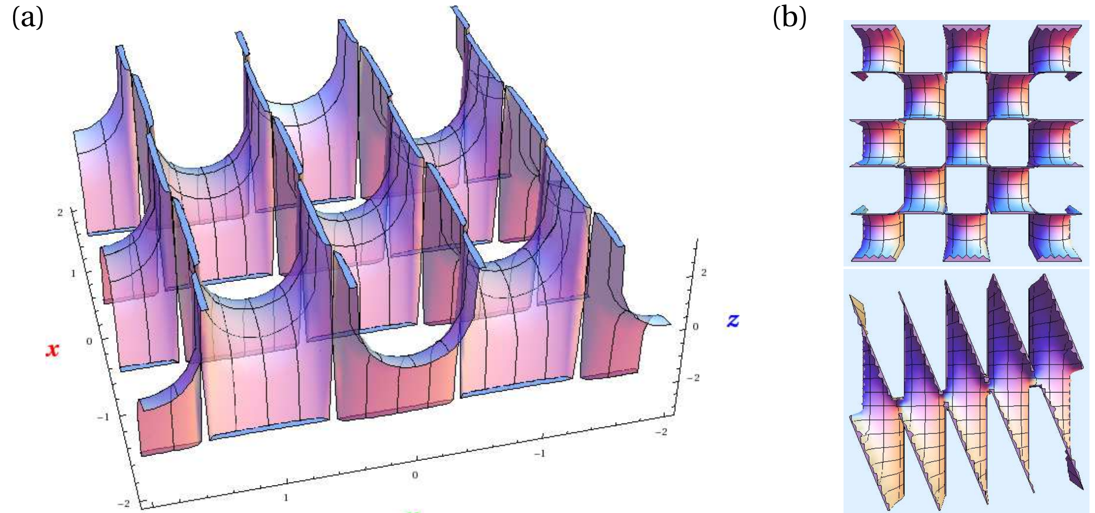

Figure 6.5: (a) The Scherk's minimal surface (Eq. 6.9) is composed of two sets of parallel planes connected by saddles. For illustration we have chosen $\alpha = \pi/2$. (b) Top view: the 'chess-board' for $\alpha = \pi/2$ and the rhombuses with side $\pi/\sin\alpha$ for $\alpha = \pi/8$. The ratio of the periods is $P_x/P_y = \tan(\alpha/2) < 1$.

points of this surface. At $z \to -\infty$ the set of parallel planes with spacing π have the normal $\mathbf{n} = (1,0,0)$ while at $z \to \infty$ the parallel planes with spacing π are perpendicular to $\mathbf{n} = (\cos\alpha, \sin\alpha, 0)$. At the grain boundary ($z = 0$ or $x = \pm(x\cos\alpha + y\sin\alpha)$) the structure is doubly periodic with one periodicity $P_x = \pi$ perpendicular to the planes and another one $P_y = \pi/\tan(\alpha/2)$. Since the structure is rotationally symmetric the ratio of these two periodicities $P_x/P_y = \tan(\alpha/2)$ does not depend on the chosen set of parallel planes ($z \leftrightarrow -z$).

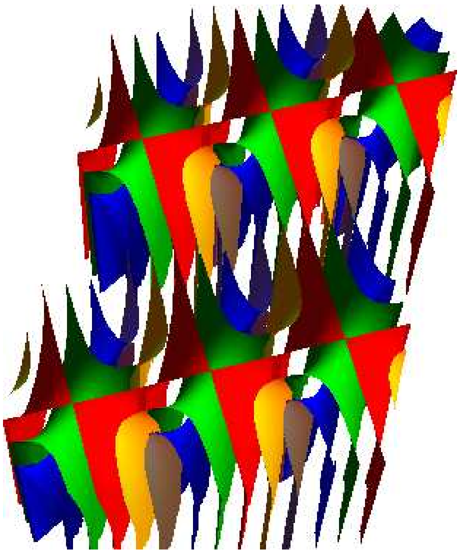

Figure 6.6: The space filling structure starting from the Sherk's minimal surface, red. The structure is composed of uniformly spaced layers with $\xi = +2, +1, -1, 2$ as gray, yellow, green and blue colors, respectively.

The Scherk's minimal surface describes a single layer of smectics with $H \equiv 0$ and negative Gaussian curvature $K < 0$. To be able to compare our model with the experimental observations we need to propose a space filling structure, like the one we did in 2D for superellipses. Starting from the minimal surface $\mathbf{x}_0 = (x, y, h(x,y))$ we translate each point along the normal $\mathbf{n}$ by a constant value a and find a set of evenly spaced layers parametrized by $\mathbf{x}_\xi = \mathbf{x}_0 + \xi a\mathbf{n}$ with $\xi = \pm1, \pm2, \ldots$ denoting the layer (see Fig. 6.6). Because of the symmetry only half of the Scherk's surface should be taken into account. Therefore the presented space filling structure is composed of a single set of parallel planes in the bulk, with magnetic field B being perpendicular to the planes, and the curved layers close to the glass surface at $z = 0$. However, the equal spacing between the layers leads to the curvature $\kappa_1(a) = 1/(R + a)$ and $\kappa_2(a) = 1/(-R + a)$ at the distance a from the minimal surface ($\kappa_1 = -\kappa_2 = 1/R$) [113]. The expressions for H, K (Eq. (2.13)) and area element dS (Eq. (2.37)) for the layer ξ are given by

$$H_\xi = \frac{a\xi K_0}{1 + a^2\xi^2 K_0}, \tag{6.10}$$

$$K_\xi = \frac{K_0}{1 + a^2\xi^2 K_0}, \tag{6.11}$$

$$dS_\xi = dS(1 + a^2\xi^2 K_0) \tag{6.12}$$

which means that non-zero Gaussian curvature $K_0 \neq 0$ of the minimal surface yields a non-zero mean curvature for any other layer ξ. Moreover at distance $\sqrt{-1/K_0}$ there is a curvature singularity, a defect, which should be treated separately [116][6]. In real situations, the competition between uniform spacing between the layers and the mean curvature (see Eq. (6.10) results in variable spacing between the layers. As was shown in [117] minimal surfaces, in particular triply periodic minimal surfaces, relax frustration between these two energy terms. Besides, we should not forget the saddle-splay term (see Annotation 2.3) which could be recast for layered structure into the integral over the Gaussian curvature $\bar{k}\iint dS\,K$ (Eq. (2.44)). For a certain range of material parameters, the favourable saddle-splay energy $\bar{k} > 0$ can stabilize the structures with $K < 0$ (minimal surfaces with defects) against the flat layers ($K \equiv 0$) as was demonstrated in [116] for the smectic blue phases.

We do not minimize the free energy here for the considered 3D structure, because the ratio of the periodicities parallel and perpendicular to the magnetic field $P_x/P_y < 1$ would always contradict the one experimentally found ($P_x/P_y \approx 5 \div 10$). To reconcile theory with experiment one should consider another minimal surface or to prove that minimal surfaces are not a good approximation.

6.4 Epilogue

Hopefully, I managed to convey the ‘beauty and mystery’ of liquid crystals and the advantages of using differential geometry. In two Acts we considered the space filling configuration of smectic layers described by i) superellipses with a positive K and ii) minimal surfaces with negative K. The ‘first actor’ ($K > 0$) was, in essence, a successful one, but not sufficient to explain the nature of the second periodicity. Therefore, the ‘second actor’ ($K < 0$) was introduced, which could easily explain the symmetry breaking in two directions, but again not correct enough to describe the experimentally observed equilibrium structure.

The question of the correct description of the observed doubly periodic pattern remains open. I think that minimal surfaces can be a powerful tool to shed light on the experimental observations and to generate the space filling structure with correct locations of

---

[6] From R. D. Kamien I have learned that smectics cannot have disclinations more than +1, but whatever minus sign.

topological defects. A recipe for solving this problem could be to start from the general *Weierstrass* representation of minimal surfaces [118]

$$x_1 = \Re \int_{z_0}^{z} dz\, e^{i\alpha} \frac{f(z)}{2} (1 - g(z))^2, \tag{6.13}$$

$$x_2 = \Re \int_{z_0}^{z} dz\, e^{i\alpha} \frac{i f(z)}{2} (1 + g(z))^2, \tag{6.14}$$

$$x_3 = \Re \int_{z_0}^{z} dz\, e^{i\alpha} f(z) g(z), \tag{6.15}$$

in terms of analytic function $f(z)$ and meromorphic function $g(z)$ and $\alpha \in [0;\pi/2]$. The Scherk's minimal surface is given by $f(z) = 4/(1 - z^4)$ and $g(z) = iz$. Another, more general, candidate of doubly periodic minimal surfaces that might be considered is a three parametric family of KMR (Karcher's, Meeks and Rosenberg's) examples $M_{\theta,\alpha,\beta}$ discussed in [119]. At this stage the author of the manuscript will provide a bottle of wine for suggestions of a simpler doubly periodic minimal surface which satisfies the experimental constraints.

Acknowledgements

I would like to thank Giorgia Tordini and Peter Christianen for introducing me to the problem of pattern formation in liquid crystals. It is a pleasure to acknowledge helpful conversations with Martine Ben Amar and Anne–Marie Cazabat. Finally I am grateful to Randall Kamien for his wonderful seminar "Geometry and topology of smectics" (Leiden, 16 April 2009) and for sharing his knowledge.

A Integrals over elliptic surface

In this appendix we derive the analytic expression of elastic energy and magnetic energy for deformed sphere. Although in chapter 3 we assumed a superspheroidal shape of deformed vesicle, it suffices in the limit of small deformations to describe a deformed sphere as a spheroid.

A.1 Oblate spheroid

A spheroid is the surface of revolution considered in Annotation 2.1 given by the following parametrization

$$\mathbf{x}(u,v) = \big(a\sin v\cos u,\, a\sin v\sin u,\, c\cos v\big), \qquad 0 \leqslant v \leqslant \pi, \quad 0 \leqslant u \leqslant 2\pi. \tag{A.1}$$

The area element for oblate spheroids ($a > c$) can be found by using Eqs. (2.7) and (2.24) and it is given by

$$\begin{aligned} dS = a\sin v\sqrt{a^2\cos^2 v + c^2\sin^2 v}\,du\,dv = \\ = a^2\sqrt{\Delta x^2 + (1-\Delta)}\,du\,dx = a^2\sqrt{\lambda}\,du\,dx, \end{aligned} \tag{A.2}$$

where the canonical variables are introduced

$$\boxed{\lambda = \Delta x^2 + (1-\Delta), \quad \Delta = 1 - \frac{c^2}{a^2} > 0, \quad x = \cos v, \quad -1 \leqslant x \leqslant 1.} \tag{A.3}$$

By using the coefficients of the II f.f. given by Eq. (2.25) we find the two principal curvatures of spheroid

$$\kappa_1 = \frac{c}{a\sqrt{a^2\cos^2 v + c^2\sin^2 v}} = \frac{\sqrt{1-\Delta}}{a\sqrt{\lambda}}, \tag{A.4a}$$

$$\kappa_2 = \frac{ac}{(a^2\cos^2 v + c^2\sin^2 v)^{3/2}} = \frac{\sqrt{1-\Delta}}{a\lambda^{3/2}}. \tag{A.4b}$$

Combining the above equations yields the mean curvature H and the Gaussian curvature K for a spheroid written as

$$H = \frac{\kappa_1+\kappa_2}{2} = \frac{\sqrt{1-\Delta}}{2a\sqrt{\lambda}}\left(1+\frac{1}{\lambda}\right), \tag{A.5}$$

$$K = \kappa_1\kappa_2 = \frac{1-\Delta}{a^2\lambda^2}, \tag{A.6}$$

Annotation A.1 Basic integrals

(i) $$\int_{-1}^{1} dx\sqrt{x^2+b^2} = \begin{bmatrix} x = b\sinh t, \\ \cosh^2 t = 1+\sinh^2 t \end{bmatrix} = b^2\int dt\cosh^2 t =$$

$$= \frac{b^2}{2}\int dt\,(\cosh 2t + 1) = \frac{b^2}{4}\sinh 2t + \frac{b^2}{2}t = \frac{b^2}{2}(\sinh t\cosh t + t) =$$

$$= \frac{b^2}{2}\left(\frac{x}{b}\sqrt{1+\frac{x^2}{b^2}} + \sinh^{-1}\frac{x}{b}\right) = \frac{1}{2}\left[x\sqrt{x^2+b^2} + b^2\ln\left(\frac{x}{b}+\sqrt{\frac{x^2}{b^2}+1}\right)\right]\Bigg|_{-1}^{1} =$$

$$= \sqrt{1+b^2} + \frac{b^2}{2}\ln\frac{1+\sqrt{1+b^2}}{-1+\sqrt{1+b^2}}. \tag{A.7}$$

(ii) $$\int_{-1}^{1} dx\frac{x^2}{\sqrt{x^2+b^2}} = \begin{bmatrix} x = b\sinh t, \\ \cosh^2 t = 1+\sinh^2 t \end{bmatrix} = b^2\int dt\sinh^2 t =$$

$$= \frac{b^2}{2}\int dt\,(\cosh 2t - 1) = \sqrt{1+b^2} - \frac{b^2}{2}\ln\frac{1+\sqrt{1+b^2}}{-1+\sqrt{1+b^2}}. \tag{A.8}$$

A.2 Surface area of spheroid

Direct integration of Eq. (A.2) yields the surface of a spheroid

$$S = 2\pi a^2\int_{-1}^{1} dx\sqrt{\lambda} = 2\pi a^2\sqrt{\Delta}\int_{-1}^{1} dx\sqrt{x^2+\frac{1-\Delta}{\Delta}} = 2\pi a^2\left(1+(1-\Delta)\frac{\tanh^{-1}\sqrt{\Delta}}{\sqrt{\Delta}}\right), \tag{A.9}$$

where $\tanh^{-1} x = \frac{1}{2}\ln\left(\frac{1+x}{1-x}\right)$. By introducing the ellipticity e and flattening f for oblate spheroid defined as following

$$e \equiv \sqrt{1-\frac{c^2}{a^2}}, \qquad f = 1-\sqrt{1-e^2}. \tag{A.10}$$

we can rewrite the surface area as

$$S = 2\pi a^2 + 2\pi c^2 \frac{\tanh^{-1} e}{e}. \tag{A.11}$$

In the limit $c \to a$ $(e \to 0)$ we recover the area of the sphere $S = 4\pi a^2$.

A.3 Measured birefringence

We start from the expression for birefringence, given by Eq. (3.4)

$$\Delta n = \frac{G}{2}\iint dS\left(1-3e_z^2\right), \tag{A.12}$$

where e_z is the z-component of the normal vector to the surface of the spheroid given by Eq. (2.23)

$$e_z = \frac{-a\cos v}{\sqrt{a^2\cos^2 v + c^2\sin^2 v}} = \frac{x}{\sqrt{\lambda}}. \tag{A.13}$$

Thus the second integral takes the form

$$\iint dS\, e_z^2 = 2\pi a^2 \int dx\,\sqrt{\lambda}\,\frac{x^2}{\lambda} = \frac{2\pi a^2}{\sqrt{\Delta}}\int dx\,\frac{x^2}{\sqrt{x^2+(1-\Delta)/\Delta}}, \tag{A.14}$$

which is the integral (ii) in Annotation A.1 with $b^2 = (1-\Delta)/\Delta$. Then, the final expression for birefringence is

$$\Delta n = \pi G\left[a^2 + c^2\frac{\tanh^{-1} e}{e} - \frac{3a^2}{a^2-c^2}\left(a^2 - c^2\frac{\tanh^{-1} e}{e}\right)\right]. \tag{A.15}$$

In the limit $a \to c$ $(e \to 0)$ we get $\Delta n = 0$, as expected for highly symmetric objects. We can check that the minimum (absolute maximum) value of the birefringence $\Delta n_{\max} = -2\pi G a^2$ is reached when $c = 0$ and thus the normalized birefringence is given by

$$\frac{\Delta n}{\Delta n_{\max}} = \frac{1}{2}\left(-1-\frac{c^2}{a^2}\frac{\tanh^{-1} e}{e} - \frac{3c^2}{a^2-c^2}\frac{\tanh^{-1} e}{e} + \frac{3a^2}{a^2-c^2}\right). \tag{A.16}$$

We are interested in the limit of small deformations of a sphere, i.e. $e \to 0$ or $\Delta \to 0$. Since $c^2 = a^2(1-\Delta)$ and $\tanh^{-1} e/e = 1 + \Delta/3 + \Delta^2/5 + \ldots$, we can rewrite Eq. (A.16) as

$$\begin{aligned}\frac{\Delta n}{\Delta n_{\max}} &= \frac{1}{2}\left[-1-\left(1+\frac{\Delta}{3}+\frac{\Delta^2}{5}\right)\left(-2-\Delta+\frac{3}{\Delta}\right)+\frac{3}{\Delta}\right] = \frac{8}{15}\Delta + \frac{11}{30}\Delta^2 \simeq \\ &\simeq \frac{16}{15}\frac{a-c}{R} + \frac{22}{15}\left(\frac{a-c}{R}\right)^2. \end{aligned} \tag{A.17}$$

The fact that the birefringence is linearly proportional to the deformation was known since the works of [62, 70] and thus our result coincides with this prediction.

A.4 Free energy terms

A.4.1 Magnetic term

The magnetic contribution to the free energy is given by

$$\mathcal{F}_{\mathrm{mag}} = -\frac{DB^2(\chi_\parallel - \chi_\perp)}{2\mu_0} \iint dS\, e_z^2. \tag{A.18}$$

where D is the thickness of layer and z labels the direction of the magnetic field B. After integration, which is the same as for the birefringence, we obtain

$$\mathcal{F}_{\mathrm{mag}} = -\frac{DB^2(\chi_\parallel - \chi_\perp)}{2\mu_0} \frac{2\pi a^2}{\Delta} \left(1 - (1-\Delta)\frac{\tanh^{-1}\sqrt{\Delta}}{\sqrt{\Delta}}\right). \tag{A.19}$$

A.4.2 Elastic terms

We start from the extended expression for the free energy proposed in [54]

$$\mathcal{F}_{\mathrm{el}} = \iint dS \{A'K + AH^2 + c_1 H^4 + c_2 H^2 K + c_3 K^2\}, \tag{A.20}$$

where $A, A', c_i = \{c_1, c_2, c_3\}$ are elastic constants. According to the Gauss–Bonnet theorem $\iint dSK = 4\pi$ (Eq. 2.34). Since we consider the deformations of vesicles without change of topology, we can neglect the first term in Eq. (A.20), which is a constant. By using Eqs. (A.5), (A.6), we can express the terms of elastic energy as polynoms of $1/\lambda$

$$H^2 = \frac{1-\Delta}{4a^2}\left(\frac{1}{\lambda} + 2\frac{1}{\lambda^2} + \frac{1}{\lambda^3}\right), \tag{A.21}$$

$$H^4 = \frac{(1-\Delta)^2}{16a^4}\left(\frac{1}{\lambda^2} + \frac{4}{\lambda^3} + \frac{6}{\lambda^4} + \frac{4}{\lambda^5} + \frac{1}{\lambda^6}\right), \tag{A.22}$$

$$H^2 K = \frac{(1-\Delta)^2}{4a^4}\left(\frac{1}{\lambda^3} + \frac{2}{\lambda^4} + \frac{1}{\lambda^5}\right), \tag{A.23}$$

$$K^2 = \frac{(1-\Delta)^2}{a^4}\frac{1}{\lambda^4}. \tag{A.24}$$

Then we introduce the function

$$\boxed{f(n) = \int_{-1}^{1} \frac{dx\sqrt{\lambda}}{\lambda^n}, \quad n \in \mathcal{N}}, \tag{A.25}$$

to express all integrals over surface in a compact form:

$$\mathcal{F}_A = A \cdot \frac{\pi}{2}(1-\Delta)\big(f(1) + 2f(2) + f(3)\big), \tag{A.26}$$

$$\mathcal{F}_{c_1} = c_1 \cdot \frac{\pi}{8a^2}(1-\Delta)^2\big(f(2) + 4f(3) + 6f(4) + 4f(5) + f(6)\big), \tag{A.27}$$

$$\mathcal{F}_{c_2} = c_2 \cdot \frac{\pi}{2a^2}(1-\Delta)^2\big(f(3) + 2f(4) + f(5)\big), \tag{A.28}$$

$$\mathcal{F}_{c_3} = c_3 \cdot \frac{2\pi}{a^2}(1-\Delta)^2 f(4). \tag{A.29}$$

The next step would be to calculate the integral Eq. (A.25) for $n \leqslant 6$, e.g. by using mathematica. We will choose another way (to exercise a bit in integration) and will derive a recursion relationship for $f(n)$, starting from

$$f(n) = \int_{-1}^{1} \frac{dx}{\lambda^{n-1/2}} = \int_{-1}^{1} \frac{dx}{\Delta^{n-1/2}(x^2+(1-\Delta)/\Delta)^{n-1/2}} = \begin{bmatrix} x = b\sinh t, \\ b^2 = \dfrac{1-\Delta}{\Delta} \end{bmatrix} =$$
$$= \int \frac{dt\, b\cosh t}{\Delta^{n-1/2} b^{2n-1} (\cosh t)^{2n-1}} = \frac{1}{\sqrt{\Delta}(1-\Delta)^{n-1}} \int \frac{dt}{(\cosh t)^{2n-2}} =$$
$$\underline{= \frac{1}{\sqrt{\Delta}(1-\Delta)^{n-1}} I(2n-2).} \tag{A.30}$$

Then we can show that

$$I(2n-2) = \int \frac{dt}{(\cosh t)^{2n-2}} = \int \frac{d\sinh t}{(\cosh t)^{2n-1}} = \frac{\sinh t}{(\cosh t)^{2n-1}} + (2n-1)\int \frac{\sinh^2 t}{\cosh^{2n} t} =$$
$$= \frac{\sinh t}{(\cosh t)^{2n-1}} + (2n-1)\int \frac{dt}{(\cosh t)^{2n-2}} - (2n-1)\int \frac{dt}{\cosh^{2n} t} \quad \rightarrow$$
$$\rightarrow \quad \int \frac{dt}{\cosh^{2n} t} = \frac{1}{2n-1} \frac{\sinh t}{(\cosh t)^{2n-1}}\bigg|_{-1}^{1} + \frac{2n-2}{2n-1}\int \frac{dt}{(\cosh t)^{2n-2}}. \tag{A.31}$$

Coming back to our natural variables we get

$$\frac{\sinh t}{\cosh^{2n-1} t}\bigg|_{-1}^{1} = \frac{2}{b} \cdot \frac{b^{2n-1}}{(1+b^2)^{n-1/2}} = 2\sqrt{\Delta}(1-\Delta)^{n-1}. \tag{A.32}$$

Substituting it into Eq. (A.31) we obtain a recursion relationsip for $I(2n)$ as

$$\boxed{I(2n) = \frac{2\sqrt{\Delta}(1-\Delta)^{n-1}}{(2n-1)} + \frac{2n-2}{2n-1} I(2n-2).} \tag{A.33}$$

and accordingly for $f(n+1)$ as follows

$$\underline{f(n+1)} = \frac{I(2n)}{\sqrt{\Delta}(1-\Delta)^{n}} = \underline{\frac{2}{(2n-1)(1-\Delta)}\big(1+(n-1)f(n)\big).} \tag{A.34}$$

►

$$f(1) = \frac{1}{\sqrt{\Delta}}\int dt = \frac{1}{\sqrt{\Delta}} \sinh^{-1}\frac{x}{b}\bigg|_{-1}^{1} = \frac{1}{\sqrt{\Delta}} \ln\left(\frac{x}{b} + \sqrt{1+\frac{x^2}{b^2}}\right)\bigg|_{-1}^{1} = 2\frac{\tanh^{-1}\sqrt{\Delta}}{\sqrt{\Delta}}.$$

In the limit $c \rightarrow a, \Delta \rightarrow 0$, $f(1) \rightarrow 2$ (useful to avoid computational divergence).

Other terms (in fact $\forall n$) are easy to calculate using Eq. (A.34)

► for $n = 1$

$$f(2) = \frac{2}{(1-\Delta)},$$

- for $n = 2$
$$f(3) = \frac{2}{3(1-\Delta)}\big(1 + f(2)\big),$$
- for $n = 3$
$$f(4) = \frac{2}{5(1-\Delta)}\big(1 + 2f(3)\big),$$
- for $n = 4$
$$f(5) = \frac{2}{7(1-\Delta)}\big(1 + 3f(4)\big),$$
- for $n = 5$
$$f(6) = \frac{2}{9(1-\Delta)}\big(1 + 4f(5)\big).$$

By substitution the explicit expressions of $f(n)$ into Eqs. (A.26)–(A.29) we get all the terms of elastic energy $\mathscr{F}_{\mathrm{el}}$ as a function of the deformation Δ.

A.5 Expansion within Helfrich model

In this section, we take into account only the quadratic term of $\mathscr{F}_{\mathrm{el}}$ or the bending energy term proposed by Helfrich [53]. Within this approach, when $\mathscr{F}_{\mathrm{el}} = \mathscr{F}_A$, we aim at finding the condition of equilibrium for spherical vesicles in presence of magnetic fields, by reproducing the result [62]. Equilibrium corresponds to the minimum (in this context extremum since we do not consider the second variation) of the total free energy

$$\frac{\partial(\mathscr{F}_{\mathrm{el}} + \mathscr{F}_{\mathrm{mag}})}{\partial\Delta} = 0 \quad \text{or} \quad \frac{\partial\mathscr{F}_{\mathrm{el}}}{\partial\Delta} = -\frac{\mathscr{F}_{\mathrm{mag}}}{\partial\Delta}. \tag{A.35}$$

In the following we expand the expressions for $\mathscr{F}_A$ and $\mathscr{F}_{\mathrm{mag}}$ given by Eqs. (A.26) and (A.19) correspondingly in $\Delta \ll 1$. First we expand Eq (A.26) as

$$\begin{aligned}\mathscr{F}_A &= A\pi(1-\Delta)\Big[\frac{\tanh^{-1}\sqrt{\Delta}}{\sqrt{\Delta}} + \frac{2}{1-\Delta} + \frac{1}{3(1-\Delta)}\Big(1 + \frac{2}{1-\Delta}\Big)\Big] = \\ &= A\pi\Big[(1-\Delta)\Big(1 + \frac{1}{3}\Delta + \frac{1}{5}\Delta^2\Big) + \frac{7}{3} + \frac{2}{3}(1 + \Delta + \Delta^2)\Big] = \underline{A\cdot 4\pi\Big[1 + \frac{2}{15}\Delta^2\Big]}.\end{aligned} \tag{A.36}$$

This expression coincides with the one obtained in [62] for the case of zero spontaneous curvature

$$E_c = 8\pi k + \frac{48}{5}\pi k\frac{s_2^2}{r_0} = \left[\begin{array}{l} s_2 = -2(a-c)/3 \simeq -R\Delta/3, \\ A = 2k,\ \Big(\dfrac{\partial n_x}{\partial x} + \dfrac{\partial n_y}{\partial y}\Big) = -2H \end{array}\right] = \pi A\Big(4 + \frac{8}{15}\Delta^2\Big). \tag{A.37}$$

Next we expand the magnetic energy, assuming the condition of constant surface, as follows:

1. The condition of constant surface follows from Eq. (A.11):
$$S = \pi a^2\Big(1 + (1-\Delta)\frac{\tanh^{-1}\sqrt{\Delta}}{\sqrt{\Delta}}\Big) \quad\rightarrow\quad 4\pi R^2 = 2\pi a^2 + 2\pi a^2(1-\Delta)\Big(1 + \frac{1}{3}\Delta + \frac{1}{5}\Delta^2\Big),$$
$$R^2 = a^2\Big(1 - \frac{1}{3}\Delta - \frac{1}{15}\Delta^2\Big) \quad\rightarrow\quad a^2 = R^2\Big(1 + \frac{1}{3}\Delta + \frac{8}{45}\Delta^2\Big). \tag{A.38}$$
2. For $\Delta \ll 1$ we expand the magnetic energy (Eq. (A.19)) as
$$\mathscr{F}_{\text{mag}} = -2\delta a^2\Big[\frac{1}{\Delta} - \frac{1-\Delta}{\Delta}\Big(1 + \frac{1}{3}\Delta + \frac{1}{5}\Delta^2\Big)\Big] = -4\delta a^2\Big(\frac{1}{3} + \frac{1}{15}\Delta\Big), \tag{A.39}$$
where $\delta = \pi D B^2(\chi_\parallel - \chi_\perp)/(2\mu_0)$ was introduced.
3. Taking into account condition Eq. (A.38) we find
$$\mathscr{F}_{\text{mag}} = -4\delta R^2\Big(1 + \frac{1}{3}\Delta\Big)\cdot\Big(\frac{1}{3} + \frac{1}{15}\Delta\Big) = -4\delta R^2\Big(\frac{1}{3} + \frac{8}{45}\Delta\Big), \tag{A.40}$$
which coincides with the result in [62].

Finally, taking the derivatives of Eqs. (A.36) and (A.40) with respect to Δ and substituting the result into Eq. (A.35), we find the condition of equilibrium as
$$\frac{16}{15}\pi A\Delta = \frac{32}{45}\delta R^2, \qquad \Delta = \frac{a^2 - c^2}{a^2} \simeq \frac{2(a-c)}{R}, \tag{A.41}$$
or rewriting
$$\boxed{\frac{a-c}{R} = B^2\frac{R^2 D(\chi_\parallel - \chi_\perp)}{6A\mu_0}}. \tag{A.42}$$

A.6 Relationship between A and c_i

In the previous section we have considered a harmonic approximation of $\mathscr{F}_{\text{el}}$ with $A > 0$. As was suggested in [54] the coefficient A can be negative and thus higher order terms with c_i are required to stabilize the free energy. To guarantee the stability of a sphere against small deformations we require the lowest term in $\mathscr{F}_{\text{el}}$ to be quadratic in Δ with positive coefficient (Hooke's law). Therefore, the coefficients A and c_i cannot be independent in order to satisfy this condition. Here we find their relationship, by expanding Eqs. (A.26)–(A.29) for small deformations $\Delta \ll 1$, assuming the condition of constant surface.

We start by expanding the last term in $\mathscr{F}_{\text{el}}$, by rewriting Eq. (A.29)
$$\begin{aligned}\mathscr{F}_{c_3} &= c_3\cdot\frac{2\pi}{a^2}(1-\Delta)^2\Big\{\frac{2}{5(1-\Delta)} + \frac{8}{15(1-\Delta)^2} + \frac{16}{15(1-\Delta)^3}\Big\} = \\ &= c_3\cdot\frac{2\pi}{a^2}\Big[\frac{2}{5} - \frac{2}{5}\Delta + \frac{8}{15} + \frac{16}{15}(1 + \Delta + \Delta^2)\Big] \overset{\text{Eq. (A.38)}}{=} \\ &= c_3\cdot\frac{2\pi}{R^2}\Big(1 - \frac{1}{3}\Delta - \frac{1}{15}\Delta^2\Big)\cdot\Big(2 + \frac{2}{3}\Delta + \frac{16}{15}\Delta^2\Big) = \underline{c_3\cdot\frac{4\pi}{R^2}\Big(1 + \frac{16}{45}\Delta^2\Big)}.\end{aligned} \tag{A.43}$$

Then the c_2-term given by Eq. (A.28) can be split into

$$\mathscr{F}_{c_2} = \frac{c_2}{2c_3}\mathscr{F}_{c_3} + c_2 \cdot \frac{\pi}{2a^2}(1-\Delta)^2\big[f(3)+f(5)\big]. \tag{A.44}$$

The first term is already calculated (Eq. (A.43) and the last term is expanded as follows

$$\begin{aligned}
&\frac{\pi}{2a^2}\Big[\frac{2}{3}(1-\Delta)+\frac{4}{3}+\frac{2}{7}(1-\Delta)+\frac{12}{35}+\frac{16}{35(1-\Delta)}+\frac{32}{35(1-\Delta)^2}\Big] = \\
&\qquad = \frac{\pi}{2a^2}\Big[\frac{92}{35}-\frac{20}{21}\Delta+\frac{16}{35}(1+\Delta+\Delta^2)+\frac{32}{35}(1+2\Delta+3\Delta^2)\Big] = \\
&\qquad = \frac{\pi}{2R^2}\Big(1-\frac{1}{3}\Delta-\frac{1}{15}\Delta^2\Big)\cdot\Big(4+\frac{4}{3}\Delta+\frac{16}{5}\Delta^2\Big) = \frac{2\pi}{R^2}\Big(1+\frac{28}{45}\Delta^2\Big),
\end{aligned} \tag{A.45}$$

and Eq. (A.44) takes the form

$$\mathscr{F}_{c_2} = c_2\frac{2\pi}{R^2}\Big(1+\frac{16}{45}\Delta^2+1+\frac{28}{45}\Delta^2\Big) = \underline{c_2\cdot\frac{4\pi}{R^2}\Big(1+\frac{22}{45}\Delta^2\Big)}. \tag{A.46}$$

The same procedure (splitting into 'known' and 'unknown') can be done for the c_1-term (Eq. (A.27)), expressed as

$$\mathscr{F}_{c_1} = \frac{c_1}{c_3}\frac{3}{8}\mathscr{F}_{c_3} + c_1\cdot\frac{\pi}{2a^2}(1-\Delta)^2\big[f(3)+f(5)\big] + c_1\cdot\frac{\pi}{8a^2}(1-\Delta)^2\big[f(2)+f(6)\big]. \tag{A.47}$$

The expansion in Δ of the last term is given as

$$\begin{aligned}
&\frac{\pi}{8a^2}\Big[2(1-\Delta)+\frac{2}{9}(1-\Delta)+\frac{2}{9}\cdot\frac{8}{7}+\frac{2}{9}\cdot\frac{8}{7}\cdot\frac{6}{5(1-\Delta)}+\frac{2}{9}\cdot\frac{8}{7}\cdot\frac{6}{5}\cdot\frac{4}{3(1-\Delta)^2}+\frac{2}{9}\cdot\frac{8}{7}\cdot\frac{6}{5}\cdot\frac{4}{3}\frac{2}{(1-\Delta)^3}\Big] = \\
&\quad = \frac{\pi}{8a^2}\Big[\frac{20}{9}-\frac{20}{9}\Delta+\frac{16}{63}+\frac{32}{105}(1+\Delta+\Delta^2)+\frac{128}{315}(1+2\Delta+3\Delta^2)+\frac{256}{315}(1+3\Delta+6\Delta^2)\Big] = \\
&= \frac{\pi}{8a^2}\Big[4+\frac{4}{3}\Delta+\frac{32}{45}\Delta^2\Big] = \frac{\pi}{2R^2}\Big(1-\frac{1}{3}\Delta-\frac{1}{15}\Delta^2\Big)\cdot\Big(1+\frac{1}{3}\Delta+\frac{8}{5}\Delta^2\Big) = \frac{\pi}{2R^2}\Big(1+\frac{64}{45}\Delta^2\Big).
\end{aligned} \tag{A.48}$$

Substituting Eqs. (A.43), (A.45), (A.48) into Eq. (A.47) gives

$$\mathscr{F}_{c_1} = c_1\cdot\frac{4\pi}{R^2}\Big[\frac{3}{8}\Big(1+\frac{16}{45}\Delta^2+\frac{1}{2}\Big(1+\frac{28}{45}\Delta^2+\frac{1}{8}\Big(1+\frac{64}{45}\Delta^2\Big)\Big)\Big] = \underline{c_1\cdot\frac{4\pi}{R^2}\Big[1+\frac{28}{45}\Delta^2\Big]}. \tag{A.49}$$

Combining all the 'underlined' results we can write the expansion of elastic free energy up to the second order in Δ as

$$\mathscr{F}_{\mathrm{el}} = \underbrace{4\pi\Big(A+\frac{c_1+c_2+c_3}{R^2}\Big)}_{\text{sphere}} + \frac{8\pi}{45}\Delta^2\underbrace{\Big(2A+\frac{14c_1+11c_2+8c_3}{R^2}\Big)}_{>0}. \tag{A.50}$$

Comparing the second term with the harmonic approximation (Eq. (A.36)) we find the relationship between the Helfrich model ($A = 2k$, $c_1 = c_2 = c_3 = 0$) and the spontaneous bending model

$$\boxed{2k = A + \frac{14c_1+11c_2+8c_3}{3R^2}}, \tag{A.51}$$

which also serves as condition of stability of a sphere agains small deformations, given that $k > 0$.

B

Variation of free energy around the sphere

In chapter 3 we considered spherical vesicles, assuming that the sphere is a stable solution of the extended form of elastic free energy

$$\mathscr{F}_{\text{el}} = \iint dS\,\{A'K + AH^2 + c_1H^4 + c_2H^2K + c_3K^2\}. \tag{B.1}$$

To check this hypothesis we study the variation of the free energy Eq. (B.1) around the sphere. The necessary, but not sufficient, condition for equilibrium is the vanishing of the first variation. When we discussed soap films in chapter 2 we have calculated the variation of the surface area dS by displacing the surface with parametrization $\mathbf{x}(u,v)$ along the normal $\mathbf{n}(u,v)$ by $a(u,v)$. We found that up to the first order in a the variation is proportional to the mean curvature $\delta dS = 2aH$ (Eq. (2.38)). Similarly, we can express the variation of mean curvature H and Gaussian curvature K when a surface is displaced along the normal by a [120, 121]

$$\delta H = (K - 2H^2)a - \frac{1}{2}g^{ij}\nabla_i\nabla_j a, \tag{B.2}$$

$$\delta K = -2KHa - \tilde{\kappa}^{ij}\nabla_i\nabla_j a, \tag{B.3}$$

where ∇_i is a covariant derivative, $\tilde{\kappa}^{ij} \equiv \epsilon^{ik}\epsilon^{jl}\kappa_{kl}/|g|$, where $\epsilon^{ij} = \epsilon_{ij} = \begin{pmatrix} 0 & 1 \\ -1 & 0 \end{pmatrix}$ is the completely antisymmetric tensor.

The metric tensor $g_{ij} = \partial_i\mathbf{x}\cdot\partial_j\mathbf{x}$ and the curvature tensor $\kappa_{ij} = -\mathbf{n}\cdot\partial_i\partial_j\mathbf{x}$ (see chapter 2 for details) take a simple form for a sphere with $R \equiv 1$

$$g_{ij} = \begin{pmatrix} E & F \\ F & G \end{pmatrix} = \begin{pmatrix} \sin^2 v & 0 \\ 0 & 1 \end{pmatrix}, \qquad \kappa_{ij} = \begin{pmatrix} \kappa_1 & 0 \\ 0 & \kappa_2 \end{pmatrix} = \delta_{ij}. \tag{B.4}$$

Substituting this result into $\tilde{\kappa}^{ij}$ we find

$$\tilde{\kappa}^{ij} = \epsilon^{ik}\epsilon^{jl}\frac{\delta_{kl}}{\sin^2 v} = -\frac{\epsilon^{ik}\epsilon^{kj}}{\sin^2 v} = -\frac{\delta^{ij}}{\sin^2 v}, \tag{B.5}$$

and consequently the variation of Gaussian curvature (Eq. B.3) takes the form (for a sphere $H = 1/R = 1$, $K = 1/R^2 = 1$)

$$\delta K = -2a + \frac{\delta^{ij}\nabla_i\nabla_j a}{\sin^2 v} = -2a + \frac{\nabla^2 a}{\sin^2 v}. \tag{B.6}$$

The last term contains the Laplace–Beltrami operator defined as

$$\boxed{\nabla^2 = \nabla_i\nabla^i = \frac{1}{\sqrt{|g|}}\partial_i\big(g^{ij}\sqrt{|g|}\partial_i\big)}, \tag{B.7}$$

which is the generalization of the Laplacian, used for the flat Euclidean metric, towards an arbitrary Riemannian metric. For a sphere we have $\sqrt{|g|} = \sin v$ and the inverse of the metric tensor is

$$g^{ij} = (g_{kl})^{-1}_{ij} = \frac{1}{\sin^2 v}\begin{pmatrix}1 & 0\\ 0 & \sin^2 v\end{pmatrix}. \tag{B.8}$$

Substituting this result into Eq. (B.7) we find the Laplace–Beltrami operator for a sphere

$$\nabla^2 = \frac{1}{\sin v}\partial_i\left(\frac{1}{\sin v}\begin{pmatrix}1 & 0\\ 0 & \sin^2 v\end{pmatrix}\partial_i\right) = \frac{1}{\sin^2 v}\partial_{uu} + \frac{1}{\sin v}\partial_v(\sin v\,\partial_v), \tag{B.9}$$

and the explicit expression of the variation of the Gaussian curvature (Eq. (B.6)).

Let us consider the covariant derivatives of:

scalar $\quad \nabla_i a = \partial_i a,$ (B.10)

vector $\quad \nabla_l V^m = \partial_l V^m + \Gamma^m_{kl}V^k,$ (B.11)

covector $\quad \nabla_l \omega_m = \partial_l \omega_m - \Gamma^k_{lm}\omega_k,$ (B.12)

tensor $\quad \nabla_l A^{ik} = \partial_l A^{ik} + \Gamma^i_{ml}A^{mk} + \Gamma^k_{ml}A^{im},$ (B.13)

where Γ^k_{ij} is called affine connection [47] or Christoffel symbol [45]. For the surface of revolution parametrized by (see Annotation 2.1) $\mathbf{x}(u,v) = \big(f(v)\cos u, f(v)\sin u, g(v)\big)$, the Christoffel symbols are [45]

$$\Gamma^1_{11} = 0, \qquad \Gamma^2_{11} = -\frac{ff'}{(f')^2 + (g')^2}, \qquad \Gamma^1_{12} = \frac{ff'}{f^2}, \tag{B.14}$$

$$\Gamma^2_{12} = 0, \qquad \Gamma^1_{22} = 0, \qquad \Gamma^2_{22} = \frac{f'f'' + g'g''}{(f')^2 + (g')^2}. \tag{B.15}$$

Substituting $f(v) = \sin v$ and $g(v) = \cos v$ into Eqs. (B.14), (B.15) we find the Christoffel symbols for a sphere as follows

$$\Gamma^1_{11} = \Gamma^2_{12} = \Gamma^1_{22} = 0, \quad \Gamma^2_{11} = -\sin v\cos v, \quad \Gamma^1_{12} = \cot v, \quad \Gamma^2_{22} = 0. \tag{B.16}$$

The second term of the mean curvature variation δH (Eq. (B.2)) around sphere reads as

$$\begin{aligned} g^{ij}\nabla_i\nabla_j a = g^{ij}\nabla_i\partial_j a = g^{ij}\big(\partial_i\partial_j a - \Gamma^k_{ij}\partial_k a\big) &\overset{\text{Eq. (B.8)}}{=} \\ = \frac{1}{\sin^2 v}(\partial_u^2 a - \Gamma^k_{uu}\partial_k a) + (\partial_v^2 a - \Gamma^k_{vv}\partial_k a) &\overset{\text{Eq. (B.16)}}{=} \\ = \frac{1}{\sin^2 v}\partial_u^2 a + \frac{\cos v}{\sin v}\partial_v a + \partial_v^2 a \equiv \hat{L}_1 a. & \end{aligned} \tag{B.17}$$

Combining this result with the first term $H^2 = K = 1$ for sphere we find

$$\underline{\delta H = -a - \frac{1}{2}\hat{L}_1 a.} \tag{B.18}$$

Similarly, we wrtite the variation of the Gaussian curvature (Eq. (B.6)) in a compact form as

$$\underline{\delta K = -2a + \hat{L}_2 a,} \qquad \hat{L}_2 = \frac{1}{\sin^4 v}\partial_{uu} + \frac{1}{\sin^3 v}\partial_v(\sin v\,\partial_v). \tag{B.19}$$

Based on the knowledge of $\delta H, \delta K$ (and $\delta dS = 2aH$) we find the variation of $\mathscr{F}_{\rm el}$ (Eq. (B.1)) as the sum of the following terms

$$A': \qquad \delta \iint dS K = \iint dS(2aHK + \delta K) = \iint dS \hat{L}_2 a, \tag{B.20}$$

$$A: \qquad \delta \iint dS H^2 = \iint dS(2aH^3 + 2H\delta H) = -\iint dS \hat{L}_1 a, \tag{B.21}$$

$$c_3: \qquad \delta \iint dS K^2 = \iint dS(2aHK^2 + 2K\delta K) = \iint dS(-2a + 2\hat{L}_2 a), \tag{B.22}$$

$$c_1: \qquad \delta \iint dS H^4 = \iint dS(2aH^5 + 4H^3\delta H) = \iint dS(-2a - 2\hat{L}_1 a), \tag{B.23}$$

$$\begin{aligned} c_2: \qquad \delta \iint dS H^2 K &= \iint dS(2aH^3 K + 2HK\delta H + H^2\delta K) = \\ &= \iint dS(-2a + \hat{L}_2 a - \hat{L}_1 a). \end{aligned} \tag{B.24}$$

Combining these terms we get

$$\delta\mathscr{F}_{\rm el} = \iint dS\big\{-2(c_1 + c_2 + c_3)a - (A + 2c_1 + c_2)\hat{L}_1 a + (A' + c_2 + 2c_3)\hat{L}_2 a\big\}. \tag{B.25}$$

Assuming that the topology does not change $\delta \iint dS K = 0 \to \hat{L}_2 a = 0$ we can neglect the last term. For $a = \text{const}$ the first variation vanishes if $c_1 + c_2 + c_3 = 0$. In the case of $a \neq \text{const}$ one needs to solve partial differential equations, which is beyond the scope of this thesis. Interestingly, we can recover the same condition $c_1 + c_2 + c_3 = 0$ for the stability of sphere ($H^2 = K = 1/R^2$) from the equilibrium shape equation Eq. (2.52).

C

Green's function on a sphere

In general, the problem of finding the Green's function is equivalent to the problem of finding the set of eigenvectors for the operator $\hat{L}$, such as $\hat{L}\Psi = -\lambda\Psi$. Then the Green's function is defined as

$$\Gamma(\mathbf{x},\mathbf{y}) = \sum_{\lambda\neq 0} \frac{\Psi_\lambda(\mathbf{x})\Psi^*_\lambda(\mathbf{y})}{\lambda}. \tag{C.1}$$

Note that not every operator $\hat{L}$ has the Green's function $\Gamma(\mathbf{x},\mathbf{y})$ or inverse of $\hat{L}$.

Here we aim at finding the Green's function for the Laplace–Beltrami operator $\hat{L} = \nabla^2$ on unit sphere defined as (see also Eq. (B.7))

$$\nabla^2 = \frac{1}{\sin^2\theta}\partial_{\phi\phi} + \frac{1}{\sin\theta}\partial_\theta\big(\sin\theta\,\partial_\theta\big), \tag{C.2}$$

where θ is a polar angle and ϕ is an azimuthal angle. Accordingly, we aim at solving the eigenvector problem for the following equation

$$\nabla^2\Psi + \lambda\Psi = 0. \tag{C.3}$$

By applying the separation of variables for $\Psi(\phi,\theta) = \Phi(\phi)\cdot\Theta(\theta)$ we get

$$\frac{\Phi''}{\Phi} = -\frac{\frac{1}{\sin\theta}\partial_\theta\big(\sin\theta\,\Theta'_\theta\big) + \lambda\Theta}{\frac{1}{\sin^2\theta}\Theta} \equiv -m^2. \tag{C.4}$$

The solution for Φ is $\Phi(\phi) \propto \cos(m\phi)$ or $\sin(m\phi)$, and for Θ we rewrite the second equality as

$$\frac{1}{\sin\theta}\partial_\theta\big(\sin\theta\Theta'_\theta\big) + \Big(\lambda - \frac{m^2}{\sin^2\theta}\Big)\Theta = 0, \tag{C.5}$$

which is known as Legendre equation written in canonical form as

$$\big((1-x^2)y'\big)' + \Big(l(l+1) - \frac{m^2}{1-x^2}\Big)y = 0, \tag{C.6}$$

where $x = \cos\theta$ and $\lambda = l(l+1)$. The solutions for this equation are called associated Legendre polynomials $P_l^m(\cos\theta)$, which allows us to express Ψ as

$$\Psi(\theta,\phi) = \begin{array}{c} P_l^m(\cos\theta)\cdot\cos(m\phi) \\ \text{or} \\ P_l^m(\cos\theta)\cdot\sin(m\phi) \end{array} \qquad 0 \leqslant m \leqslant l. \tag{C.7}$$

The associated Legendre polynomials for negative m are

$$P_l^{-m}(x) = (-1)^m \frac{(l-m)!}{(l+m)!} P_l^m(x). \tag{C.8}$$

Since $\forall l$ there are $2l+1$ functions orthogonal both in l and m, we can write the solution for $\Psi(\theta,\phi)$ in spherical harmonics $Y_{l,m}$, given by

$$\Psi(\theta,\phi) = Y_{l,m}(\theta,\phi) = \sqrt{\frac{(2l+1)(l-m)!}{4\pi(l+m)!}} P_l^m(\cos\theta) e^{im\phi}, \qquad -l \leqslant m \leqslant l, \tag{C.9}$$

which are orthonormal

$$\int_{\theta=0}^{\pi} \int_{\phi=0}^{2\pi} d\Omega\, Y_{l,m} Y^*_{l',m'} = \delta_{ll'}\delta_{mm'}, \qquad Y^*_{l,m}(\theta,\phi) = (-1)^m Y_{l,-m}(\theta,\phi). \tag{C.10}$$

$$\Gamma(\theta_1,\phi_1;\theta_2,\phi_2) = \sum_{l=1}^{\infty} \sum_{m=-l}^{l} \frac{Y_{l,m}(\theta_1,\phi_1) Y^*_{l,m}(\theta_2,\phi_2)}{l(l+1)} \tag{C.11}$$

According to the addition theorem for spherical harmonics [122]

$$P_l(\cos\gamma) = \frac{4\pi}{2l+1} \sum_{m=-l}^{l} Y_{l,m}(\theta_1,\phi_1) Y^*_{l,m}(\theta_2,\phi_2), \tag{C.12}$$

where $\cos\gamma = \cos\theta_1\cos\theta_2 + \sin\theta_1\sin\theta_2\cos(\phi_1-\phi_2) \rightarrow$ is an angle between two vectors with spherical coordinates (θ_1,ϕ_1) and (θ_2,ϕ_2). Then Eq. (C.11) is simplified to

$$\Gamma(\mathbf{x},\mathbf{y}) = \frac{1}{4\pi} \sum_{l=1}^{\infty} \frac{2l+1}{l(l+1)} P_l(\cos\gamma) = \frac{1}{4\pi} \sum_{l=1}^{\infty} \left(\frac{1}{l+1} + \frac{1}{l}\right) P_l(\cos\gamma). \tag{C.13}$$

The last sum can be performed using the identities [97]

$$\sum_{l=0}^{\infty} \frac{1}{l+1} P_l(x) = \int_0^1 \frac{du}{(1-2ux+u^2)^{1/2}}, \tag{C.14}$$

and

$$\sum_{l=1}^{\infty} \frac{1}{l} P_l(x) = \lim_{\epsilon\to 0} \left(\int_{\epsilon}^{1} \frac{du}{u(1-2ux+u^2)^{1/2}} - \int_{\epsilon}^{1} \frac{du}{u} \right), \tag{C.15}$$

yielding the Green's function on a sphere as

$$\Gamma(\mathbf{x},\mathbf{y}) = -\frac{1}{4\pi} \log \frac{1-\cos\gamma}{2}. \tag{C.16}$$

Geometric potential

The Green's function on a sphere allows to calculate the energy of interactions between pairs of defects. However, the defect itself confined on a curved surface at the position $\mathbf{u}$ feels a geometric potential $V(\mathbf{u})$, defined as [92]

$$V(\mathbf{u}) \equiv -\iint dS\, K(\mathbf{u}')\Gamma(\mathbf{u},\mathbf{u}'), \tag{C.17}$$

where K is the Gaussian curvature. The interaction between the defect and the Gaussian curvature, called the geometric interaction, is described by the energy [96]

$$\mathscr{F}_{\text{self}} = 2\pi K_A q_i \left(1 - \frac{q_i}{2}\right) V(\mathbf{u}). \tag{C.18}$$

The geometric potential $V(\mathbf{u})$ can be cast into the differential form [92]

$$D_\alpha D^\alpha V(\mathbf{u}) = K(\mathbf{u}), \tag{C.19}$$

which follows from Eq. (C.17) and the definition of the Green's function on a surface with metric g_{ij} and point source $\delta(\mathbf{u},\mathbf{u}')$ given by $D_\alpha D^\alpha \Gamma(\mathbf{u},\mathbf{u}') = -\delta(\mathbf{u},\mathbf{u}')/\sqrt{g}$.

In isothermal coordinates $E = G = \lambda(u,v)$, $F = 0$ (see Eq. (2.8)) the metric and the Gaussian curvature are given by

$$ds^2 = \lambda(u,v)(du^2 + dv^2), \quad \text{and} \quad K = -\frac{1}{2\lambda}\Delta(\log\lambda), \quad \Delta = \partial_u^2 + \partial_v^2. \tag{C.20}$$

The product of covariant derivatives $D_\alpha D^\alpha$ is in fact the Laplace–Beltrami operator defined by Eq. (B.7) expressed in isothermal coordinates as

$$D_\alpha D^\alpha V(\mathbf{u}) = \frac{1}{\lambda}\left(\partial_u^2 + \partial_v^2\right) V(\mathbf{u}). \tag{C.21}$$

Substituting this result together with Eq. (C.20) into Eq. (C.19) we find that the geometric potential is defined by the shape of the surface as

$$V(\mathbf{u}) = -\frac{1}{2}\log\lambda(u,v), \tag{C.22}$$

or by replacing the variable with the one used in references [92, 96, 101] as $\lambda(u,v) \equiv e^{-2\omega(\mathbf{u})}$, we recover the following identity

$$V(\mathbf{u}) = \omega(\mathbf{u}). \tag{C.23}$$

Bibliography

[1] Toulouse, G. (1977) *Communication on Physics* **2**, 115.

[2] Kamien, R. D. and Selinger, J. V. (2001) *J. Phys.: Condens. Matter* **13**, R1.

[3] Sadoc, J. F. (1990) Geometry in condensed matter physics, World Scientific, Singapore.

[4] Tarjus, G., Kivelson, S. A., Nussinov, Z., and Viot, P. J. (2005) *Phys.: Cond. Matt.* **17**, R1143.

[5] Emons, A. M. and Mulder, B. M. (2000) *Trends Plant Sci.* **5**, 35.

[6] http://www.ncbi.nlm.nih.gov/books/bv.fcgi?rid=mboc4.section.3603.

[7] Cosgrove, D. J. (1997) *Ann. Rev. Cell Dev. Biol.* **13**, 171.

[8] O'Sullivan, A. C. (1997) *Cellulose* **4**, 173.

[9] Iwata, T., Indrarti, L., and Azuma, J. I. (1998) *Cellulose* **5**, 215.

[10] Nieuwland, J., Feron, R., Huisman, B. A. H., Fasolino, A., Hilbers, C. W., Derksen, J., and Mariani, C. (2005) *The Plant Cell* **17**, 2009.

[11] Baranov, A. I., Anisimova, V. N., Khripunov, A. K., and Baklagina, Y. G. (2003) *Ferroelectrics* **286**, 863.

[12] McQueen-Mason, S. and Cosgrove, D. J. (1994) *Proc. Natl. Acad. Sci. USA* **91**, 6574.

[13] Debenedetti, P. G. and Stillinger, F. S. (2001) *Nature* **410**, 259–267.

[14] Rao, K. J. (2002) Structural chemistry of glasses, Elsevier, Amsterdam.

[15] Frenkel, D. and Smit, B. (2001) Understanding Molecular Simulation, Academic Press, San Diego.

[16] Nose, S. (1990) *J. Phys.: Condens. Matter* **2**, SA115.

[17] Martyna, G. J., Klein, M. L., and Tuckerman, M. (1992) *J. Chem. Phys.* **97**, 2635.

[18] Martyna, G. J., Klein, M. L., and Tuckerman, M. (1992) *J. Chem. Phys.* **97**, 1990.

[19] Martyna, G. J., Tuckerman, M. E., Tobias, D. J., and Klein, M. L. (1996) *Molecular Physics* **87**, 1117.

[20] Binder, K. and Young, A. P. (1986) *Rev. Mod. Phys.* **58**, 801.

[21] Mallamace, F., Gambadauro, P., Micali, N., Tartaglia, P., Liao, C., and Chen, S.-H. (2000) *Phys. Rev. Lett.* **84**, 5431.

[22] Puertas, A. M., Fuchs, M., and Cates, M. E. (2002) *Phys. Rev. Lett.* **88**, 098301.

[23] Cang, H., Novikov, V. N., and Fayer, M. D. (2003) *Phys. Rev. Lett.* **90**, 197401.

[24] Götze, W. and Sjogren, J. (1992) *Rep. Prog. Phys.* **55**, 241.

[25] Götze, W. and Sperl, M. (2002) *Phys. Rev. E* **66**, 011405.

[26] Chen, S. H., Chen, W. R., and Mallamace, F. (2003) *Science* **30**, 619.

[27] Pham, K. N., Puertas, A. M., Bergenholtz, J., Egelhaaf, S. U., Moussaïd, A., Pusey, P. N., Schofield, A. B., Cates, M. E., Fuchs, M., and Poon, W. C. K. (2002) *Science* **296**, 104.

[28] Dawson, K., Foffi, G., Fuchs, M., Götze, W., Sciortino, F., Sperl, M., Tartaglia, P., Voigtmann, T., and Zaccarelli, E. (2000) *Phys. Rev. E* **63**, 011401.

[29] Sciortino, F. (2002) *Nature Mater.* **1**, 145.

[30] Nagasawa, Y., Nakagawa, Y., Mori, Y., Muromoto, T., and Okada, T. (2004) *AIP Conf. Proc.* **708**, 318.

[31] Fabry, B., Maksym, G. N., Butler, J. P., Glogauer, M., Navajas, D., and Fredberg, J. J. (2001) *Phys. Rev. Lett.* **87**, 148102.

[32] Bursac, P., Lenormand, G., Fabry, B., Oliver, M., Weitz, D. A., Viasnoff, V., Butler, J. P., and Fredberg, J. J. (2005) *Nature Materials* **4**, 557.

[33] Deng, L., Trepat, X., Butler, J. P., Millet, E., Morgan, K. G., Weitz, D. A., and Fredberg, J. J. (2006) *Nature Materials* **5**, 636.

[34] Kimura, T. (2003) *Polym. J.* **35**, 823.

[35] Reis, D., Vian, B., Chanzy, H., and Roland, J. C. (1991) *Biol. Cell* **73**, 173.

[36] Belamie, E., Mosser, G., Gobeaux, F., and Giraud-Guille, M. M. (2006) *J. Phys.: Condens. Matter* **18**, S115.

[37] Fuhrhop, J. H. and Wang, T. (2004) *Chem. Rev.* **104**, 2901.

[38] http://www.britannica.com/EBchecked/topicart/342808/lipid.

[39] Jones, R. A. (2002) Soft condensed matter, Oxford University Press, New York.

[40] Leibler, S. Statistical Mechanics of Membranes and Surfaces pp. 56–60 World Scientific second edition (2004).

[41] Shearman, G. C., Ces, O., Templer, R. H., and Seddon, J. M. (2006) *Phys.: Condens. Matter* **18**, s1105.

[42] Lipowsky, R. (1991) *Nature* **349**, 475.

[43] Israelachvili, J. N. (1991) Intermolecular and surface forces, Academic Press, Amsterdam.

[44] Hyde, S., Andersson, S., Larsson, K., Blum, Z., Landh, T., Lidin, S., and Ninham, B. W. (1996) The language of shape: the role of curvature in condensed matter physics, chemistry and biology, Elsevier Science, Amsterdam.

[45] DoCarmo, M. P. (1976) Differential Geometry of Curves and Surfaces, Prentice–Hall, Englewood Cliffs, N.J.

[46] Kamien, R. D. (2002) *Rev. Mod. Phys.* **74**, 953.

[47] David, F. Statistical Mechanics of Membranes and Surfaces chapter 5 World Scientific second edition (2004).

[48] Isenberg, C. (1978) The science of soap films and soap bubbles, Woodspring Press, England.

[49] deGennes, P. G., Brochard-Wyart, F., and Quere, D. (2003) Capillarity and wetting phenomena: drops, bubbles, pearls, waves, Springer, New York.

[50] Plateau, J. A. F. (1873) Statique Expérimentale et Théorique des Liquides Soumis aux Seules Forces Moléculaires, Gauthier-Villars, Paris.

[51] Hutchings, M., Morgan, F., Ritoré, M., and Ros, A. (2000) *Elec. Res. Ann. AMS* **6**, 45.

[52] Antonietti, M. and Förster, S. (2003) *Adv. Mater.* **15**, 1323.

[53] Helfrich, W. (1973) *Z. Naturforsch.* **28C**, 693.

[54] Katsnelson, M. I. and Fasolino, A. (2006) *J. Phys. Chem. B* **110**, 30.

[55] Zhong-can, O.-Y. (2001) *Thin Solid Films* **393**, 19.

[56] Safran, S. A. (1994) Statistical thermodynamics of surfaces, interfaces and membranes, Addison-Wesley, Reading.

[57] Siegel, D. P. and Kozlov, M. M. (2004) *Biophys. J.* **87**, 366.

[58] Jung, H. T., Lee, S. Y., Kaler, E. W., Coldren, B., and Zasadzinski, J. A. (2002) *Proc. Natl. Acad. Sci. USA* **99**, 15318.

[59] Peliti, L. and Leibler, S. (1985) *Phys. Rev. Lett.* **54**, 1690.

[60] Zhong-can, O.-Y., Ji-Xing, L., and Yu-Zhang, X. (1999) Geometric Methods in the Elastic Theory of Membranes in Liquid Crystal Phases, World Scientific, Singapore.

[61] Hsu, L., Kusner, R., and Sullivan, J. (1992) *Experiment. Math.* **1**, 191.

[62] Helfrich, W. (1973) *Phys. Lett. A* **43**, 409.

[63] deGennes, P. G. (1974) The physicsl of liquid crystals, Oxford University Press, London.

[64] Shklyarevskiy, I. O., Christianen, P. C. M., Jonkheijm, P., Schenning, A. P. H. J., Meijer, E. W., Henze, O., Feast, W. J., Kilbinger, A. F. M., Guerzo, A. D., Desvergne, J. P., and Maan, J. C. (2005) *J. Am. Chem. Soc.* **127**, 1112.

[65] Manyuhina, O. V., Shklyarevskiy, I. O., Jonkheijm, P., Christianen, P. C. M., Fasolino, A., Katsnelson, M. I., Schenning, A. P. H. J., Meijer, E. W., Henze, O., Kilbinger, A. F. M., Feast, W. J., and Maan, J. C. (2007) *Phys. Rev. Lett.* **98**, 146101.

[66] Sutter, D. H. and Flygare, W. J. (1969) *J. Am. Chem. Soc.* **91**, 4063.

[67] Maret, G. and Dransfeld, K. (1985) Strong and Ultrastrong Magnetic Fields and Their Applications, Springer-Verlag, Berlin.

[68] Gielen, J. C., Wolffs, M., Portale, G., Bras, W., Henze, O., Kilbinger, A. F. M., Feast, W. J., Maan, J. C., Schenning, A. P. H. J., and Christianen, P. C. M. (2009) *Langmuir* **3**, 25.

[69] Champagne, B., Mosley, D. H., and André, J. M. (1994) *J. Chem. Phys.* **100**, 2034.

[70] Maret, G. and Dransfeld, K. (1977) *Physica* **86-88b**, 1077.

[71] http://en.wikipedia.org/wiki/Superellipse.

[72] Jonkheijm, P., P. vander S., Schenning, A., and Meijer, E. W. (2006) *Science* **313**, 80.

[73] Hass, J., Hutchings, M., and Schlafly, R. (1995) *Elec. Res. Ann. AMS* **1**, 98.

[74] Seifert, U., Berndl, K., and Lipowsky, R. (1991) *Phys. Rev. A* **44**, 1182.

[75] Baumgart, T., Das, S., Webb, W., and Jenkins, J. (2005) *Biophys. J.* **89**, 1067.

[76] Ziherl, P. and Svetina, S. (2007) *Proc. Natl. Acad. Sci. USA* **104**, 761.

[77] Malinin, V. S. and Lentz, B. R. (2004) *Biophys. J.* **86**, 2951.

[78] Kozlovsky, Y., Efrat, A., Siegel, D. A., and Kozlov, M. M. (2004) *Biophys. J.* **87**, 2508.

[79] Katsov, K., Müller, M., and Schick, M. (2004) *Biophys. J.* **87**, 3277.

[80] Seifert, U. (1997) *Adv. Phys* **46**, 13.

[81] Fournier, J. B. and BenAmar, M. (2006) *Eur. Phys. J. E* **21**, 11.

[82] Ozeki, S., Kurashima, H., and Abe, H. (2000) *J. Phys. Chem. B* **104**, 5657.

[83] Helfrich, W. (1974) *Phys. Lett. A* **50**, 115.

[84] Taylor, J. and Cahn, J. (1986) *Science* **233**, 548.

[85] Lubensky, T. C. and Prost, J. (1992) *J. Physique* **2**, 371.

[86] Nelson, D. R. and Peliti, L. (1987) *J. Physique* **48**, 1085.

[87] Chaikin, P. M. and Lubensky, T. C. (1995) Principles of condensed matter physics, Cambridge University Press, United Kingdom.

[88] Landau, L. D. and Lifshitz, E. M. (1986) Theory of elasticity, Pergamon Press, Oxford.

[89] Fasolino, A., Los, J. H., and Katsnelson, M. I. (2007) *Nature Mater.* **6**, 858.

[90] Zakharchenko, K. V., Katsnelson, M. I., and Fasolino, A. (2009) *Phys. Rev. Lett.* **102**, 046808.

[91] Katsnelson, M. I. (2007) *Materials Today* **10**, 20.

[92] Vitelli, V. and Nelson, D. R. (2004) *Phys. Rev. E* **70**, 051105.

[93] Mermin, N. D. (1979) *Rev. Mod. Phys.* **51**, 591.

[94] Bowick, M. J. and Travesset, A. (2001) *J. Phys. A* **34**, 1535.

[95] Nelson, D. R. (2002) *Nanolet.* **2**, 1125.

[96] Vitelli, V. and Turner, A. M. (2004) *Phys. Rev. Lett* **93**, 215301.

[97] Bowick, M. J., Nelson, D. R., and Travesset, A. (2000) *Phys. Rev. B* **62**, 8738.

[98] MacKintosh, F. C. and Lubensky, T. C. (1991) *Phys. Rev. Lett.* **67**, 1169.

[99] Bausch, A. R., Bowick, M. J., Cacciuto, A., Dinsmore, A. D., Hsu, M. F., Nelson, D. R., Nikolaides, M. G., Travesset, A., and Weitz, D. A. (2003) *Science* **299**, 1716.

[100] N. F. M. Henry and K. Lonsdale, (ed.) (1969) International Tables for X-Ray Crystllography, volume **1**, The Kynoch Press, Birmingham.

[101] Turner, A. M., Vitelli, V., and Nelson, D. R. (2009) *Rev. Mod. Phys* **to**, appear.

[102] Tsuzuki, S., Honda, K., and Azumi, R. (2002) *J. Am. Chem. Soc.* **124**, 12200.

[103] Scherlis, D. A. and Marzari, N. (2004) *J. Phys. Chem. B* **108**, 17791.

[104] deGennes, P. G. and Prost, J. (1993) The physicsl of liquid crystals, Oxford University Press, New York.

[105] Ishikawa, T. and Lavrentovich, O. D. (1999) *Phys. Rev. E* **60**, R5037.

[106] Michel, J. P., Lacaze, E., Alba, M., deBoissieu, M., Gailhanou, M., and Goldmann, M. (2004) *Phys. Rev. E* **70**, 011709.

[107] Blanc, C. and Kleman, M. (1999) *Eur. Phys. J. E* **10**, 53.

[108] Ruan, L. Z., Sambles, J. R., and Stewart, I. W. (2003) *Phys. Rev. Lett.* **91**, 033901.

[109] Kleman, M. (1983) Points, Lines, and Walls, Wiley, New York.

[110] Li, Z. and Lavrentovich, O. D. (1994) *Phys. Rev. Lett.* **73**, 280.

[111] Choi, M. C., Pfohl, T., Wen, Z., Li, Y., Kim, M. W., Israelachvili, J. N., and Safinya, C. R. (2004) *Proc. Natl. Acad. Sci. USA* **101**, 17340.

[112] Michel, J. P., Lacaze, E., Goldmann, M., deBoissieu, M., Gailhanou, M., and Alba, M. (2006) *Phys. Rev. Lett.* **96**, 027803.

[113] Kamien, R. D. and Santangelo, C. D. (2006) *Geom. Dedicata* **120**, 229.

[114] Gido, S. P., Gunther, J., Thomas, E. L., and Hoffman, D. (1993) *Macromolecules* **26**, 4506.

[115] Kamien, R. D. and Lubensky, T. C. (1999) *Phys. Rev. Lett.* **82**, 2892.

[116] DiDonna, B. A. and Kamien, R. D. (2003) *Phys. Rev. E* **68**, 041703.

[117] Anderson, D. M., Gruner, S. M., and Leibler, S. (1988) *Proc. Natl. Acad. Sci. USA* **85**, 5364.

[118] http://en.wikipedia.org/wiki/Weierstrass_representation.

[119] Rodriguez, M. M. (2007) *J. Geom. Phys.* **57**, 1371.

[120] DiDonna, B. A. and Kamien, R. D. (2003) *Phys. Rev. E* **68**, 041703.

[121] Capovilla, R. and Guven, J. (2002) *J. Phys. A* **35**, 6233.

[122] http://en.wikipedia.org/wiki/Spherical_harmonics.

[123] http://mathworld.wolfram.com/ParallelPostulate.html.

Summary

This thesis may be seen as a crossing point of three major roads: physics, chemistry, and geometry. To measure the length of these roads in years, like astronomers do to measure the distance to the stars in light years[1], we will assume that 1 year = 1 kilometer. Then the longest, and thus the oldest, road is the road of geometry, stretching for up to 5000 km from Nijmegen to ancient Mesopotamia (nowadays Iraq). We are grateful to Sumerians, who lived there five thousand years ago, for the birth of geometry. Another major road of about 4000 km brings us to Egypt, where the chemistry was born. The third road, the road of physics, stretches to Greece and it is about 2500 km long. Without the knowledge collected on these roads the progress of science and of this thesis, in particular, would be impossible.

The roads

At the beginning of the road of geometry we see temples and the great pyramids, built with the help of Babylonian and Egyptian mathematicians. They could approximate the area of a circle, calculate the volume of the pyramids and other shapes, but it is known very little about their accomplishments and even less is known about their names. What we know for sure is that they had an impact on the development of the Greek mathematics, in particular on Pythagoras, Euclid and Archimedes, whom we meet on the road at the distance about 2300 km from Nijmegen. The Pythagoras theorem and the Euclidean geometry we still learn in school. In fact, for many kilometers the Euclid's *"Elements"*, 13 books on geometry, were considered by many scientists as an example of logical arguments. When the king Ptolemy I had asked Euclid if there is a short way in geometry than his *"Elements"*, Euclid answered that *"There is no royal road in geometry"*. For the next 2000 km geometers were desperately trying to prove the fifth postulate [2] of Euclid as a theorem, using the first four postulates. About 200 km from Nijmegen, János Bolyai and Nikolai Lobachevsky realized independently that logically consistent non-Euclidean geometries can be created even if the fifth postulate does not hold (Gauss had also studied this problem before, but he did not publish any of his results). It was Bernhard Riemann, the student of Gauss, who unified hyperbolic, elliptic and Euclidean geometries, general-

---

[1] 1 Light Year $= 9460730472580.8$ km $\approx 9.46 \cdot 10^{12}$ km.

[2] It is also known as parallel postulate, which is equivalent to the following statement: given any straight line and a point not on it, there exists one and only one straight line which passes through that point and never intersects the first line [123]).

ized differential geometry of surfaces to higher dimensions (Riemannian geometry). The brilliant works of Poincaré determined the development of the 20th century differential geometry and established the foundations of topology (global geometry). In the year 2000 the Clay Mathematical Institute has announced seven *Millennium Prize*[3] *Problems* (in spirit of 23 Hilbert's problems formulated in the year 1900), intended to represent the most significant challenges currently facing mathematics and theoretical physics. It was a sensation when in 2002, Grigori Perelman posted a paper at arXiv.org, stating apropos that he had proven the geometrization conjecture, and hence the Poincaré conjecture (the only 3D manifold in which every loop can shrunk to a point is the three-sphere), which was the most famous open problem in topology formulated by Henri Poincaré in 1904, and one of the seven Millennium Prize Problems. Mathematicians around the world became excited by Perelman's insight. It took three years of "digestion" and thorough examination of his ideas by hundreds of experts before it was announced that Grigori Perelman had truly proven the Poincaré conjecture. It was the "Breakthrough of the year" and the "best piece of mathematics we have seen in the last ten kilometers".

Since antiquity people were trying to understand the forces of nature by observing different phenomena around them. Thus the physics, science about nature, was born. Its name was given by Aristotle, who (as you remember 2500 km away from Nijmegen, in Greece) wrote the first *"Physics"* devoted to the motion. Aristotle is called the father of physics, but it was Archimedes, who, sitting in the bath, invented the first physical law, which says that any body submerged in a liquid loses the weight of this liquid displaced by it. According to the legend, the last words of Archimedes said to the Roman soldier were *"Don't disturb my circles"*, indicating how much he was engrossed in mathematics/physics. Then for many kilometers (about 1700) it was dark[4] on the road of physics. The revolutionary ideas came with Nicolaus Copernicus, who unlike Aristotle, proposed to consider the Earth as other planets moving around the sun. For Aristotle being in motion and being at rest was an obvious distinction, if anything moved there must be a force acting on it. But Galileo's principle of inertia and the first law of Newton stated that a body at rest stays at rest, and a body in motion stays in motion, unless it is acted on by an external force. The second revolution, at the distance about 100 km, on understanding the space, time and motion happened thanks to the genius of Albert Einstein and his theory of relativity saying that all of the laws of physics are the same for every inertial observer. Such breakthrough would be impossible without the knowledge of Riemannian (non-Euclidean) geometry. The last 100 km on this road can be thought of as an intellectual triumph. The landscape became magnificent: air is filled with X-rays, electrons are showing their wave nature, the atoms are bombarded with α- and β-particles, the energy levels of atoms are splitting in magnetic fields, the gasses are cooled to liquids where they reveal amazing properties like superfluidity and superconductivity, and every kilometer a new avenue of physics opens.

About thirty years ago chemists learned how to synthesize huge molecules. They have

---

[3] One million US dollars is offered as a prize for solution.

[4] Of course, not completely dark, because Persian and Arab mathematicians, astronomers, philosophers like Omar Khayyam, Al-Kashi, Ibn al-Haytham (Alhazen), Avicenna had significantly contributed to the development of science. In particular, we owe to Arabs the amazing invention of numerals.

also discovered that such molecules can be bound together not only by strong covalent bonds, but also by weak non-covalent interactions. A new field which focuses on the assemblies of molecules formed due to non-covalent interactions and is called supramolecular chemistry was born. The process of arrangement of millions of molecules in solution into patterns or structures, which happens without any external intervention, is called *self-assembly*. The appearance of order from disorder is surprising, because it may look like the violation of the second law of thermodynamics (entropy cannot decrease in isolated system). But indeed, the molecules tend to stay close to each other, like the penguins in Antarctica favour the surrounding of their warm neighbours rather than arctic air, minimizing their free energy. The self-assembled structures about 100 nanometers (‘nano’= 10^{-9}) size, are therefore in equilibrium, meaning that they live long enough to be explored. The membranes of our cells and many organelles inside the cells are, in fact, self-assembled structures. Although biological systems are more complex, understanding self-assembly could shed light on the origin of life and could be important for biology in general. Many scientists believe that supramolecular self-assembly can contribute to the development of nanotechnology, which is aimed to create ‘nanomaterials and nanodevices of nanoscale’[5]. But there is a long way between discoveries and potential applications. In the special issue of *“Science”*, devoted to 125 anniversary of the journal, there were proposed 25 fundamental questions, the answers of which we would like to know, one of these questions was *“How far can we push self-assembly?”*.

Let us define science as an increase of knowledge by means of observations, experiments, whatsoever. In ancient times (more than 2000 km away) the Library of Alexandria was charged for collecting and preserving all the world’s knowledge. It is likely, that the Library was holding about seven hundred thousand scrolls before it was destroyed by fire. The Torah scroll contains 304.805 letters, which corresponds to about 300 kilobytes (‘kilo’= 10^3) of data, yielding roughly 20 GB (‘Giga’= 10^9) data in total preserved in the Library of Alexandria. Nowadays, the library of Congress, the biggest library in the world, contains about 20 TB (‘Tera’= 10^{12}) data. For comparison, the size of the English part of Wikipedia is about 3 million articles (8 GB of data, June 2009). Books, papers, manuscripts are just the means of sharing knowledge, required by a scientific community. What constitutes science nowadays are new ideas, new discoveries, and the cooperative work of many highly specialized people, driven to understand the world around us. This thesis is just a small brick at the cross-point of three roads, which were shaped by the intellect, imagination, brilliance and courage of many scientists.

The thesis

The basic idea of this thesis is to describe the experimental observations in the framework of phenomenological models. This means that we aimed at understanding the robust, mesoscopic, long-wavelength behaviour of systems, neglecting the details of microscopic interactions. For self-assembled membranes and vesicles (small bubbles),

---

[5] The overuse of the prefix ’nano-’ is done on purpose to show the current obsession of scientists to use fashionable words. This thesis may sound very poor, because the word nanotechnology is used only once.

that are two-dimensional layers of molecules either open or closed, the thickness of the layer (~ 10^{-9} m) is much smaller than the characteristic size of the vesicles (~ 10^{-6} m). Therefore we can neglect the thickness of the membrane and describe it as a truly two-dimensional surface embedded in the three-dimensional Euclidean space. The basic concepts of the differential geometry of surfaces, such as the metric and the curvature, are introduced in chapter 2. It turns out, that curvature describes not only the deviation of the surface (membrane) from the flat layer, but also serves as a good order parameter for the Landau–Ginsburg free energy of membranes. In this thesis we restrict our consideration to fluid membranes only, meaning that molecules can easily flow within a layer and adapt to the change of shape.

Recently, high magnetic fields (up to 20 Tesla) were used to deform[6] spherical vesicles self-assembled from diamagnetic molecules. These molecules tend to align along magnetic field, resulting into the deformation of spherical vesicles into oblate spheroids if the gain in magnetic energy compensates the loss in elastic energy. In chapter 3 we compare the predictions of two theoretical models, assuming a general shape of deformed vesicle as superspheroid, and extract the values of elastic constants from a best fit to experimental data. The bending rigidity (the coefficient in the free energy in front of the square of the mean curvature) turns out to be of the order of $k_B T$, typical for weak non-covalent interactions. However, we found that only a fourth order Landau–Ginsburg expression of the vesicle free energy describes quantitatively the measured elastic deformation up to high magnetic fields, far beyond the quadratic dependence predicted by Helfrich.

It is not surprising that vesicles can easily change their shape in presence of magnetic fields, temperature or other external influences. One may ask another less trivial question, whether changes of topology might occur. Chapter 4 is devoted to the investigation of the possibility of topological transformations from spherical vesicles to a double bubble, which is composed of two spherical caps separated by a flat membrane. Double bubbles can be observed in everyday life when two soap bubbles meet each other, minimizing their surface area of two given volumes, as has been proven by mathematicians in the year 2000, and thus the surface energy. We found that a double bubble can be also an equilibrium shape of vesicles, because it minimizes the elastic free energy, and certainly the presence of a flat membrane minimizes the magnetic energy. Therefore we believe that high magnetic fields can be used to change not only the shape of vesicles, like sphere→superspheroid considered in chapter 3, but also the topology.

The mathematical description that we pursued so far is based on the assumption that curvature is the only paramater accounting for the shape of vesicles. In chapter 5 we show that the stacking of flat aromatic molecules on a curved surface results in unavoidable topological defects. Taking into account the long-range interactions of two defects on spheroids the equilibrium shapes of vesicles turns out to be elongated. This 'simple'[7] geometric approach is the first step to incorporate the details of microscopic interactions into a phenomenological model.

---

[6] The possibility of magnetic deformations of vesicles was predicted long ago, but was never observed before. The High Field Magnet Laboratory in Nijmegen (HFML) did this pioneering work.

[7] The quantitative understanding of the energetics of topological defects involves the calculation of the inverse of the Laplace–Beltrami operator on spheroids, which is a non-trivial problem.

Samenvatting

Dit proefschrift kan gezien worden als een samenkomst van drie belangrijke wegen: natuurkunde, scheikunde en meetkunde. Om de lengte van die wegen te bepalen zullen we postuleren dat 1 jaar overeenkomt met 1 kilometer, op een vergelijkbare manier als die waarop sterrenkundigen afstanden naar sterren uitdrukken[1]. De langste, en dus oudste, weg is de weg van de meetkunde, die 5000 km uitstrekt van Nijmegen tot Mesopotamië, het tegenwoordige Irak. We hebben de geboorte van de meetkunde te danken aan de Sumeriërs die daar vijfduizend jaar geleden leefden. De tweede weg, die ongeveer 4000 km lang is, begint in Egypte, waar de scheikunde is geboren. De derde weg, die van de natuurkunde, komt uit Griekenland en is ongeveer 2500 km lang. Zonder de kennis die bij de reis over deze wegen is verkregen, zou de vooruitgang van de wetenschap in het algemeen en het ontstaan van dit proefschrift in het bijzonder onmogelijk zijn[2].

Het basisidee van dit proefschrift is om experimentele observaties te beschrijven met fenomenologische modellen. Dit betekent dat we het robuuste, mesoscopische gedrag op lange golflengtes van sytemen willen begrijpen, en de details van de microscopische interacties willen verwaarlozen. In het geval van zelf-geassembleerde membranen en vesicules (kleine belletjes), die bestaan uit open of gesloten tweedimensionale lagen van moleculen, is de dikte van de laag ($\sim 10^{-9}$ m) veel kleiner dan de typische afmeting van de vesicules ($\sim 10^{-6}$ m). We kunnen daarom de dikte van de membranen verwaarlozen en ze beschrijven als een tweedimensionaal oppervlak ingebed in de driedimensionale Euclidische ruimte. De fundamentele concepten van differentiaalmeetkunde op oppervlakken, zoals metriek en kromming, worden geintroduceeerd in hoofdstuk 2. Het is gebleken dat kromming niet alleen kan worden gebruikt om de afwijking van een oppervlak (membraan) van een platte laag te beschrijven, maar ook een goede ordeparameter is voor de Landau–Ginsburg vrije energie van membranen. In dit proefschrift beperken we ons tot vloeistofmembranen, wat betekent dat de moleculen makkelijk kunnen bewegen over het oppervlak, en zich aanpassen aan veranderingen in de vorm.

Recent zijn hoge magnetische velden (tot 20 Tesla) gebruikt om bolvormige vesicules bestaand uit diamagnetische moleculen te vervormen[3]. Deze moleculen hebben de

---

[1] 1 Lichtjaar $= 9460730472580.8$ km $\approx 9.46 \cdot 10^{12}$ km.

[2] Als U meer belangstelling heeft in de historische achtergrond, lees dan verder de engelstalige samenvatting op pagina 111.

[3] Het was al lang geleden voorspeld dat vesicules magnetisch vervormd konden worden, maar dit was nog nooit geobserveerd. Dit werk werd uitgevoerd in het High Field Magnet Laboratory in Nijmegen (HFML).

neiging om langs de magnetische-veldlijnen te gaan staan, wat leidt tot afplatting van de vesicules als de lagere magnetische energie de hogere elastische energie compenseert. In hoofdstuk 3 vergelijken we de voorspellingen van twee theoretische modellen waarbij wordt aangenomen dat de vesicule een superspheroïde vorm heeft, en bepalen de waardes van elastische constanten met behulp van een fit aan experimentele gegevens. De stijfheid (de coëfficient voor het kwadraat van de gemiddelde kromming in de vrije energie) blijkt van dezelfde orde van grootte te zijn als $k_B T$, wat typisch is voor zwakke niet-covalente interacties. Aan de andere kant hebben we ontdekt dat een vierde orde Landau–Ginsburg uitdrukking voor de vrije energie van de vesicules nodig is om de gemeten elastische vervorming in sterke magnetische velden quantitatief goed te beschrijven, wat verder gaat dan de kwadratische afhankelijkheid die door Helfrich is voorspeld.

Het is niet verrassend dat vesicules makkelijk van vorm kunnen veranderen onder invloed van magnetische velden, temperatuur, of andere externe parameters. Een minder triviale vraag is of ook veranderingen van de topologie mogelijk zijn. Hoofdstuk 4 is gewijd aan de mogelijkheid om de topologie van bolvormige vesicules te veranderen zodat het dubbele bellen worden, die een andere topologie hebben dan enkele boloppervlakken of twee losse boloppervlakken. Dubbele bellen komt men tegen in het dagelijks leven als twee zeepbellen bij elkaar komen en voor de gegeven twee volumes hun oppervlakte (en dus de oppervlakte-energie) wordt geminimaliseerd, zoals door wiskundigen werd aangetoond in 2000. We hebben ontdekt dat een dubbele bel ook een evenwichtstoestand is voor vesicules, omdat de elastische vrije energie geminimaliseerd wordt, en de aanwezigheid van een vlak membraan de magnetische energie zeker minimaliseert. We zijn er daarom van overtuigd dat hoge magnetische velden niet alleen gebruikt kunnen worden om de vorm van vesicules te veranderen (zoals van bol naar superspheroïde in hoofdstuk 3), maar ook de topologie.

De wiskundige beschrijving die we tot nu toe hebben gebruikt is gebaseerd op de aanname dat de kromming de enige paramater is die van belang is voor de vorm van de vesicules. In hoofdstuk 5 laten we zien dat de stapeling van platte aromatische moleculen op een gekromd oppervlak leidt tot topologische defecten. Het is uit ons onderzoek naar de interacties van de twee defecten op een bol over lange afstanden gebleken dat in evenwicht de vorm van de vesicules uitgerekt is. Deze “simpele”[4] geometrische aanpak is de eerste stap op weg om de details van de microscopische interacties in een fenomenologisch model in te bouwen.

---

[4] Voor de quantitatieve beschrijving van de energiën van topologische defecten is het nodig om de inverse van de Laplace–Beltrami operator uit te rekenen, en dat is niet triviaal.

Заключение

Эту диссертацию можно представить как пересечение трех больших дорог: физики, химии и геометрии[1]. Давайте измерять расстояние на этих дорогах в годах, подобно тому, как астрономы измеряют расстояние до звезд в световых годах[2], будем предполагать, что 1 год = 1 км. Самая длинная, а значит и самая древняя дорога, это дорога геометрии, которая простирается почти на 5000 км, от Наймегена до древней Месопотамии (современный Ирак). Мы благодарны шумерам, которые жили там примерно 5000 лет тому назад, за рождение геометрии. Вторая дорога, длиной в 4000 км приводит нас в Древений Египет, где родилась химия. Третья дорога – дорога физики – простирается до древней Греции 'всего лишь' на 2500 км. Без знаний, которые накапливались на этих дорогах, прогресс науки, и эта диссертация в частности, были бы невозможны.

Дороги

В начале дороги геометрии мы замечаем с обеих сторон храмы и великие пирамиды, построенные с помощью знаний вавилонских и египетских математиков. Они умели приближенно вычислять площадь окружности, объем пирамиды и других фигур, но мы знаем очень мало об их достижениях и еще меньше об их именах. Однако нам точно известно, что их работы имели большое влияние на развитие древнереческой математики, в частности, на Пифагора, Евклида и Архимеда, которых мы встречаем на этой дороге на расстоянии примерно в 2300 км от Наймегена. Теорему Пифагора и геометрию Евклида мы до сих пор изучаем в школе. В действительности, на протяжении сотен километров Евклидовы «*Начала*», 13 книг посвященных геометрии, служили для многих ученых примером логических рассуждений. Когда царь Египта Птолемей I спросил Евклида: «Существует ли в геометрии дорога проще, чем его "*Начала*"», Евклид ответил: «*В геометрии нет царских дорог*». На протяжении последующих 2000 км геометры

---

[1] Нужно заметить, что русская версия заключения не претендует на плавность переходов и гладкость текста, поскольку является простым переводом английской.

[2] 1 световой год $= 9460730472580.8 \approx 9.46 \cdot 10^{12}$ км.

отчаянно пытались доказать пятый постулат Евклида[3] как теорему, используя первые четыре постулата. Лишь примерно в 200 км от Наймегена, Янош Бойяи и Николай Лобачевский независимо друг от друга осознали , что возможно создать логически совместимую "Неевклидову" геометрию, где пятый постулат не выполняется (нужно заметить, что Гаусс также уделял внимание этой проблеме, но не опубликовал свои результаты). Только его ученик, Бернхард Риман, обьединил гиперболическую, эллиптическую и Евклидову геометрии, обобщил дифференциальную геометрию поверхностей на пространства более высокой размерности и фактически создал новую геометрию – Риманову. Блестящие работы Пуанкарэ определили развитие геометрии 20-го века и положили основу топологии (глобальной геометрии). В 2000 году Математический институт Клэя обьявил семь *Проблем тысячелетия* подобно 23 проблемам Гильберта, сформулированным в 1900 году) за решение каждой из которых предложен приз в 1 миллион долларов, определяя наиболее важные и сложные задачи с которыми столкнулись современная математика и теоретическая физика. Это была сенсация, когда в 2002 году Григорий Перельман выложил статью в arXiv.org, в которой сообщалось, что он доказал гипотезу Терстона о геометризации, и следовательно доказал гипотезу Пуанкарэ (всякий 'трехмерный объект', каждая петля внутри которого стягиваема, обязан быть трехмерной сферой с точностью до деформации). Гипотеза Пуанкаре являлась наиболее известной нерешенной задачей топологии, сформулированной Генри Пуанкарэ в 1904 году, и одной из семи *Проблем тысячелетия*. Математики во всем мире были потрясены проницательностью Перельмана. Потребовалось три года проверок и тщательного изучения его идей сотней экпертов, прежде чем было объявлено, что Григорий Перельман действительно доказал гипотезу Пуанкарэ. Это был «Прорыв года» и «лучший кусок математики, который мы видели за последние 10 километров».

С давних времен люди пытались понять силы природы, наблюдая различные явления вокруг. Так родилась физика, наука о природе. Имя 'физика' дано Аристотелем, которого как вы помните мы повстречали в 2500 км вдали от Наймегена, в Древней Греции. Он написал первую «*Физику*», посвященную движению. Аристотеля называют крестным отцом физики, но первый закон физики 'сидя в ванной' открыл Архимед, в шуточном варианте он звучит так

> Если тело вперто в воду,
> Не потонет оно сроду,
> Ибо давит оттуды,
> Сила выпертой воды.

---

[3] Пятый постулат или аксиома параллельности Евклида, гласит: в плоскости, через точку не лежащую на данной прямой, можно провести одну и только одну прямую, параллельную данной.

Согласно легенде, последние слова Архимеда, сказанные римскому солдату были *«Не тронь моих чертежей!»*, которые свидетельствуют о том как сильно он был поглощен математикой/физикой. После Архимеда на многие километры (около 1700) дорога физики оставалась неосвещенной[4]. Революционные идеи пришли вместе с Николаем Коперником, который, в отличие от Аристотеля, предложил рассматривать Землю также как и другие планеты, вращающимися вокруг Солнца. Для Аристотеля, движение и покой были различными состояниями, если тело двигалось, должна быть сила действующая на него. Но принцип инерции Галилея и первый закон Ньютона гласят: **тело, находящееся в состоянии покоя или равомерного прямолинейного движения, остается в этом состоянии, до тех пор пока сумма внешних сил, приложенных к нему равняется нулю**. Вторая революция в понимании пространства, времени и движении произошла еще через 200 км (уже всего в 100 км отсюда), благодаря гению Альберта Эйнштейна и его теории относительности, говорящей о том, что **все законы физики инвариантны (не зависят от) в инерциальных системах отсчета** и этот прорыв был бы невозможен без Римановой геометрии. Последние 100 км дороги физики можно описать как интеллектуальный триумф человечества. Пейзаж стал великолепным: воздух наполнился рентгеновскими лучами, электроны открывают свою волновую природу, атомы бомбардируются альфа- и бета-частицами, их энергетические уровни расщепляются под воздействием магнитного поля, охлажденные до жидкого состояния газы, приоткрывают завесу тайны над сверхтекучестью и сверхпроводимостью, и каждый километр открываются новые проспекты физики.

Около 30 лет назад химики научились синтезировать большие молекулы. Они также открыли, что эти молекулы могут связываться в единое целое не только посредством сильных ковалентных связей, а также с помощью слабых нековалентных связей. Родилась новая область, *супрамолекулярная химия*, которая изучает ансамбли молекул сформированных за счет нековалентных связей. Процесс упорядочивания миллиона молекул, находящихся в растворе, в структуры, происходящий без внешнего вмешательства, называется *самосборкой*. Возникновение порядка из беспорядка достаточно неожиданное явление, поскольку это похоже на нарушение второго закона термодинамики (в изолированной системе энтропия не может уменьшаться). В действительности же, молекулы склонны находиться близко друг к другу, как пингвины в Антарктике предпочитают быть окруженными теплыми соседями, а не холодным антарктическим воздухом, таким образом минимизируя свою свободную энергию. Вследствие этого, самособирающиеся структуры размером порядка 100 нанометров ('нано'$= 10^{-9}$) находятся в равновесии, и могут быть экспериментально исследованы. Мембраны на-

---

[4] На этой темной дороге виднелись проблески в виде персидских и арабских метематиков, астрономов, философов таких, как Омар Хаям, ал-Каши, Ибн ал-Хайсам, Авиценна, которые повлияли на развитие науки. В частноти, мы в долгу перед арабами за изумительное изобретение цифр.

ших клеток и многие органеллы внутри клеток в сущности являются самособранными структурами. Несмотря на то, что биологические системы гораздо более сложны, понимание самосборки может пролить свет на происхождение жизни и может быть важно для биологии в общем. Многие ученые полагают, что супрамолекулярная самосборка может способствовать развитию нанотехнологий, направленных на создание `'наноматериалов и наноустройств на наномасштабах'[5]. Но путь от окрытия до потенциального применения может быть очень длинным. В специальном выпуске «*Science*», посвященному 125-летию журнала, было предложено 25 фундаментальных вопросов, ответы на которые мы хотели бы знать, один из этих вопросов был «*Как далеко мы можем продвинуть самосборку?*»

Давайте определим науку, как накопление знаний с помощью наблюдений, экспериментов и чего бы то ни было еще. В древние времена (на расстоянии более 2000 км от нас) Александрийская библиотека стремилась собрать и сохранить все знания мира. Считается, что в библиотеке находилось около семисот тысяч свитков до того, как ее сожгли. Свиток Торы содержит 304.805 букв, что соответствует 300 килобайтам ('кило'$= 10^3$) данных, что дает примерно 20 ГБ ('Гига'$= 10^9$) данных хранившихся в Александрийской библиотеке. В настоящее время библиотека Конгресса США – крупнейшая библиотека мира, будучи оцифрованной будет содержать около 20 ТБ ('Тера'$= 10^{12}$) информации. Для сравнения, английская части Википедии по состоянию на июнь 2009 года, содержит около 3 миллионов статей (или примерно 8 ГБ данных). Книги, статьи, рукописи – это способ распространения знаний, – необходимый элемент для функционирования научного общества. Науку же в настоящее время составляют новые идеи, открытия и совместная работа множества высокообразованных людей, пытающихся понять мир вокруг нас. Эта диссертация является маленьким камнем на пересечении трех дорог, форму которых определили интеллект, воображение, блеск и мужество многих ученых.

Диссертация

Основополагающей идеей этой диссертации является описание экспериментальных наблюдений с использованием феноменологических моделей. Это означает, что мы стремимся понять грубое, мезоскопическое, поведение системы на больших масштабах, пренебрегая деталями микроскопических взаимодействий. У самособранных мембран и везикул (маленький пузырь), которые представляют из себя двумерный слой молекул с открытой или закрытой границей, толщина слоя ($\sim 10^{-9}$ м) много меньше, чем характерный размер везикулы ($\sim 10^{-6}$ м). Поэтому мы можем пренебречь этой толщиной и описывать мембрану, как двумерную поверхность заключенную

---

[5] Чрезмерное использование префикса 'нано' было сделано с намерением показать одержимость некоторых ученых в использовании модных слов. Эта диссертация может выглядеть очень 'бледной', поскольку слово нанотехнологии используется только единожды.

в трехмерное Евклидовое пространство. Основные понятия дифференциальной геометрии поверхностей, такие как метрика и кривизна, изложены во второй главе. Оказывается, что кривизна, т.е. отклонение поверхности (мембраны) от плоского слоя, служит хорошим параметром порядка для свободной энергии Гинзбурга—Ландау. В этой диссертации мы ограничиваемся рассмотрением жидких мембран, где молекулы могут свободно перемещаться внутри слоя и приспосабливаться к изменению формы.

Недавно, высокие магнитные поля (до 20 Тесла) были использованы для деформации сферических везикул, самособранных из диамагнитных молекул[6]. Эти молекулы стремятся выровняться вдоль магнитного поля, приводя к деформации сферических везикул в сплющенные эллипсоиды, если уменьшение магнитной энергии компенсирует рост эластической энергии. В третьей главе мы сравниваем предсказания двух теоретических моделей, предполагая, что деформированная везикула имеет суперсфероидальную форму, и извлекаем величины эластических констант из наилучшего согласия теории и эксперимента. Модуль жесткости на изгиб (коэффициент в свободной энергии перед квадратом средней кривизны) оказывается порядка $k_B T$, как и ожидалось для слабых нековалентных связей. Мы также обнаружили, что только четвертый порядок разложения свободной энергии Гинзбурга—Ландау для везикул, колличественно описывает измеренные магнитные деформации вплоть до высоких магнитных полей, что оказывается за пределами квадратичной зависимости предсказанной Хелфричем.

Неудивительно, что везикулы могут легко изменять свою форму в присутствии магнитных полей, температуры, или других внешних воздействий. Однако возникает менее тривиальный вопрос: могут ли они изменять топологию? Четвертая глава посвящена исследованию возможностей топологических переходов от сферических везикул к двойному пузырю, который состоит из двух сферических сегментов разделенных плоской мембраной. Двойные пузыри можно наблюдать в повседневной жизни, когда встречаются два мыльных пузыря, минимизируя свою поверхность (а значит и певерхностную энергию) при двух заданных обьемах, что было доказано математиками в 2000 году. Мы обнаружили, что двойной пузырь может также быть равновесной формой везикул, поскольку он минимизирует эластическую энергию, а присутствие плоской мембраны также минимизирует магнитную энергию. Поэтому мы полагаем, что высокие магнитные поля могут быть использованы не только для изменения формы, например для деформации сферы в суперсфероид, рассмотренные в третьей главе, но и для изменения топологии.

Математическое описание которому мы следовали до сих пор основывается

---

[6] Возможность магнитных деформаций везикул была предсказана давно, но никогда не наблюдалась ранее. Это открытие было сделано в Лаборатории Высоких Магнитных Полей в Наймегене.

на предположении, что кривизна является единственным параметром отвечающим за форму везикулы. В пятой главе мы показываем, что регулярная упаковка плоских ароматических молекул на искривленной поверхности неизбежно приводит к появлению топологических дефектов. Принимая во внимание дальнодействующие взаимодействия между двумя дефектами на сфероидах, равновесная форма везикулы получается удлиненной. Этот ’простой’[7] геометрический подход можно рассматривать как первый шаг к включению микроскопических взаимодействий в феноменологические модели.

---

[7] Колличественное описание энергетики топологических дефектов включает в себя нахождение обратного оператора Лапласа—Бельтрами для сфероидов, что составляет нетривиальную задачу.

Curriculum Vitae

Manyuhina Oksana Vyacheslavovna was born on 11 February 1982 in Leningrad, USSR (now Saint-Petersburg, Russia). In 1998 she graduated from the Lyceum of Physics and Mathematics in Cherkasy, Ukraine. Then she went to study in Moscow Institute of Physics and Technology ("PhysTech") at the faculty of Molecular and Biological Physics. Her master project entitled *Theoretical study of elastic wave propagation in human lungs* was done under supervision of Dr. A. I. D'yachenko in General Physics Institute of the Russian Academy of Science. In 2004 she received her Master degree in applied Physics and applied Mathematics and Diploma with honors. In the years 2001–2004 she was teaching mathematics at PhysTech College (high school with advanced instructions in Physics and Mathematics). Since 21 January 2005 she was employed as a "junior-onderzoeker" (PhD-student) in the Theory of Condensed Matter department of the Radboud University Nijmegen. She was a student's teaching assistant at the courses of Statistical Mechanics and Advanced Statistical Physics from 2005 till 2007. In the year 2007 she won Frye Stipendia, a grant which allows to make an extended scientific trips.

‘*I wonder,*’ thought the Hedgehog, ‘*if the horse lies down to sleep, will it choke in the fog?*’

‘*Excuse me,*’ said someone quietly, ‘*who are you and how did you get here?*’

‘*I am a hedgehog. I fell in the river.*’

‘*Then get on my back. I will carry you to the shore.*’

‘*Oh, who other than you knows how to count the stars?!*’

Hedgehog in the fog
Sergei Kozlov and Yuri Norstein.

«*А интересно,* – подумал Ежик, – *если лошадь ляжет спать, она захлебнется в тумане?*»

«*Извините,* – беззвучно сказал кто-то, – *кто вы и как сюда попали*».

«*Я – Ежик. Я упал в реку*».

«*Тогда садитесь ко мне на спину. Я отвезу вас на берег*».

«*Ведь кто же, кроме тебя, звезды-то считать будет?!*»

«Ежик в тумане»
Сергей Козлов и Юрий Норштейн.